POLITECNICO DI TORINO

Corso di Laurea in Ingegneria Meccanica

Tesi di Laurea

# Analysis of Hydrokinetic Turbines for Application in Congo


**Relatori**
Ing. Giovanni Bracco
Prof.ssa Giuliana Mattiazzo

**Candidato**
John Erwin Dinglasan

Dicembre 2018

**Abstract**

In recent decades, the demand for renewable energy has always been growing, mainly due to pollution caused by excessive consumption of fossil fuels. For this reason, a lot of research in this area has been carried out, supported by technological developments. The renewable energy sector is dominated by wind, water and solar technologies. Africa is a country rich in renewable resources, but poor in the ability to exploit and use them. Although there is a distribution of electricity production plants (e.g., dams, wind farms, etc..), it is not sufficient to cover the vastness of the African territory, making the transport of energy and its costs among the major problems in this sector. These difficulties mainly affect small communities, which in some cases have to rely on the production of their own electricity. The work developed in this thesis is divided into two parts: an investigation of theories and technologies in the field of smallhydro; evaluation of renewable technologies in Oyo, Congo. In particular, a potential application in the Alima River, which touches the city of Oyo, was analysed. To this purpose, two optimization software for horizontal and vertical axis turbines were used to estimate the potential of the river.

# Contents

# List of Tables

# List of Figures

# Chapter 1

# Renewable energy

## 1.1 Introduction

Renewable energy is energy that is collected from renewable resources(RES), which are naturally replenished on a human timescale, such as sunlight, wind, rain, tides, waves and geothermal heat. Based on REN21's 2016 report [7], renewables contributed 19.3% to human global energy consumption and 24.5% to their generation of electricity in 2016.

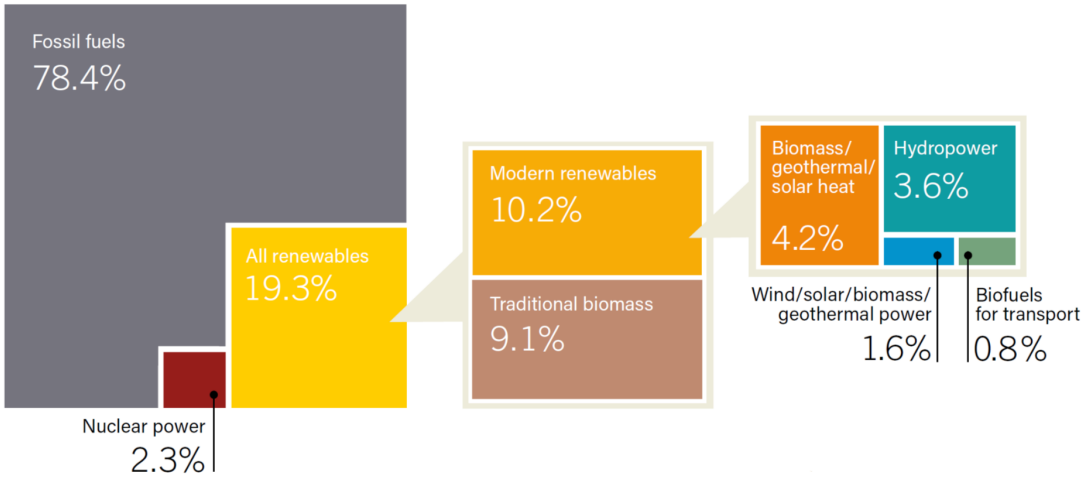


Figure 1.1.1: Renewable Energy Share of Total Final Energy Consumption in 2015

Renewable energy is a clean and inexhaustible energy, it occurs naturally in the environment and, therefore, should never run out. RES reduced environmental effects compared to fossil fuels. Renewable technologies like water and wind power probably would not have provided the same fast increase in industrial productivity as fossil did. Oil and gas are expected to continue to be important sources of energy. The share of renewable energy sources is expected to increase very significantly (to 30 – 80% in 2100) [8].
About 98% of carbon emissions result from fossil fuel combustion. Reducing use of fossil fuels would considerably reduce the amount of carbon dioxide produced, as well as reducing the levels of the pollutants. The "20-20-20" protocol imposed to

the participating countries to reduce by 20% the consumption of primary sources, to reduce by 20% the climate-changing gases emissions and to increase the contribution of renewable energies up to 20% of the country overall energy request. For the future, after the 2020 deadline, new and more restrictive standards have already been set: the European Union intends to achieve a reduction of 40% of emissions by 2030 and a reduction of 80% by 2050.

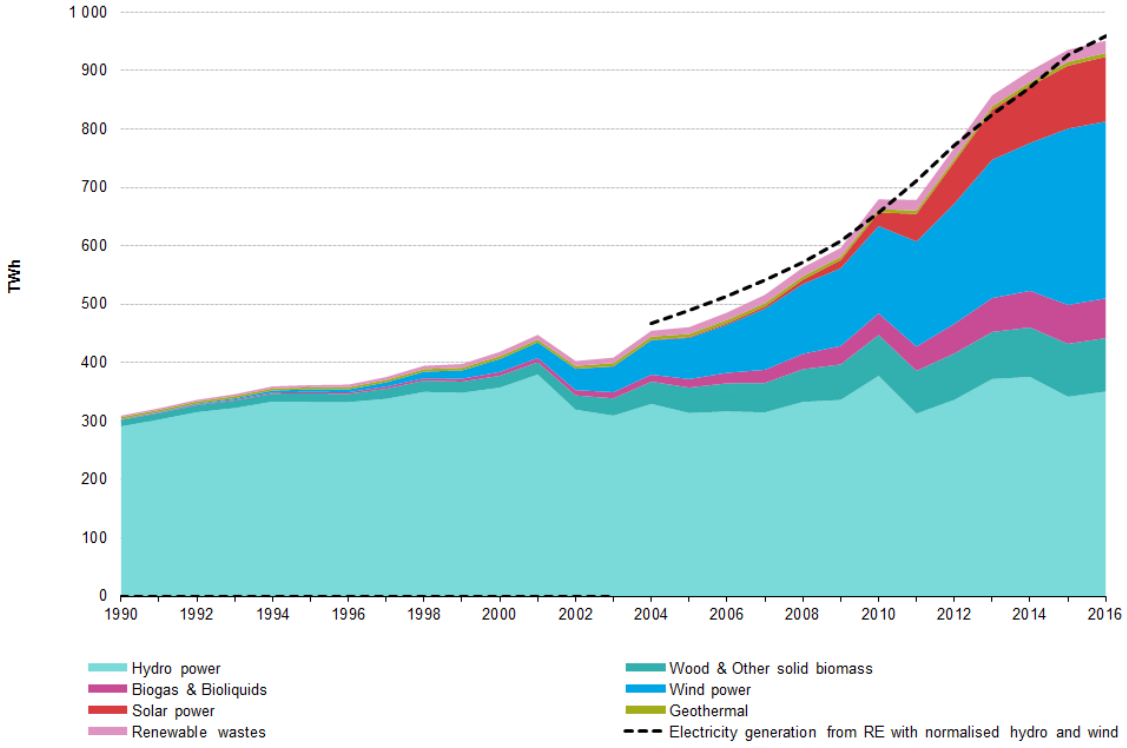


Figure 1.1.2: Gross electricity generation from renewable sources 1990-2016 [3]

### 1.1.1 Hydropower

In recent years, there has been a major upsurge in hydropower development. The total installed capacity has grown by 39% from 2005 to 2015, with an average growth rate of nearly 4% per year. The rise has been concentrated in emerging markets where hydropower offers not only clean energy, but also provides water services, energy security and facilitates regional cooperation and economic development. The drivers for the upsurge in hydropower development include the increased demand for electricity, energy storage, flexibility of generation, freshwater management, and climate change mitigation and adaptation solutions. On the one hand, there has been significant progress in terms of sustainability practices in the sector and acceptance by external stakeholders such as NHOs and the financial community, which had previously opposed the development of some new projects. On the other hand, criticism of hydropower continues in some stakeholder groups, whose views are mainly biased by past negative experiences and a lack of acknowledgement of sustainable projects successfully built more recently. Hydropower is the leading renewable source for

electricity generation globally, supplying 71% of all renewable electricity. Reaching 1,064 GW of installed capacity in 2016, it generated 16.6% of the world's electricity from all sources [7].

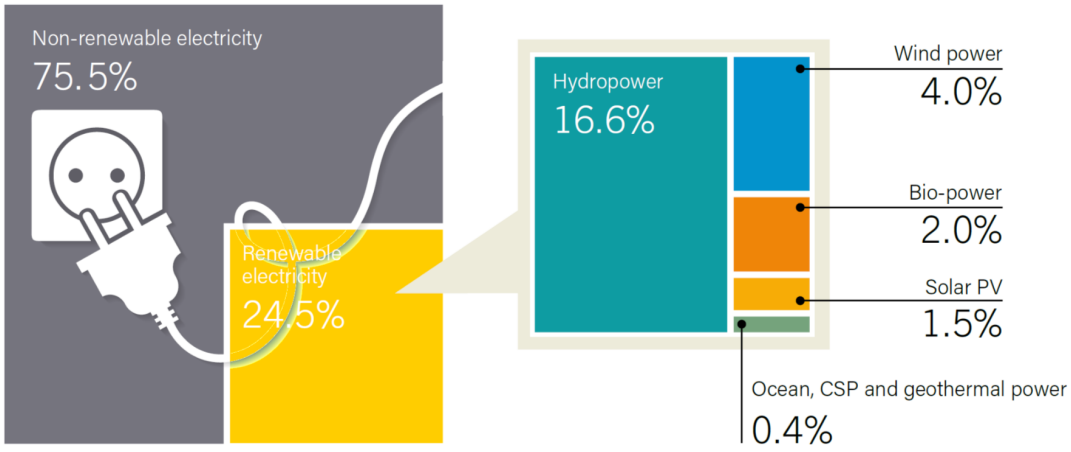


Figure 1.1.3: Renewable Energy Share of Global Electricity Production in 2016

Since 2004, there has been a resurgence in hydropower development, particularly in emerging markets and less developed countries. Significant new development is concentrated in the markets of Asia (particularly China), Latin America and Africa. In these regions, hydropower offers an opportunity to supply electricity to under-served populations and a growing industrial base, while at the same time providing a range of complementary benefits associated with multi-purpose projects [9].

### 1.1.2 Types of hydropower

Hydropower is power derived from the energy of falling water or fast running water, which may be harnessed for useful purposes. Generally, a first difference is based on the power generated. They are defined [8]:

- Large scale system: the technically usable world potential of large-scale hydro is estimated to be over 2200 GW, of which only about 25% is currently exploited.In the developing countries, considerable potential still exists, but large hydropower projects may face financial, environmental, and social constraints;
- Small hydro system: with capacity between 100 kW and 1 MW;
- Micro hydro system: with capacities below 100 kW;

The current commercially available technologies generate electricity through the transformation of hydraulic energy into mechanical energy to activate a turbine connected to a generator [9]. It is a versatile energy source, which can respond to different power system requirements while adapting to different physical and environmental constraints as well as stakeholders' interests. Although hydropower plants are highly site-specific (the local topography and hydrology will define the type of facilities that can be built), they can be broadly categorised into four main typologies:

- **Storage Hydropower:** a facility that uses a dam to impound river water, which is the stored for release when needed. Electricity is produced by releasing water from the reservoir through operable gates into a turbine, which in turn activates a generator. Storage hydropower can be operated to provide base-load power, as well as peak-load through its ability to be shut down and started up at short notice according to the demands of the system. It can offer enough storage capacity to operate independently of the hydrological inflow for many weeks, or even up to months or years. Given their ability to control water flows, storage reservoirs are often built as multi-purpose systems, providing additional benefits. The primary advantage of hydro facilities with storage capability is their ability to respond to peak load requirements.

Figure 1.1.4: Grand Inga dam

- **Run-of-river hydropower:** a facility that channels flowing water from a river through a canal of penstock to drive a turbine. Typically, a run-of-river project will have short term water storage and result in little or no land inundation relative to its natural state. Run-of-river hydro plants provide a continuous supply of electricity, and are generally installed to provide base load power to the electrical grid (see figure 1.1.5). These facilities include some flexibility of operation for daily/weekly fluctuations in demand through water flow that is regulated by the facility.

Figure 1.1.5: Chief Joseph Dam

- **Pumped-storage hydropower:** provides peak-load supply, harnessing water which is cycled between a lower and upper reservoir by pumps, which use surplus energy from the system at times of low demand. When electricity demand is high, water is released back to the lower reservoir through turbines to produce electricity. Pumped-storage hydropower is practically speaking a zero sum electricity producer. Its value is in the provision of energy storage, enabling peak demand to be met, assuring a guaranteed supply when in combination with other renewables, and other ancillary services to electrical grids. One major advantage of pumped-storage facilities is their synergy with variable renewable energy supply options such as wind and solar power. This is because pump-storage installations can provide back-up reserve which is immediately dispatchable during periods when the other variable power sources are unavailable.

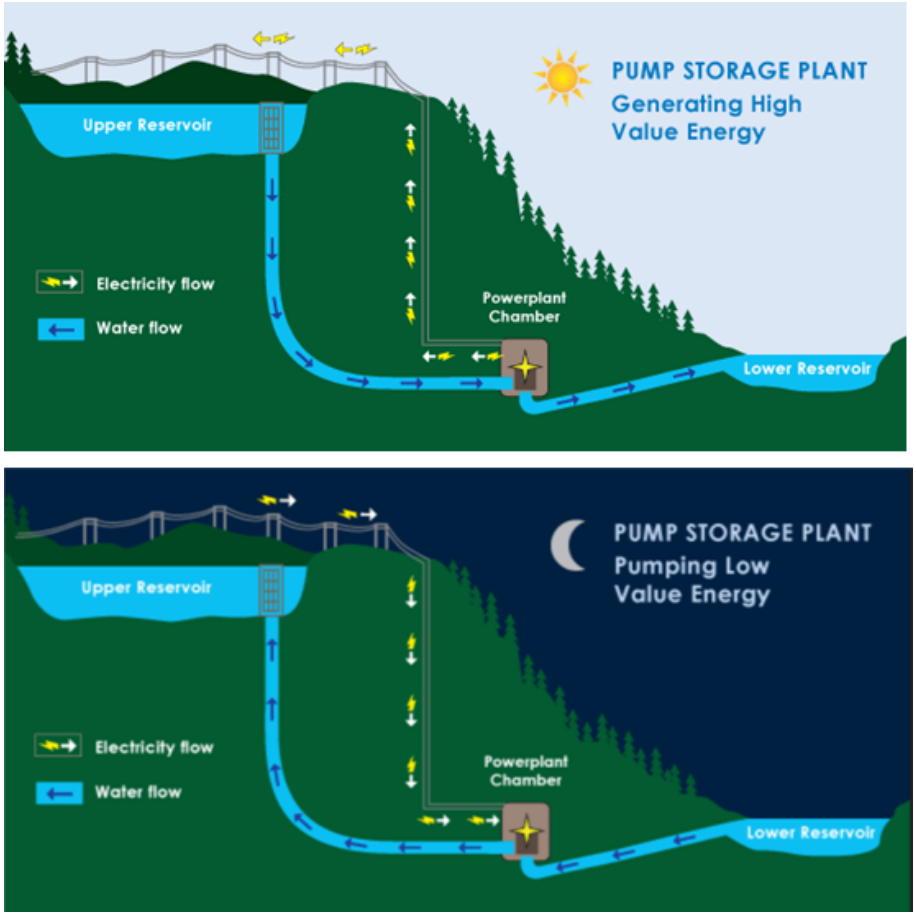


Figure 1.1.6: Pumped-storage hydropower

- **Offshore marine and other new technologies:** a less established, but growing group of hydropower technologies that use the power of currents or waves to generate electricity from seawater. These include hydrokinetic (river, ocean and wave), tidal barrage and tidal stream, osmotic, and ocean thermal technologies.

Hydropower technologies are not bound by size constraints – the basic technology is the same irrespective of the size of the development. Large-scale hydropower installations typically require storage reservoirs as mentioned earlier in this section. Smaller-scale hydropower systems can be attached to a reservoir, or they can be installed in small rivers, streams or in the existing water supply networks, such as drinking water or wastewater networks. Small-scale hydropower plants are typically run-of-river schemes or implemented in existing water infrastructure. As with all energy technologies, hydropower facilities are reported on in terms of their installed capacity. Hydropower facilities installed today range in size from less than 100 kW to greater than 22 GW, with individual turbines reaching 1000 MW in capacity [9].

# Chapter 2

# Turbine

## 2.1 History

The idea of using naturally water or air to help do work is an ancient one. Waterwheels and windmills are the best examples of ancient mankind's ability to capture some of nature's energy and put it to work. According to historians, the first machines utilising wind energy were operated in the orient. As early as 1700 B.C., it is mentioned that Hammurabi used windmills for irrigation in the plains of Mesopotamia [10]. The first practical windmills had sails that rotated in a horizontal plane, around a vertical axis. This system was developed, in Persia about 500-900 A.D. An asymmetry was created by screening half the rotor with a wall. This way the drag forces could be utilised for driving the rotor. Vertical-axis windmills were also used in China, which is often claimed as their birthplace. The earliest actual documentation of a Chinese windmill was in 1219 A.D [11]. In Chinese windmills, a similar asymmetry is created by sails which rotate out of the wind on their way "back", that is when they advance into the wind. Similar to the Persian mills, they had a vertical axis. However, in contrast to the Persian mills, they had the typical advantage of vertical axis windmills to utilise the wind independent of its direction.

The first reference to a water wheel dates back to around 4000 B.C. Vitruvius, an engineer who died in 14 AD, is later credited with creating and using a vertical water wheel during Roman times. The hydraulic turbine is a modern invention based on the same principles as the water wheel [12] - [13].

Both windmills and waterwheels have large surfaces (paddles, buckets, or a sail) at their edges that are stuck by moving wind or water which forces the wheel to turn. It was through the turning of this large central wheel, which drove the gears, that mechanical energy was obtained and work like grinding corn or operating a pump. The most ancient of these methods was the undershot wheel or paddle wheel. On these old waterwheels, only the very lowest part of the wheel was submerged beneath a moving body of water, and the entire wheel was turned as the river flowed past it, pushing against its paddles.This was a prototype for what came to be called an impulse turbine, which is one that is driven by the force of a fluid directly striking it. The undershot waterwheel was followed during medieval times by the overshot

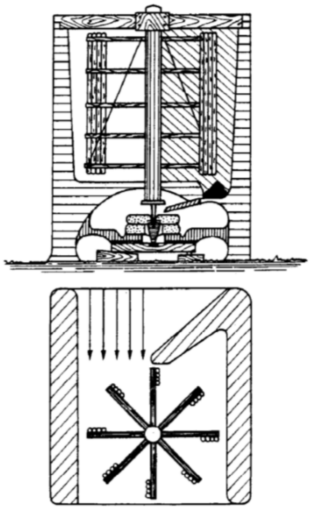

(a) Persian windmill

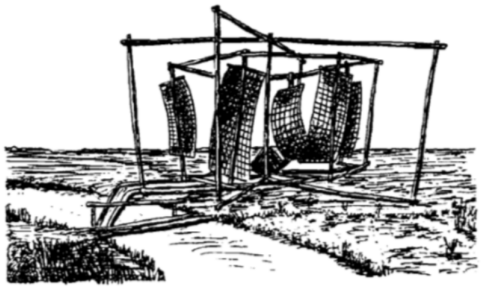

(b) Chinese windmill

Figure 2.1.1: Windmill

wheel. This first made its appearance in Germany and became the prototype for the modern reaction turbine.
Contrasted to the impulse turbine whose energy source is kinetic energy, the energy source for an overshot wheel (or reaction turbine) is known as potential energy. This Is because it is the weight of the water acting under gravity that is used to turn the wheel. Renaissance engineers studied the waterwheel and realized that the action of water on a wheel with blades would be much more effective if the entire wheel were somehow enclosed in a kind of chamber. They knew very well that only a small amount of the water pushing or falling on a wheel blade or paddle actually strikes it, and that much of the energy contained in the onrushing water is lost or never actually captured. Enclosing the wheel and channeling the water through this chamber would result in a machine of greater efficiency and power. They were hampered, however, by a lack of any theoretical understanding of hydraulics as well as by a lack of precision machine tools with which they could carefully build things. Both of these problems were resolved to some degree in the eighteenth century [14], and one of the earliest examples of a reaction turbine was built in 1750 by the German mathematician and naturalist Johann Andres von Segner (1704-1777). In his system, the moving water entered a cylindrical box containing the shaft of a runner or rotor and flowed out through tangential openings, acting with its weight on the inclined vanes of the wheel.
A really efficient water turbine was now within reach it appeared, and a prize was offered in France by the Societe d'Encouragement pour l'Industrie Nationale. The prize was won by the French mining engineer Claude Burdin who improved and developed his master's work and who is considered to be the inventor of the modern hydraulic turbine. Fourneyron built a six-horsepower turbine and later went on to build larger machines that worked under higher pressures and delivered more horsepower. His main contribution was his addition of a distributor which guided the water flow so that it acted with the greatest efficiency on the blades of the

wheel. His was a reaction type turbine, since water entering through the vanes of the distributor (that was fitted inside the blades) then acted on the blades of the wheel. Following Fourneyron's first turbine, which happened to be a hydraulic or water turbine, other turbines were developed that used the energy of a different material like gas or steam. Although these different types of turbines have different means of operation and certainly different histories, they still embody the basic characteristics of a turbine. They all spin, or receive their energy from some form of a moving fluid, and they all convert it into mechanical energy.

## 2.2 Classification

Water turbines are generally divided into two categories:

- **Impulse turbines**
  The impulse turbine generally uses the velocity of the water to move the runner and discharges to atmospheric pressure. The water stream hits each bucket on the runner. There is no suction on the down side of the turbine, and the water flows out the bottom of the turbine housing after hitting the runner. An impulse turbine is generally suitable for high head, low flow applications.

- **Reaction turbines**
  A reaction turbine develops power from the combined action of pressure and moving water. The runner is placed directly in the water stream flowing over the blades rather than striking each individually. Reaction turbines are generally used for sites with lower head and higher flows than compared with the impulse turbines.

These two classes include the main types in common use-namely, the Pelton impulse turbine and the reaction turbines of the Francis, propeller, Kaplan, and Deriaz variety. Turbines can be arranged with either horizontal or, more commonly, vertical shafts. Wide design variations are possible within each type to meet the specific local hydraulic conditions [15]-[16].

### Impulse turbines

- **Pelton**
  A Pelton wheel has one or more free jets discharging water into an aerated space and impinging on the buckets of a runner. Draft tubes are not required for impulse turbine since the runner must be located above the maximum tailwater to permit operation at atmospheric pressure.
  A Turgo Wheel is a variation on the Pelton and is made exclusively by Gilkes in England. The Turgo runner is a cast wheel whose shape generally resembles a fan blade that is closed on the outer edges. The water stream is applied on one side, goes across the blades and exits on the other side.

- **Cross-Flow**
  A cross-flow turbine is drum-shaped and uses an elongated, rectangular-section

nozzle directed against curved vanes on a cylindrically shaped runner. It resembles a "squirrel cage" blower. The cross-flow turbine allows the water to flow through the blades twice. The first pass is when the water flows from the outside of the blades to the inside; the second pass is from the inside back out. A guide vane at the entrance to the turbine directs the flow to a limited portion of the runner. The cross-flow was developed to accommodate larger water flows and lower heads than the Pelton.

### Reaction turbines

- **Propeller**
  A propeller turbine generally has a runner with three to six blades in which the water contacts all of the blades constantly. Picture a boat propeller running in a pipe. Through the pipe, the pressure is constant; if it isn't, the runner would be out of balance. The pitch of the blades may be fixed or adjustable. The major components besides the runner are a scroll case, wicket gates, and a draft tube. There are several different types of propeller turbines:

  - *Bulb turbine:* The turbine and generator are a sealed unit, placed directly in the water stream.
  - *Straflo:* The generator is attached directly to the perimeter of the turbine.
  - *Tube turbine:* The penstock bends just before or after the runner, allowing a straight line connection to the generator.
  - *Kaplan:* Both the blades and the wicket gates are adjustable, allowing for a wider range of operation.

### Kinetic turbines

The Kinetic energy turbine are powered by kinetic energy instead of potential energy. The term 'Hydrokinetic Turbine' has long been interchangeably used with other synonyms such as "zero-head" or "ultra-low" turbine, "in-stream" turbine, water current turbine(WCT). The systems may operate in rivers, man-made channels, tidal waters, or ocean currents. Kinetic systems utilize the water stream's natural pathway. They do not require the diversion of water through manmade channels, riverbeds, or pipes, although they might have applications in such conduits. Kinetic systems do not require large civil works; however, they can use existing structures such as bridges, tailraces and channels.

## 2.3 Hydrokinetic Turbine

Water current turbines, or hydrokinetic turbines, produce electricity directly from the flowing water in a river or a stream. No dam or artificial head is needed to produce the small-scale power output. Two main areas where hydrokinetic devices

can be used for power generation purposes are tidal currents and river streams. Because of low investment costs and maintenance fees, this technology is cost effective in comparison to other technologies. This kind of hydropower is considered environmentally friendly, meaning that the water passing through the generator is directed back into the stream with relatively small impact on the surrounding ecology.
The energy flux of the water stream is dependent on the density, cross-sectional area and velocity cubed [17].

$$P = \frac{1}{2}\rho C_P A U^3$$

$P$ =Power $[Watt]$;
$\rho$ =Water density $[kg/m^3]$;
$C_P$ =Power coefficient;
$A$ =Turbine area $[m^2]$;
$U$ =Velocity $[m/s]$;

The traditional hydroelectric plants always have a large capacity for the electrical generation, but the costs and environmental impacts on constructing a dam are the main problem, so most of the hydrokinetic power systems are small-scale electrical generation sets, which operate in a "free-flow" environment that does not require the damming or diversion of rivers. Free-flow deployment does not disrupt natural ecosystems or interfere with aquatic and marine life. Additionally, in some hydrokinetic energy deployment situations, hydrokinetic systems flexibly operated with multi-unit arrays, which would extract energy from flowing current in a similar way to wind farm. The depth of the foundation of a hydrokinetic system and the spacing between systems are determined by the site conditions such as water depth and current flow. Like some other renewable energy sources, hydrokinetic power is variable, because the generation changes with the fluctuations in water speed. Unlike wind and solar power, the variability of hydrokinetic power is highly predictable according to seasonal statistics. Even though hydrokinetic turbine has lower environmental impact, it cannot replace the role of conventional hydro plants. In conclusion, as an alternative energy source, hydrokinetic systems are highly recommended for remote communities or coastal communities.
The hydrokinetic energy conversion device and the wind turbine system work in a similar way. When the water speed is large enough, a net positive power is produced by the hydrokinetic system. Because of the characteristic of the hydrokinetic turbine, there is only one optimal point producing the maximum power for each tip speed ration, and the optimal operation point is determined by the water speed and shaft rotational speed. Because the water speed is uncontrollable, the rotor speed can be adjusted to achieve the maximum power [18].

## 2.4 Hydrokinetic System

A complete hydrokinetic system for use in river environment may consist of units such as augmentation channel, rotor-blade assembly, electrical generator, floating device, mooring, control system, protection screen, etc. Since the discussion of

all these components goes beyond the scope of this work, only the rotors and the chennelling devices will be considered here [19].

### 2.4.1 Rotor Configurations

The choice of turbine rotor configuration requires considerations of a brad array of technical and economical factors. As an emerging field of energy conversion, these issues become even more dominant for hydrokinetic turbines. A general classification of water turbines justified on their physical arrangements is given in figure 2.4.1. Based on the alignment of the rotor axis with respect to water flow, two generic classes could be formed, namely, the axial and cross flow turbines.

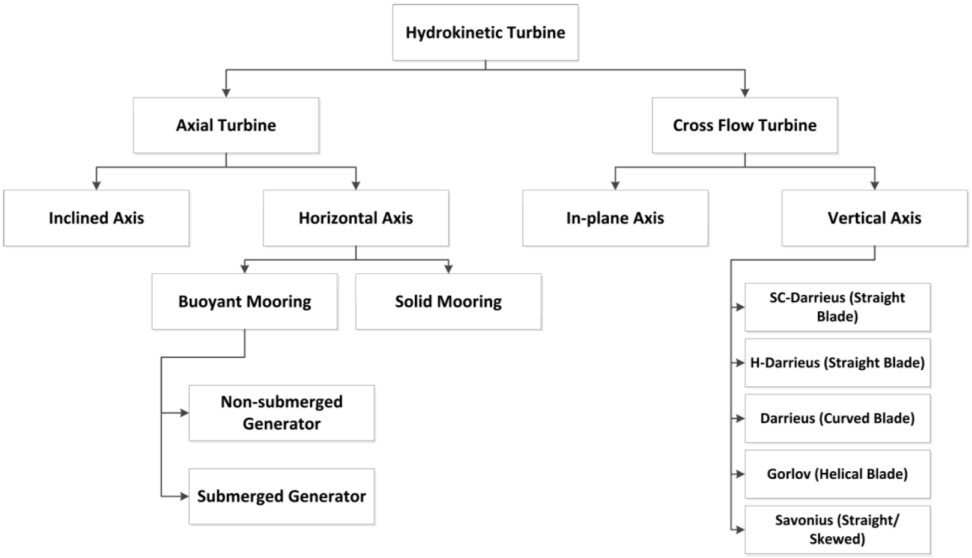


Figure 2.4.1: Classification of hydrokinetic turbines

The axial turbines have axes parallel to the fluid flow and employ propeller type rotors. On the other hand, the cross flow types encounter water flow orthogonal to the rotor axis and mostly appear as cylindrical rotating structures. Various arrangements of axial turbines for use in hydro environment are shown in figure 2.4.2. Inclined axis turbines have mostly been studied for small river energy converters. Horizontal axis turbines are common in tidal energy converters and are very similar to modern day wind turbines from design and structural point of view. Turbines with solid mooring structure require the generator unit to be placed near the river or seabed. Horizontal axis rotors with a buoyant mooring mechanism may allow a non-submerged generator to be placed closer to the water surface.

Various arrangements under the cross flow turbine category are given in figure 2.4.3. The turbines can rotate unidirectionaly even with bi-directional fluid flow. These can also be divided into two groups: vertical axis (axis vertical to water plane) and in-plane axis (axis on the horizontal plane of water surface). In-plane axis turbines are better known as floating waterwheels. These are mainly

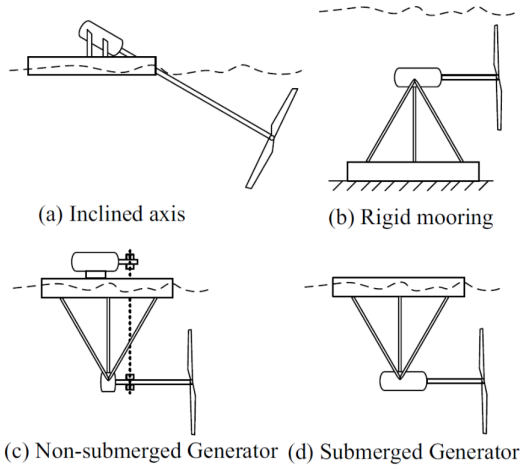


Figure 2.4.2: Axial flow turbines

drag based devices and inherently less efficient than their lift based counterparts. The large amount of material usage is another problem for such turbines. Darrieus turbines with in-plane axes may also fall under this category. But such systems are less common and suffer from bearing and power take-off problems. In the vertical axis domain, Darrieus turbines are the mos prominent options. Even though examples of H-Darrieus or Squirrel Cage Darrieus (straight bladed) are rather common, istances of Darrieus turbines (curved baldes) being used in hydro applications are non-existent. The Gorlov turbine is another member of the vertical axis family, where the blades are of helical structure. Savonious turbine are drag type devices, which may consist of straight or skewed blades.

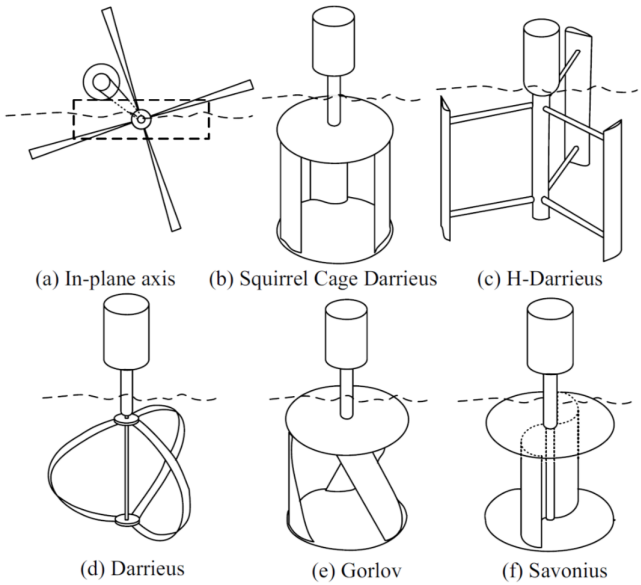


Figure 2.4.3: Cross-Flow Turbines

Hydrokinetic turbines may also be classified based on their lift/drag properties, orientation to up/down flow, and fixed/variable (active/passive) blades pitch mechanism. Different types of rotors may also be hybridized (such as, Darrieus- Savonius hybrid) in order to achieve certain performance features [19]-[20].

### 2.4.2 Technical advantages and disadvantages of horizontal and vertical turbines

It is worthwhile to investigate the opportunities and challenges associated with various hydrokinetic turbine systems, especially when this sector of energy engineering is mostly at the design and development phase. Of particular interest is a review of both horizontal and vertical axis configurations with regard to their technical merits and drawbacks [21].
Vertical axis turbines, especially the straight bladed Darrieus types have gained considerable attention owing to various favourable features such as:

- **Design simplicity:** As an emerging technology, design simplicity and system cost are important factors that may determine the success of hydrokinetic turbine technology. In contrast to horizontal axis turbines where blade design involves delicate machining and manufacturing, use of straight blades make the design potentially simpler and less expensive;

- **Generator coupling:** For hydrokinetic applications, generator coupling with the turbine rotor involves a special challenge. In the horizontal axis turbines, this could be achieved by a right-angled gear coupling, long inclined shaft or underwater placement of the generator. In vertical axis turbines, the generator can be placed in one end of the shaft, allowing the generator to be placed above the water surface. This reduces the need and subsequent cost in arranging water-sealed electric machines;

- **Flotation and augmentation equipment:** The cylindrical shape of the Darrieus turbine allows convenient mounting of various curvilinear or rectilinear ducts. These channels can also be employed for mooring and floating purposes. For axial-flow turbines, ducts can not be easily used for flotation purposes;

- **Noise emission:** Vertical turbines generally emit less noise than the horizontal turbine concepts due to reduced blade tip losses. Subject to further research and investigation, this may prove to be beneficial in preserving the marine-life habitat;

- **Skewed flow:** The vertical profile of water velocity variation in a channel may have significant impact on turbine operation. In a shallow channel, the upper part of a turbine faces higher velocity than the lower section. Vertical turbines, especially the ones with helical/inclined blades are reportedly more suitable for operation under such conditions;

The disadvantages associated with vertical axis turbines are:

- **Low starting torque:** depending on their design, these turbines generally possess poor starting performance. This may require special arrangement for external electrical, mechanical, or electromechanical starting mechanisms;
- **Torque ripple:** The blades of a vertical turbine unit are subject to cyclic tangential pulls and generate significant torque ripple in the output;
- **Lower efficiency:** Cavitation and fatigue loading due to unsteady hydrodynamics are other concerning issues associated with vertical turbines;

Axial-flow turbines on the other hand, eliminate many of these drawbacks. In addition, various merits of such rotors are:

- **Knowledgebase:** Literature on system design and performance information of axial type rotors is abundant. Advancements in wind engineering and marine propellers have significantly contributed to this field. Use of such rotors have been successfully demonstrated for large scale applications (10–350 kW), especially for tidal energy conversion;
- **Performance:** One of the main advantages of axial type turbines is that all the blades are designed to have sufficient taper and twist such that lift forces are uniformly applied along the blade. Therefore, these turbines are self-starting. Also, their optimum performance is achieved at higher rotor speeds, and this simplifies the problem of generator matching, allowing reduced gear coupling;
- **Control:** : Various control methods (stall or pitch regulated) of axial type turbines have been studied in great details. Active control by blade pitching allows greater flexibility in over speed protection and efficient operation;

The major technical challenges encountered with axial type rotors are:

- **Blade design;**
- **Underwater generator installation;**
- **Underwater cabling;**

### 2.4.3 Duct Augmentation

Whether the turbine is ducted or not plays an important role in the performance of the turbine. Augmentation channels induce a sub-atmospheric pressure within a constrained area and thereby increase the flow velocity. If a turbine is placed in such a channel, the flow velocity around the rotor is higher than that of a free rotor. This increases the possible total power capture significantly. In addition, it may help to regulate the rotor speed and impose lesser system design constraints as as the top of the flow rate is reduced. Such devices have been widely tested in

the wind energy domain. A survey conducted with 76 hydrokinetic system concepts show that around one-third of the horizonal axis turbines are being considered for such arrangements. On the contrary, vertical axis turbines are being given attention when it comes to duct augmentation. Almost half of the study systems consider some form of augmentation scheme to be incorporated with the vertical turbine [21].
The ducts for horizontal axis turbines mostly take conical shapes (for operation under unidirectional flow) as opposed to vertical turbines where the channels are of rectangular cross-section. This imposes a design asymmetry and subsequent structural vulnerability for the former type. The lesser number of duct augmentation being considered for horizontal axis turbines can be attributed to these issues. A simplified classification of various channel designs are given in figure 2.4.5 and in figure 2.4.4. A simple channel may consist of a single nozzle, cylinder (or straight path) with brim or diffuser. In a hybrid design, all three options may be incorporated in one unit.

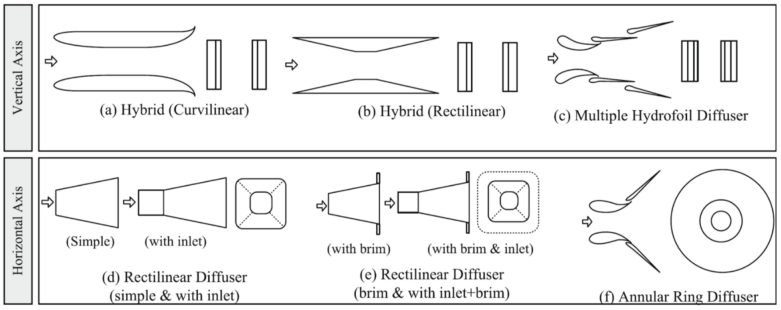


Figure 2.4.4: Channel shapes (Top and Side view)

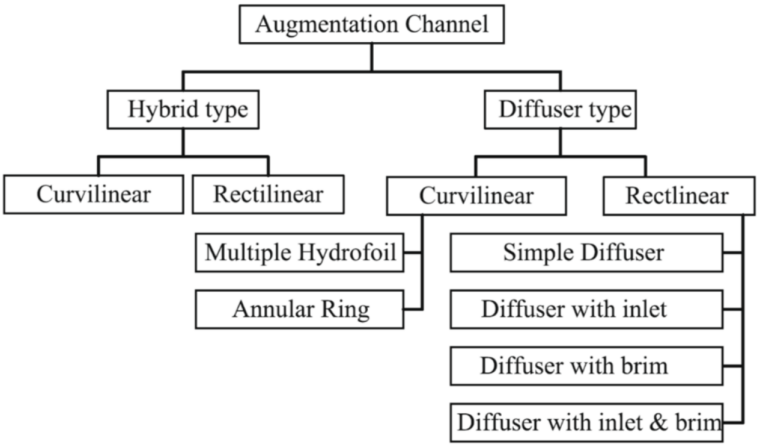


Figure 2.4.5: Augmentation channels

### 2.4.4 Rotor Placement

While the type of rotor to be deployed and duct augmentation to be incorporated are of fundamental importance, placement of the system in a channel also deserves attention. A turbine may incorporate bottom structure mounting (BSM) arrangement where the converter is fixed near the seafloor/riverbed. Also, turbine units may operate under variable elevation if a floating structure mounting (FSMM) is devised. The last option is to mount the converter with a structure that is closer to the surface (near-surface structure mounting NSM) (see figure 2.4.6).

The axial-flow turbines are given almost equal consideration for the three options outlined above. However, more than half of vertical axis turbines are being considered for near-surface placement. This probably arises from the fact that this option allows the generator and other apparatus to be placed above the water level. However, at the present state of this technology, there is no clear direction on the most attractive option. Several aspects that can be observed in this regard are highlighted below:

- *Energy capture:* The energy flux in a river/tidal channel is higher near the surface. This suggests that the FSM option is the best options as long energy extraction is the prime concern. In contrast, the BSM method allows only sub-optimal energy capture. Also, energy capture using the NSM scheme would see fluctuating output subject to variations in river stage.

- *Competing users:* While placing a turbine at the surface of a channel seems attractive, competing users of the water resource may object to such arrangement. Fishing, shipping, recreational boating and many other activities may leave the BSM or NSM methods as the only option. Floating structures are still possible but these need to be placed closer to the shore where energy resources may appear limited.

- *Construction challenge:* Experience of floating structure design for energy harvesting is limited. In contrast, knowledge in civil engineering domain for bottom mounted structures (e.g. bridges, offshore oil and has platforms) are quite abundant.

- *Footprint:* Any trenching, piling or excavation at the riverbed may become subject to environmental scrutiny. Floating or near-surface structures appear more permissible in this context.

- *Design and operation constraints:* Depending on where a turbine is to be placed various power conversion apparatus (generator, bearing, gearboxes and power conditioning equipment) would require special design considerations such as, water sealing, lubrification and protection. Also, variation of water velocity and stage will impose operational constraints. Due attention is also required to address the challenges associated with sever-storm conditions, especially for the near surface and floating-type systems.

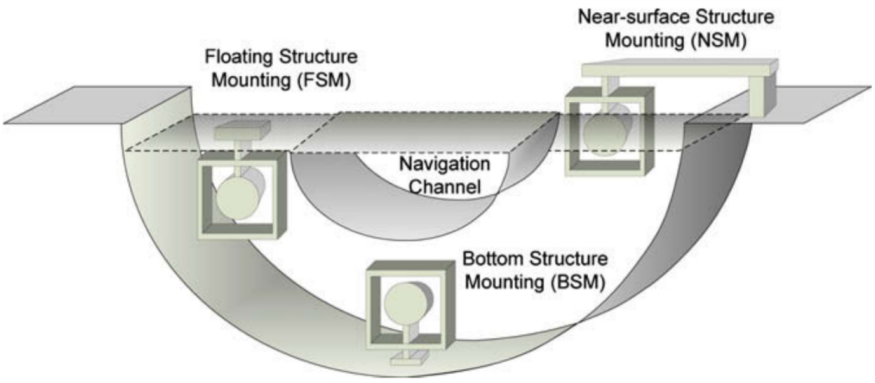


Figure 2.4.6: Turbine mounting options

# Chapter 3

# Hydrokinetic turbine configuration

As mentioned in section 2.4.1, turbines may be classified according not only by the position of the axis of rotation, but also by the kind of principle used: lift or drag; all types of turbines have benefits and drawbacks, which means that hybrid solutions are also available.
Another classification of turbines types is by orientation of the flow relative to the rotational axis. Axial flow turbines has the axis and hub of the turbine in the same direction as the freestream flow. These are the most common types of devices used for large-scale commercial wind and proposed commercial marine applications, owing to their high efficiency. Maximum water-to-wire efficiency for some marine devices is around 50% (Polagye et al., 2011). The conventional axial flow windmill turbine design is not ideal for a micropower application. One reason is that the axis of the turbine needs to be aligned with the current to achieve reasonable efficiencies. A control yaw mechanism increas design complexity and introduce a parasitic power loss.
A cross-flow turbine has its axis of rotation perpendicular to the freestream velocity, as in a Darrieus rotor or Savonius rotor. Cross-flow turbines tend to show slightly lower efficiency than axial-flow turbines, but they are advantageous for a micropower application for several reasons. First of all, they can accept and operate with equal efficiency with a freestream flow from any horizontal direction without yaw control. Secondly, they have a symmetric design that makes them a more balanced installation. Several cross-flow turbine designs are described in more detail in the following sections [22].

## 3.1 Vertical axis

The main vertical axis turbines, which for the first time were designed for wind applications, are named in honour of their inventors:

1. Darrieus turbines;

2. Savonius turbines;

3. Gorlov turbines;

4. Hybrid turbines;

The design of vertical axis turbines is made more difficult by the stall phenomenon.
Stall conditions of an airfoil are reached when the ratio between the absolute speed of the current and the speed of the rotor exceeds a certain limit predetermined by the type of profile adopted. The flow lines deviate from the profile, creating vortices that reduce the lifting capacity to zero and, at the same time, increasing the resistance component.
The torque and power extracted collapses to zero, erasing the useful effect of the machine [23].

### 3.1.1 Darrieus Turbine

The Darrieus turbine is based on the principle of lift, patented by George Darrieus in 1931. The lift force is generated by the movement of the fluid around an airfoil at an angle relative to the blade chord (known as the angle of attack), which causes a pressure difference from one side of the blade to the other. The lift force acts perpendicularly to the angle of relative fluid velocity. A drag force is also developed by the fluid acting on the airfoil, which normally impedes rotation, but for lift devices the average tangential force developed by lift overcomes the retarding drag force, and the net tangential force acting at a radius on the turbine blade generates positive torque and power [22]. These turbines are widely used because they are able to produce the same power as the best horizontal axis turbines in widespread use. The name Darrieus refers to three kinds of vertical axis turbines: the "eggbeater", "H-type", and the "helical Darrieus", which differ only in the shape of the blades, but all of them work using the lift created by the shape of the blades [23].

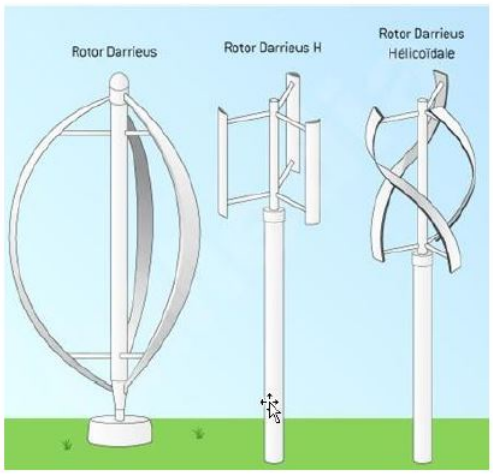


Figure 3.1.1: Types of Darrieus turbines

The advantages of this type of turbine are:

- High efficiency operation: Darrieus turbines are quite commonly used for wind and marine energy systems, in part due to their high operating speed, but also due to their fairly high efficiencies, as numerous test results have indicated. Testing of a 2-bladed 17-meter troposkein wind turbine by Sandia National Labs resulted in a power coefficient of 38% (Worstell, 1978). Darrieus straight-bladed turbines used for tidal turbine generation have been tested and are documented in several sources (e.g., Khan, 2008; Dai & Lam, 2009). An example is Shiono et al. (2002), who reported Darrieus turbine efficiencies for a marine turbine as high as $\approx 33\%$ for 1.2 m/s flow [22];

- Low loads on the blades;

On the other hand, some disadvantages are:

- Lack of self-starting: To have a lift-force on the blades that can drive the generator, the rotor must be pushed to a minimum speed that often occurs only under ideal conditions.

- Vibrations in the shaft due to torque variations, known as "torque ripple". Darrieus turbines can take a variety of forms, but are all characterised by all points on each blade having the same azimuthal angle, $\theta$ , at any time. Since the hydrodynamic forces acting upon the blade are a function of blade angle of attack,$\alpha$ (which is a function of $\theta$) the blade forces vary with time as the blades rotate. This in turn means that the shaft torque will fluctuate over time, known as torque ripple, which can cause vibrations in the shaft and potentially damage the turbine [24]. The torque oscillation problem is prevalent at low tip speed ratio, but is gradually diminished at higher tip speed ratio (Khan et al., 2010). The oscillation increases fatigue of the blades (Gorlov, 1998). The electrical power output will also exhibit an oscillatory behavior when the turbine is loaded (Khan et al., 2010) [22].

Both self-start and torque oscillation in the Darrieus turbine have been addressed in various ways. Two common methods are manipulating the blade shape to provide better starting torque or higher lift at low Reynolds number, or using a hydrid turbine configuration [22].

### 3.1.2 Savonius Turbine

The Savionius turbine, invented by a Finnish engineer Sigurd Savonius, uses the action of dragging the current to turn the blades. This turbine has no stall problems and can operate even at minimum current speeds (figure 3.1.3). The primary motive force is due to the stagnation pressure of the fluid pushing against the profile of the turbine cup, paddle, or blade (Alam & Iqbal, 2009).The cups are attached to a central rotating shaft or a conveyor-style attachment. The cups are normally designed such that the force of the fluid against the retreating cup is greater than the force of the fluid against the advancing cup. The differential force acting at a radius causes torque and rotation [22]. figure 3.1.4. At this point the process is

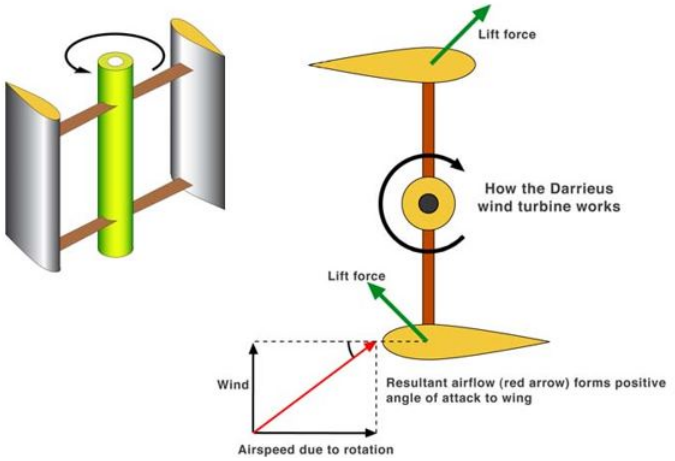


Figure 3.1.2: Darrieus turbine configuration

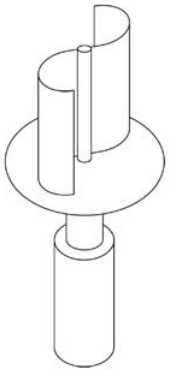

Figure 3.1.3: Savonius turbine

repeated, resulting in a continuous rotation.

The main advantages of this turbine are:

- Possibility of working even at low speeds while at the same time improving self-starting conditions;
- Like all vertical axis turbines, Savonius turbine is also able to accept current in all directions;
- Possibility to have a hybrid solution with the Darrieus turbine to solve the problem of self-starting;
- Easy to build, they often have simple bowl, flat plate or cylindrical shapes, compared to lift style devices that usually incorporate an airfoil shape and are more complex.

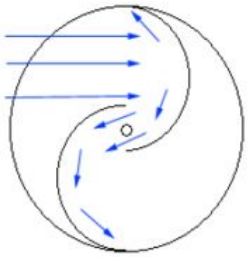

Figure 3.1.4: Savonius's principle working

The main disadvantages of this turbine are:

- Low efficiency operation: Several authors have tested the parameters of the Savonius rotor in order to optimise its efficiency, even modifying its conventional design. A good summary of experimental performance testing of the Savonius rotor was given by Ushiyama & Nagai (1988). Ushiyama & Nagai tested several parameters of the device, including gap ratio, aspect ratio, number of cylindrical buckets, number of stages, endplate effects, overlap ratio, and bucket design (noted in the figure 3.1.5 are (a) gap, (d) bucket diameter, (e) overlap and (R) rotor radius).The highest efficiency of all configurations tested was $\approx$ 24 % for a two-stage, two-bucket rotor;

- Drag devices operate normally at a tip speed ratio below unity, as they cannot rotate faster than the free stream (Alam & Iqbal, 2009). The slow rotational speed of drag devices makes them more difficult to integrate with a generator without a high ratio gearbox to step up the rotational speed [22].

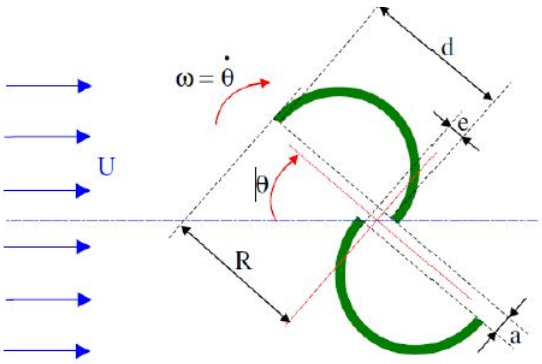


Figure 3.1.5: Savonius's details, Menet(2004)

### 3.1.3 Hybrid turbine

In order to overcome the self-start problem for the Darrieus turbine, some designers have tested different kinds of turbines on the Darrieus type. A particular solution is to combine a large Darrieus turbine with a small Savonious rotor, on the same rotational axis( Alam & Iqbal (2009)). The intent is to provide a better torque of the turbine during the phases of starting using the good inizial torque and performance of the Savonius rotor at tip speed ratio below unity. Once the rotor gets to sufficiently high rotational speed, lift forces generated by the Darrieus turbine blades allow the turbine to spin up to full operating speed. One obvious design challenge of a Darrieus-Savonius hybrid design is the different optimum tip speed ratio of the two devices. While a Savonius rotor generates optimum lift with $\lambda \leq 1$, a Darrieus turbine optimum tip speed ratio is much higher than unity (actual optimum depends on blade design, size and solidity). The two rotors must be appropriately sized so that their optimum tip speed ratio coincide to the same rotational speed. Otherwise, the turbine may spin up to an angular velocity that exceeds the Savonius rotor peak operating point. Wakui, et al. (2005) built and tested a hybrid Savonius-Darrieus wind turbine rotor that accomplished power coefficient up to $\approx 22.5\%$. The hybrid turbine performed similarly to the Darrieus turbine alone in terms of power coefficient but had improved starting torque. Alam & Iqbal (2009) designed and built a similar turbine for marine current applications but experimental results had very low power output [22].

### 3.1.4 Gorlov Turbine

The helical turbine was invented by Alexander Gorlov (1995) and is also known as the Gorlov turbine. The helical turbine is similar to a Darrieus straight-bladed style turbine, except the airfoil blade profile is swept in a helix profile along its span. A diagram of a four-bladed helical turbine is shown in figure 3.1.6.

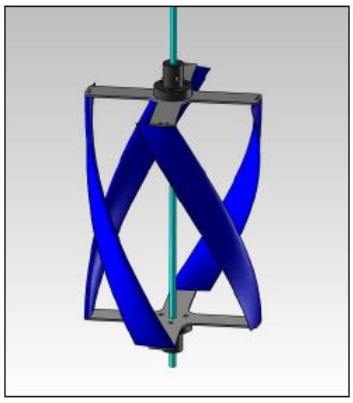

Figure 3.1.6: Four blade Gorlov turbine

One of the advantages of the helical blade is that it improves the self-start of the turbine compared to a Darrieus turbine (Gorlov, 1998). As the helical blade

shape sweeps along the circumference of rotation of the turbine, some portion of the blade profile is located at the optimum angle of attack even in static or slowly rotating conditions, which allows for a more uniform starting torque that less dependent upon turbine azimuthal position. In addition, the helical blade shape permit the reduction of torque oscillation during rotation (Gorlov, 1998). A Darrieus turbine tends to experience torque oscillation resulting from the circumferential void space between the discrete blade positions. A helical turbine with a full blade wrap around its circumference does not experience this problem; the uniform blade coverage, neglecting end effects and wake dynamics, ideally give the turbine fully uniform torque, although in reality some variation is likely to occur. [22]

## 3.2 Horizontal axis

Horizontal hydrokinetic turbines are classified into axial and cross-flow. Cross-flow turbines, often known in tidal energy field as transverse horizontal axis water turbine (THAWT), have the same types of blades already seen for vertical axis turbines, such as Gorlov and Savonius, which are adapted according to the application (figure 3.2.1a). On the other hand, the axial hydrokinetic turbines are inspired by the classic wind turbines, re-designed to work in water (figure 3.2.1b).

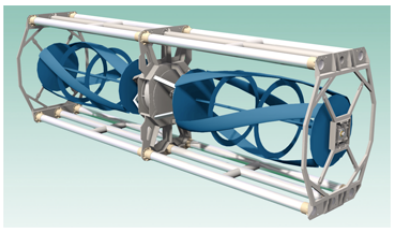

(a) THAWT

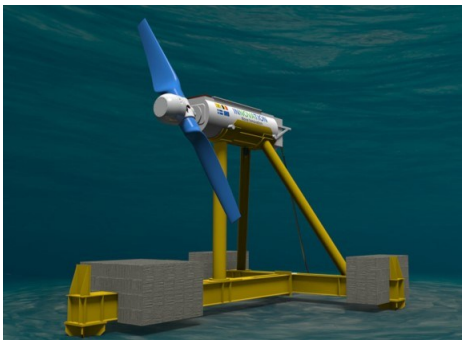

(b) Tidal turbine

Figure 3.2.1: Horizontal axis water turbine

# Chapter 4

# Turbine theory and mathematical modelling

It is believed that there is a similarity in the working principles between the water current turbine and the wind turbines. This is because that the water current turbine extracts the kinetic energy of a moving fluid, a similar mechanism to that of the wind turbine (Khan 2007). Some literatures in Guney (2010), Rourke (2010) , Li (2010) and Anyi (2010) show that the most of the turbines for the water current, such as river and marine turbines, have a similar appearance to the wind turbines [25]. Hence, the following sections will refer to the wind theory, as it was the first one developed in the past.

## 4.1 Betz theory and optimal tip speed ratio (TSR)

Typical analysis of wind and water turbines is done by applying the Betz analysis in order to determine the efficiency of the turbine and the energy available in the fluid flow [26].
The fundamental theory of design and operation of wind turbines is derived based on a first principles approach using conservation of mass and conservation of energy. This fundamental equation was first introduced by the German engineer Albert Betz in 1919 and published in his book " Wind energy and its extraction through windmills" in 1926. The theory that is developed can be used for both horizontal and vertical axis turbines.
The Betz equation is analogous to the Carnot cycle efficiency in thermodynamics suggesting that a heat engine cannot extract all the energy from a given source of energy and must reject part of its heat input back to the environment. Whereas the Carnot cycle efficiency can be expressed in term of the Kelvin isothermal heat input $T_1$ and the Kelvin isothermal heat rejection temperature $T_2$:

$$\eta_{Carnot} = \frac{T_1 - T_2}{T_1}$$

The Betz equation deals with the wind speed upstream of the turbine $U_1$ and the downstream wind speed $U_2$. The limited efficiency of a heat engine is caused by

heat rejection to the environment. The limited efficiency of a wind turbine is caused by breaking of the wind form its upstream speed $U_1$ to its downstream speed $U_2$, while allowing a continuation of the flow regime. The additional losses in efficiency for a practical wind turbine are caused by the viscous and pressure drag on the rotor blades, the swirl imparted to the air flow by the rotor, and the power losses in the transmission and electrical system. The wind rotor is assumed to be an ideal energy converter, meaning that:

1. It does not possess a hub;
2. It possesses an infinite number of rotor blades which do not result in any drag resistance to the wind flowing through them;

In addition, uniformity is assumed over the whole area swept by the rotor, and the speed of the air beyond the rotor is considered to be axial. The ideal wind rotor is taken at rest and is placed in a moving fluid atmosphere. Considering the ideal model shown in figure 4.1.1, the cross sectional area swept by the turbine blade is designated as S, with the air cross-section upwind from the rotor designated as $A_1$, and downwind as $A_2$. The wind speed passing through the turbine rotor is considered uniform as U, with its value as $U_1$ upwind, and as $U_2$ downwind at a distance from the rotor. Extraction of mechanical energy by the rotor occurs by reducing the kinetic energy of the air stream from upwind to downwind, or simply applying a braking action on the wind. This implies that:

$$U_2 < U_1$$

Consequently the air stream cross sectional area increases from upstream of the turbine to the downstream location, and:

$$A_2 > A_1$$

If the air stream is considered as a case of incompressible flow, the conservation of mass or continuity equation can be written as:

$$\dot{m} = \rho A_1 U_1 = \rho A U = \rho A_2 U_2 = constant \tag{4.1.1}$$

This expresses the fact that the mass flow rate is a constant along the wind stream. Continuing with the derivation, Eulero's Theorem gives the force exerted by the wind on the rotor as:

$$F = ma = m\frac{dU}{dt} = \dot{m}\Delta U = \rho A U(U_1 - U_2) \tag{4.1.2}$$

The incremental energy or the incremental work done in the wind stream is given by:

$$dE = Fdx$$

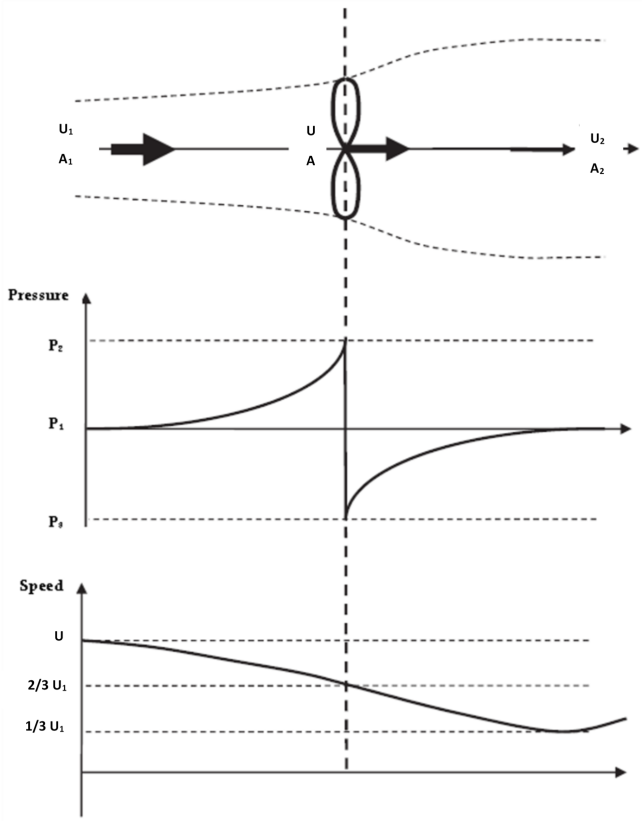


Figure 4.1.1: Pressure and speed variation in an ideal model of a wind turbine.

From which the power content of the wind stream is:

$$P = \frac{dE}{dt} = F\frac{dx}{dt} = FU$$

Substituting for the force $F$ from Eqn. (4.1.2), we get for the extractable power from the wind:

$$P = \rho A U^2 (U_1 - U_2) \tag{4.1.3}$$

The power as the rate of change in kinetic energy from upstream to downstream is given by:

$$P \simeq \frac{\Delta E}{\Delta t} \simeq \frac{\frac{1}{2}mU_2^2 - \frac{1}{2}mU_1^2}{\Delta t} = \frac{1}{2}\dot{m}(U_1^2 - U_2^2)$$

Using the continuity equation (4.1.1), we can write:

$$P = \frac{1}{2}\rho A U (U_1^2 - U_2^2) \tag{4.1.4}$$

Equating the two expressions for the power $P$ in Eqns. (4.1.3) and (4.1.4), we get:

$$P = \rho A U^2 (U_1 - U_2) = \frac{1}{2}\rho A U (U_1^2 - U_2^2)$$

The last expression implies that:

$$\frac{1}{2}(U_1^2 - U_2^2) = \frac{1}{2}(U_1 - U_2)(U_1 + U_2) = U(U_1 - U_2), \quad \forall U, A, \rho \neq 0$$

Or:

$$U = \frac{1}{2}(U_1 + U_2), \quad \forall (U_1 - U_2) \neq 0 \quad or \quad U_1 \neq U_2$$

This in turn suggests that the wind velocity at the rotor may be taken as the average of the upstream and downstream wind velocities. It also implies that the turbine must act as a brake, reducing the wind speed from $U_1$ to $U_2$, but not totally reducing it to $U = 0$, at which point the equation is no longer valid. To extract energy from the wind stream, its flow must be maintained and not totally stopped. The last result allows us to write new expressions for the force $F$ and power $P$ in terms of the upstream and downstream velocities by substituting for the value of $U$ as:

$$F = \rho A U(U_1 - U_2) = \rho A \frac{1}{2}(U_1^2 - U_2^2) \tag{4.1.5}$$

$$P = \rho A U^2(U_1 - U_2) = \frac{1}{4}\rho A(U_1^2 - U_2^2)(U_1 + U_2)$$

We can introduce the "downstream velocity factor," or "interference factor," $b$ as the ratio of the downstream speed $U_2$ to the upstream speed $U_1$ as:

$$b = \frac{U_2}{U_1}$$

From equation (4.1.5) the force $F$ can be expressed as:

$$F = \rho A \frac{1}{2} U_1^2 (1 - b^2)$$

The extractable power P in terms of the interference factor b can be expressed as:

$$P = \frac{1}{4}\rho A(U_1^2 - U_2^2)(U_1 + U_2) = \frac{1}{4}\rho A U_1^3 (1 - b^2)(1 + b) \tag{4.1.6}$$

The most important observation pertaining to wind power production is that the extractable power from the wind is proportional to the cube of the upstream wind speed $U_1^3$ and is a function of the interference factor $b$. The "power flux" or rate of energy flow per unit area, sometimes referred to as "power density", is defined using equation (4.1.3) as:

$$P_F = \frac{P}{A} = \frac{\frac{1}{2}\rho A U^3}{A} = \frac{1}{2}\rho U^3 \quad \left[\frac{Watt}{m^2}\right]$$

The kinetic power content of the undisturbed upstream wind stream with $U = U_1$ and over a cross sectional area $A$ becomes:

$$P_{available} = \frac{1}{2}\rho A U_1^3 \quad [Watt] \tag{4.1.7}$$

The performance coefficient or efficiency is the dimensionless ratio of the extractable power $P$ to the kinetic power $P_{available}$ available in the undisturbed stream:

$$C_p = \frac{P}{P_{available}}$$

The performance coefficient is a dimensionless measure of the efficiency of a wind turbine in extracting the energy content of a wind stream. Substituting the expressions for $P$ from equation (4.1.6) and for $P_{available}$ from equation (4.1.7) we have:

$$C_P = \frac{P}{P_{available}} = \frac{\frac{1}{4}\rho A U_1^3 (1 - b^2(1+b))}{\frac{1}{2}\rho A U_1^3} = \frac{1}{2}(1-b^2)(1+b) \tag{4.1.8}$$

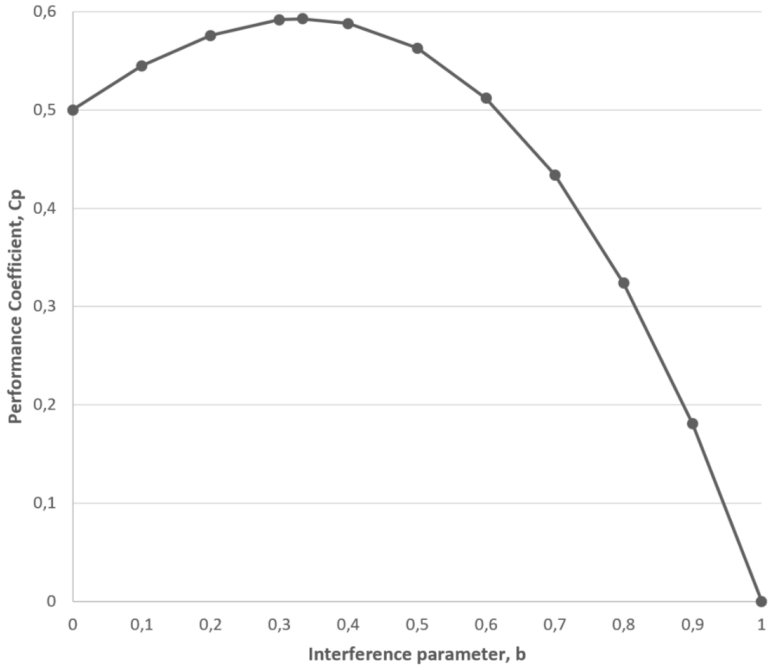


Figure 4.1.2: The performance coefficient $C_P$ as a function of the interference factor $b$

When $b = 1$, $U_1 = U_2$ and the wind stream is undisturbed, leading to a performance coefficient of zero. When $b = 0$, $U_2 = 0$, the turbine stops all the air flow and the performance coefficient is equal to 0.5. It can be noticed from the graph that the performance coefficient reaches a maximum around $b = \frac{1}{3}$. A condition for maximum performance can be obtained by differentiation of equation (4.1.8) with respect to the interference factor $b$. Applying the chain rule of differentiation (shown below) and setting the derivative equal to zero yields equation (4.1.9):

$$\frac{d}{dx}(uv) = u\frac{dv}{dx} + v\frac{du}{dx}$$

$$\begin{aligned}\frac{dC_p}{db} =& \frac{1}{2}\frac{d}{db}[(1-b^2)(1+b)] = \frac{1}{2}[(1-b^2) - 2b(1+b)] = \\ =& \frac{1}{2}[(1-b^2) - 2b(1+b)] = \frac{1}{2}(1-b^2-2b-2b^2) = \\ =& \frac{1}{2}(1-3b^2-2b) = \frac{1}{2}(1-3b)(1+b) = 0 \end{aligned} \tag{4.1.9}$$

Equation (4.1.9) has two solutions. The first is the trivial solution:

$$(1+b) = 0$$

$$b = \frac{U_2}{U_1} = -1 \Rightarrow U_2 = -U_1 \tag{4.1.10}$$

Equation (4.1.10) shows that for optimal operation, the downstream velocity $U_2$ should be equal to one third of the upstream velocity $U_1$. Using equation (4.1.8), the maximum or optimal value of the performance coefficient $C_P$ becomes:

$$\begin{aligned} C_{P,out} &= \frac{1}{2}(1-b^2)(1+b) = \frac{1}{2}\left(1 - \left(\frac{1}{3}\right)^2\right) \\ &= \frac{16}{27} = 0.59259 = 59.26\% \end{aligned} \tag{4.1.11}$$

This is referred to as the Betz Criterion or the Betz Limit. It was first formulated in 1919, and applies to all wind turbine designs. It is the theoretical power fraction that can be extracted from an ideal wind stream. Modern wind machines operate at a slightly lower practical non-ideal performance coefficient. It is generally reported to be in the range of:

$$C_{P,prac} \simeq \frac{2}{5} = 40\%$$

Considering the frictional losses, blade surface roughness, and mechanical imperfections, between 35 to 40 percent of the power available in the wind is extractable under practical conditions.

If no change in the wind speed occurs, energy cannot be efficiently extracted from the wind. Realistically, no wind machine can totally bring the air to a total rest, and for a rotating machine, there will always be some air flowing around it. Thus a wind machine can only extract a fraction of the kinetic energy of the wind. The wind speed on the rotors at which energy extraction is maximal has a magnitude lying between the upstream and downstream wind velocities.

The Betz Criterion reminds us of the Carnot cycle efficiency in Thermodynamics suggesting that a heat engine cannot extract all the energy from a given heat reservoir and must reject part of its heat input back to the environment.

### 4.1.1 Rotor optimal Tip Speed Ratio, TSR

Another important concept relating to the power of wind turbines is the optimal tip speed ratio, which is defined as the ratio of the speed of the rotor tip to the free stream wind speed. If a rotor rotates too slowly, it allows too much wind to pass through undisturbed, and thus does not extract as much as energy as it could, within the limits of the Betz Criterion, of course.
On the other hand, if the rotor rotates too quickly, it appears to the wind as a large flat disk, which creates a large amount of drag. The rotor Tip Speed Ratio, TSR depends on the blade airfoil profile used, the number of blades, and the type of wind turbine. In general, three bladed wind turbines operate at a TSR of between 6 and 8, with 7 being the most widely reported value.
In general, a high TSR is desirable, since it results in a high shaft rotational speed that allows for efficient operation of an electrical generator. Disadvantages however of a high TSR include:

- Blade tips operating at 80 m/s of greater are subject to leading edge erosion from dust and sand particles, and would require special leading edge treatments like helicopter blades to mitigate such damage;
- Noise, both audible and inaudible, is generated;
- Vibration, especially in 2 or 1 blade rotors;
- Reduced rotor efficiency due to drag and tip losses;
- Higher speed rotors require much larger braking systems to prevent the rotor from reaching a runaway condition that can cause disintegration of the turbine rotor blades;

The optimal TSR for maximum power extraction is inferred by relating the time taken for the disturbed wind to reestablish itself to the time required for the next blade to move into the location of the preceding blade.
These times are $t_b$ and $t_w$ respectively, and are shown below in equations (4.1.12) and (4.1.13). In equations (4.1.12) and (4.1.13), $N$ is the number of blades, $\omega$ is the rotational frequency of the rotor, $s$ is the length of the disturbed wind stream, and $U$ is the wind speed.

$$t_b = \frac{2\pi}{N\omega} \quad [s] \tag{4.1.12}$$

$$t_w = \frac{s}{U} \quad [s] \tag{4.1.13}$$

If $t_b > t_w$ some wind is unaffected. If $t_w > t_b$, some wind is not allowed to flow through the rotor. The maximum power extraction occurs when the two times are approximately equal. Setting $t_w$ equal to $t_b$ yields equation (4.1.14) below, which is rearranged as:

$$\begin{gathered} t_b \simeq t_w \\ \frac{2\pi}{N\omega} \simeq \frac{s}{U} \Rightarrow \frac{N\omega}{U} \simeq \frac{2\pi}{s} \end{gathered} \tag{4.1.14}$$

Equation (4.1.14) may then be used to define the optimal rotational frequency as shown in equation (4.1.15):

$$\omega_{optimal} \simeq \frac{2\pi U}{Ns} \tag{4.1.15}$$

Consequently, for optimal power extraction, the rotor blade must rotate at a rotational frequency that is related to the speed of the oncoming wind.

$$\lambda_{optimal} \simeq \frac{\omega_{optimal} r}{U} \simeq \frac{2\pi}{N}\left(\frac{r}{s}\right) \tag{4.1.16}$$

### 4.1.2 Effect of the number of rotor blades on the Tip Speed Ratio (TSR)

The optimal TSR depends on the number of rotor blades, $N$, of the wind turbine. The smaller the number of rotor blades, the faster the wind turbine must rotate to extract the maximum power from the wind. For an N-bladed rotor, it has empirically been observed that $s$ is approximately equal to 50% of the rotor radius. Thus by setting:

$$\frac{s}{r} \simeq \frac{1}{2}$$

Equation (4.1.16) is modified into equation (4.1.17)

$$\lambda_{optimal} \simeq \frac{2\pi}{N}\left(\frac{r}{s}\right) \simeq \frac{4\pi}{N} \tag{4.1.17}$$

For N = 2, the optimal TSR is calculated to be 6.28, while it is 4.19 for three-bladed rotor, and it reduces to 3.14 for a four-bladed rotor. With proper airfoil design, the optimal TSR values may be approximately 25% – 30% above these values. These highly-efficient rotor blade airfoils increase the rotational speed of the blade, and thus generate more power. Using this assumption, the optimal TSR for a three-bladed rotor would be in the range of 5.24 – 5.45.
Poorly designed rotor blades that yield too low of a TSR would cause the wind turbine to exhibit a tendency to slow and stall. On the other hand, if the TSR is too high, the turbine will rotate very rapidly, and will experience larger stresses, which may lead to catastrophic failure in highly-turbulent wind conditions.

## 4.2 Introduction to Mathematical modelling

The basic equations in some wind mathematical models can be applied for fluid, like water, because these models are based on the Bernoulli equation [25].
General aerodynamic concepts are then introduced. The details of momentum theory and blade-element theory are developed. The combination of two theories, called strip theory or blade-element momentum theory (BEM) is then studied to outline

the governing equations for the aerodynamic design and power prediction of a turbine rotor.

The theory of the Vortex, Panel and Cascade are also defined later in this section.

## 4.3 Actuator disk model (ADM)

A simple model, generally attributed to Betz (1926) can be used to determine the power from an ideal turbine rotor, the thrust of the wind on the ideal rotor and the effect of the rotor operation on the local wind field. The simplest aerodynamic model is known as "actuator disk model" in which the turbine is represented by a uniform actuator disk which creates a discontinuity of pressure in the stream tube of air flowing through it. Actuator disk theory is based on a linear momentum theory developed over 100 years ago to predict the performance of ship propeller [27].
This analysis uses the following assumptions:

- Homogenous, incompressible, steady state fluid flow;
- No frictional drag;
- An infinite number of blades;
- Uniform thrust over the disk or rotor area;
- The static pressure far upstream and far downstream of the rotor is equal to the undisturbed ambient static pressure;

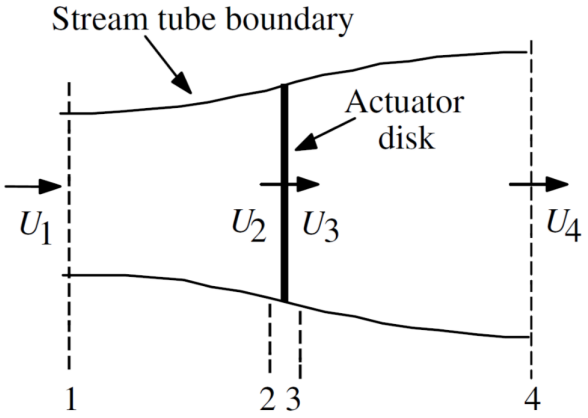


Figure 4.3.1: Actuator disk model of a wind turbine; $U$ , mean air velocity; 1, 2, 3 and 4 indicate locations

Applying the conservation of linear momentum to the control volume enclosing the whole system, one can find the net force on the contents of the control volume. That force is equal and opposite to the thrust, $T$, which is the force of the wind on

the wind turbine. From the conservation of linear momentum for a one-dimensional, incompressible, time-invariant flow, the thrust is equal and opposite to the change in momentum of air stream:

$$T = U_1(\rho AU)_1 - U_4(\rho AU)_4$$

where $\rho$ is the air density, $A$ is the cross sectional area, $U$ is the air velocity and the subscripts indicate values at numbered cross sections in figure 4.3.1. For steady state flow, $(\rho AU)_1 = (\rho AU)_4 = \dot{m}$ , where $\dot{m}$ is the mass flow rate.
Therefore:

$$T = \dot{m}(U_1 - U_4) \tag{4.3.1}$$

The thrust is positive so the velocity behind the rotor, $U_4$, is less than the free stream velocity, $U_1$. No work is done on either side of the turbine rotor. Thus the Bernoulli function can be used in the two control volumes on either side of the actuator disk. In the stream tube upstream of the disk:

$$p_1 + \frac{1}{2}\rho U_1^2 = p_2 + \frac{1}{2}\rho U_2^2 \tag{4.3.2}$$

In the stream tube downstream of the disk:

$$p_3 + \frac{1}{2}\rho U_3^2 = p_4 + \frac{1}{2}\rho U_4^2 \tag{4.3.3}$$

where it is assumed that the far upstream and far downstream pressures are equal ($p_1 = p_4$) and that the velocity across the disk remains the same ($U_2 = U_3$). The thrust can also be expressed as the net sum of the forces on each side of the actuator disk:

$$T = A_2(p_2 - p_3) \tag{4.3.4}$$

If one solves for $(p_2 - p_3)$ using equations 4.3.2 and 4.3.3 and substitutes that into equation 4.3.4, one obtains:

$$T = \frac{1}{2}\rho A_2 \left(U_1^2 - U_4^2\right) \tag{4.3.5}$$

Equating the thrust values from equations 4.3.1 and 4.3.5 and recognizing that the mass flow rate is $A_2U_2$ , one obtains:

$$U_2 = \frac{U + U}{2}$$

Thus, the wind velocity at the rotor plane, using this simple model, is the average of the upstream and downstream wind speeds. If one defines the axial induction factor, $a$ , as the fractional decrease in wind velocity between the free stream and the rotor plane, then:

$$a = \frac{U_1 - U_2}{U_1}$$

$$U_2 = U_1(1 - a) \tag{4.3.6}$$

$$U_4 = U_1(1 - 2a) \tag{4.3.7}$$

The quantity, $U_1 a$ , is often referred to as the induced velocity at the rotor, in which case velocity of the wind at the rotor is a combination of the free stream velocity and the induced wind velocity. As the axial induction factor increases from 0, the wind speed behind the rotor slows more and more. If $a = 1/2$, the wind has slowed to zero velocity behind the rotor and the simple theory is no longer applicable.
The power out, $P$ , is equal to the thrust times the velocity at the disk:

$$P = \frac{1}{2}\rho A_2 \left(U_1^2 - U_4^2\right) U_2 = \frac{1}{2}\rho A_2 U_2 (U_1 + U_4)(U_1 - U_4)$$

Substituting for $U_2$ and $U_4$ from Equations 4.3.6 and 4.3.7 gives

$$P = \frac{1}{2}\rho A U^3 4a(1-a)^2 \tag{4.3.8}$$

where the control volume area at the rotor, $A_2$, is replaced with $A$ , the rotor area, and the free stream velocity $U_1$ is replaced by $U$ . Wind turbine rotor performance is usually characterized by its power coefficient, $C_P$:

$$C_P = \frac{P}{\frac{1}{2}\rho U^3 A} = \frac{Rotor \quad power}{Power \quad in \quad the \quad wind}$$

The non-dimensional power coefficient represents the fraction of the power in the wind that is extracted by the rotor. From equation 4.3.8, the power coefficient is:

$$C_p = 4a(1-a)^2 \tag{4.3.9}$$

The maximum $C_P$ is determined by taking the derivative of the power coefficient (Equation 4.3.9) with respect to $a$ and setting it equal to zero, yielding $a = 1/3$. Thus:

$$C_{P,max} = 16/27 = 0.5926$$

when $a = 1/3$. For this case, the flow through the disk corresponds to a stream tube with an upstream cross-sectional area of $2/3$ the disk area that expands to twice the disk area downstream. This result indicates that, if an ideal rotor were designed and operated such that the wind speed at the rotor were $2/3$ of the free stream wind speed, then it would be operating at the point of maximum power production. Furthermore, given the basic laws of physics, this is the maximum power possible.
From Equations 4.3.5, 4.3.6 and 4.3.7, the axial thrust on the disk is:

$$T = \frac{1}{2}\rho A U_1^2 [4a(1-a)] \tag{4.3.10}$$

Similarly to the power, the thrust on a wind turbine can be characterized by a nondimensional thrust coefficient:

$$C_X = \frac{T}{\frac{1}{2}\rho U^2 A} = \frac{Thrust \quad force}{Dynamic \quad force}$$

From Equation 4.3.10, the thrust coefficient for an ideal wind turbine is equal to $4a(1-a)$. $C_X$ has a maximum of 1.0 when $a = 0.5$ and the downstream velocity is

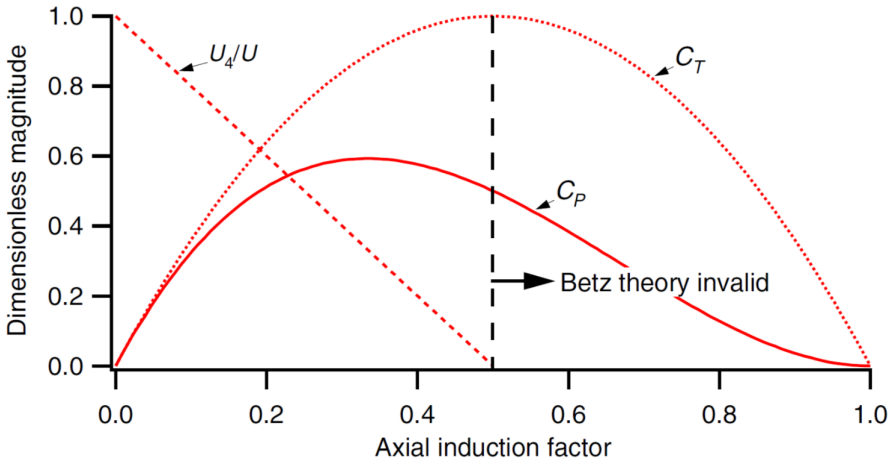


Figure 4.3.2: Operating parameters for a Betz turbine; $U$ ,velocity of undisturbed air; $U_4$ ,air velocity behind the rotor; $C_P$ ,power coefficient; $C_X$ ,thrust coefficient

zero. At maximum power output ( $a = 1/3$), $C_X$ has a value of 8/9. A graph of the power and thrust coefficients for an ideal Betz turbine and the non-dimensionalized downstream wind speed are illustrated in figure 4.3.2.

As mentioned above, this idealized model is not valid for axial induction factors greater than 0.5. In practice (Wilson et al., 1976), as the axial induction factor approaches and exceeds 0.5, complicated flow patterns that are not represented in this simple model result in thrust coefficients that can go as high as 2.0.
As mentioned in the section concerning the Betz limit, the value of $C_P$ is theoretically equal to 16/27 but there are losses in practice that cause a reduction of this value.

## 4.4 General Momentum or Rotor Disk model

The axial momentum theory of the previous section was developed on the assumption that there was no rotational motion in the slipstream and that the turbine blades could be replaced by an actuator disk which produce a sudden decrease of pressure in the fluid without any change in velocity. More generally, the slipstream will have a rotational motion by the reaction of the torque of the blade and this rotational motion implies a further loss of energy [28].
To extend the theory to include the effects of this rotational motion, it is necessary to modify the qualities of the actuator disk by assuming that it can also provide a rotational component to the fluid velocity while the axial and radial components remain unchanged.
Using a stremtube analysis, equation can be written that express the relation between the wake velocities (both axial and rotational) and the corresponding wind velocities at the rotor disk. In figure 4.4.1 an anular streamtube model of this flow illustrating the rotation of the wake is shown for making the visualization clear figure 4.4.2 illustrates the geometry of this stremtube model.

Referring to the figure 4.4.2, let $r$ be the radial distance of any annular element

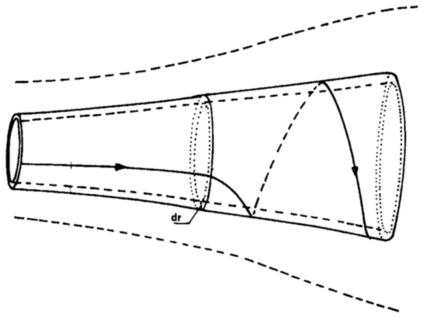

Figure 4.4.1: Streamtube model including wake rotation

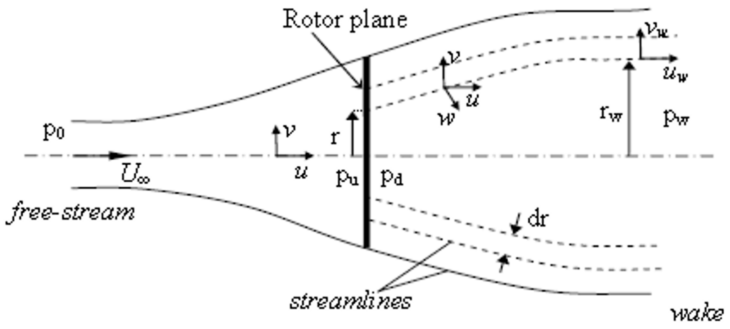


Figure 4.4.2: Geometry of streamtube model

of the rotor plane, let $u$ and $v$ respectively the inflow ( the flow immediately in front of the rotor plane) axial and radial components of the fluid velocity. Let $p_u$ be the inflow pressure and let $p'$ be the decrease of the outflow ( the flow immediately behind the rotor plane) pressure associated with an angular velocity $w$. In the final wake let $p_w$ be the pressure, $u_w$ be the axial velocity and $w_w$ be the angular velocity at a radial distance $r_w$ from the axis of the slipstream.
By applying both conditions of flow continuity for the annular element and the constancy of angular momentum of the fluid, one obtains:

$$u_w r_w dr_w = urdr \tag{4.4.1}$$

$$w_w r_w^2 = wr^2 \tag{4.4.2}$$

Since the element of torque of the radial blade element is equal to the angular momentum extracted in unit time to the corresponding annular element of the slipstream

$$dM = \rho u w r^2 dA \tag{4.4.3}$$

where $dA = 2\pi r dr$

To make the energy equation, the Bernoulli's equation can be used separately from the free flow conditions at inflow conditions and from the outflow to wake conditions;

$$H_0 = p_0 + \frac{1}{2}\rho U_\infty^2 = p_u + \frac{1}{2}\rho(u^2 + v^2)$$
$$H_1 = p_d + \frac{1}{2}\rho(u^2 + v^2 + w^2 r^2) = p_w + \frac{1}{2}\rho(u_w^2 + w_w^2 + r_w^2)$$

Hence,

$$H_0 - H_1 = p' - \frac{1}{2}\rho(w^2 r^2) \tag{4.4.4}$$

Equation (4.4.4) shows that the decrease of the total pressure head passing through the blade element is below the thrust per unit area $p'$ by a term representing the kinetic energy of the rotational motion provided to the fluid by the torque of the blade.

The expressions for the total pressure head also give

$$\begin{aligned} p_0 - p_w &= \frac{1}{2}\rho(u_w^2 - U_\infty^2) + \frac{1}{2}\rho w_w^2 r_w^2 + H_0 - H_1 = \\ &= \frac{1}{2}\rho(u_w^2 - U_\infty^2) + \frac{1}{2}\rho(w_w^2 r_w^2 - w^2 r^2) + p' \end{aligned} \tag{4.4.5}$$

To find the pressure drop $p'$, Bernoulli equation can be applied between the inflow and outflow relative to the blade which are rotating with an angular velocity $\Omega$. Note that the flow behind the rotor rotates in the opposite direction to the rotor, in reaction to the torque exerted by the flow on the rotor. Hence the angular velocity of the air relative to the blade increase from $\Omega$ to $(\Omega + w)$, while the axial component of the velocity remains constant. The result is:

$$p' = \frac{1}{2}\rho[(\Omega + w)^2 - \Omega^2]r^2 = \rho(\Omega + \frac{w}{2})wr^2 \tag{4.4.6}$$

Finally, combining equation (4.4.6) with the previous equations (4.4.5) and (4.4.2), the drop of pressure in the wake becomes:

$$p_0 - p_w = \frac{1}{2}\rho(u_w^2 - U_\infty^2) + \rho\left(\Omega + \frac{w}{2}\right) w_w^2 r_w^2 \tag{4.4.7}$$

The pressure gradient in the wake balances the centrifugal force on the fluid and is governed by the following equation:

$$\frac{dp_w}{dr_w} = \rho w_w^2 r_w \tag{4.4.8}$$

And then differentiating equation (4.4.7) relative to $r_w$ and equating to equation (4.4.8), a differential equation is obtained connecting the axial and rotational velocities in the wake

$$\frac{1}{2}\frac{d}{dr_w}[U_\infty^2 - u_w^2] = (w_w + \Omega)\frac{d}{dr_w}(w_w r_w^2) \tag{4.4.9}$$

The equation of axial momentum for the blade element, which can be established rigorously by a simple extension of the previous section:

$$T = \int \rho u_w (U_\infty - u_w) dA_w + \int (p_0 - p_w) dA_w$$

And in the differential form:

$$dT = \rho u_w (U_\infty - u_w) dA_w + (p_0 - p_w) dA_w \tag{4.4.10}$$

From the pressure decrease at the rotor plane, $dT$ can alternatively written as:

$$dT = p' dA \tag{4.4.11}$$

By substituting equation (4.4.6) into its place in equation (4.4.11) one obtains:

$$dT = \rho(\Omega + \frac{w}{2}) w r^2 dA \tag{4.4.12}$$

Finally, combining equation (4.4.1),(4.4.5),(4.4.10) and (4.4.12):

$$\frac{1}{2}[U_\infty - u_w]^2 = \left[\frac{\Omega + \frac{w_w}{2}}{u_w} - \frac{\Omega + \frac{w}{2}}{U_\infty}\right] u_w w_w r_w^2 \tag{4.4.13}$$

It should be emphasized that the equation of the axial momentum is based on the assumption that the axial force due to the pressure on the lateral boundary of the streamline is equal to the pressure force, $(p_0 A_0 - p_w A_w)$ over its end. This assumption implies that the mutual interference between various annular elements has been neglected but the actual deviations from the conditions represented by equation (4.4.12) are believed to be extremely small in general. The other assumptions made for deriving the general momentum equations so far are that the rotor was treated as having very large number of very narrow blades (infinite number of blades) resulting in negligible radial component of the velocity of the fluid and the air is incompressible and inviscid, i.e., fluid drag is zero.
Equations (4.4.1), (4.4.2), (4.4.9) and (4.4.13), though rather complex in form, it's enough to determine the relationship between the thrust and the torque of the blade and the flow in the slipstream. If, for example, the angular velocity $w_w$ is known as a function of the radius $r$ in the wake, with equation (4.4.9) the axial velocity $u_w$ may be determined. At the same time, by combining equation (4.4.13) with equations (4.4.1) and (4.4.2), the axial and rotational speeds in the rotor plane can be calculated. The thrust and the torque of the rotor are then obtained from equation (4.4.12) and equation (4.4.3) respectively. Owing to the complexity of these equations, however, it is customary to adopt certain approximations based on the fact that the rotational velocity in the slipstream is generally very small.
An exact solution of the general momentum equations can be obtained when the flow in the slipstream is irrotational except along the axis. The condition implies that the rotational momentum $wr^2$ has the same value for all radial elements. Then by virtue of equation (4.4.11), the axial velocity $u_w$ is constant along a radius because the right-hand side of this equation is zero.

By defining the axial velocities $u$ and $u_w$ as:

$$u = U_\infty(1-a)$$
$$u_w = U_\infty(1-b_{wk})$$

where $b_{wk}$ is the axial induction factor far the wake.
After some algebraic manipulations, it can be obtained from equation (4.4.13)

$$a = \frac{a}{2}\left[1 - \frac{(1-b_{wk})a^2}{4\lambda^2(a-b_{wk})}\right] \tag{4.4.14}$$

Examination of equation (4.4.14) shows that the axial velocity reduction of the rotor disk is always approximately one-half the reduction in the far-wake for the tip-speed ratio above 2, which is the same result reached in the previous section when the wake rotation was neglected.

For the approximate solution, the following assumption is made. The angular $w$ provided to the slipstream is very small compared with the angular velocity $\Omega$ of the blades and it is therefore possible to simplify the general equations by neglecting certain terms involving $w^2$. On this basis of approximation the pressure $p_w$ of the air and the decrease of pressure $p'$ across the rotor disk is equal to the decrease of total pressure head $(H_0 - H_1)$. The relationship connecting the thrust and axial velocity are then the same as in the simple momentum theory, the axial velocity $u$ at the rotor disk is the arithmetic mean of the axial velocity $U_\infty$ and the slipstream velocity $u_w$, and the element of thrust is:

$$dT = 2\rho u(u-U_\infty)dA = 4\pi\rho U_\infty^2 a(1-a)rdr \tag{4.4.15}$$

Alternatively, from equation (4.4.6):

$$dT = p'dA = 2\pi\rho\left(\Omega + \frac{w}{2}\right)wr^3dr$$

And defining angular induction factor, $a' = w/2\Omega$:

$$dT = 4\pi\rho\Omega^2 a'(1+a')r^3dr \tag{4.4.16}$$

Equating the two expressions for the thrust given in equation (4.4.15) and equation (4.4.16), a relationship is obtained between axial induction factor,$a$ and angular induction factor $a'$,

$$\frac{a(1-a)}{a'(1+a')} = \frac{\Omega^2 r^2}{U_\infty^2} = \lambda_r^2 \tag{4.4.17}$$

The element of torque is obtained from equation (4.4.3) as following:

$$dM = \rho u w r^2 dA = 4\pi\rho U_\infty \Omega a'(1+a)r^3dr \tag{4.4.18}$$

The power generated to each radial element $dP$, is given by the following equation:

$$dP = \Omega dM \tag{4.4.19}$$

By substituting $dM$ from equation (4.4.18) into equation (4.4.19) and using the definition of local tip speed ratio $\lambda_r$, the expression for the power generated at each radial element becomes:

$$dP = \frac{1}{2}\rho A U_\infty^3 \left[\frac{8}{\lambda^2} a'(1-a)\lambda_r^3 d\lambda_r\right] \tag{4.4.20}$$

The incremental contribution to the power coefficient from each annular ring is given by:

$$dC_P = \frac{dP}{\frac{1}{2}\rho A U_\infty^3} \tag{4.4.21}$$

By putting equation (4.4.20) into equation (4.4.21) and integrating elemental power coefficient from local tip speed ratio at the hub, $\lambda_h$ to the tip speed ratio, $C_P$ is obtained as:

$$C_P = \frac{8}{\lambda^2}\int_{\lambda_h}^{\lambda} a'(1-a)\lambda_r^3 d\lambda_r \tag{4.4.22}$$

In order to integrate equation (4.4.22), it is needed to relate the variables $a$, $a'$ and $\lambda_r$.By solving equation (4.4.17), $a'$ in term of $a$:

$$a' = -\frac{1}{2} + \frac{1}{2}\sqrt{1 + \frac{4}{\lambda_r^2}a(1-a)} \tag{4.4.23}$$

The aerodynamic conditions for the maximum possible power production occur when the term $a'(1-a)$ in equation (4.4.22) is at its greatest value. Substituting the value for $a'$ from equation (4.4.23) into the term $a'(1-a)$ and setting the derivative with respect to a and equating to zero yields:

$$\lambda_r^2 = \frac{(1-a)(4a-1)^2}{(1-3a)} \tag{4.4.24}$$

And using equation (4.4.24) into equation (4.4.17), it is found that for maximum power in each annular ring:

$$a' = \frac{1-3a}{(4a-1)} \tag{4.4.25}$$

If equation (4.4.24) is differentiated with respect to $a$, a relationship between $d\lambda_r$ and $da$ at those condition is obtained:

$$2\lambda_r d\lambda_r = \left[\frac{6(4a-1)(1-2a)^2}{(1-3a)^2}\right] \tag{4.4.26}$$

Now, substituting the equations (4.4.24), (4.4.25) and (4.4.26) into the equation (4.4.22) gives:

$$C_P, max = \frac{24}{\lambda^2}\int_{a_1}^{a_2}\left[\frac{(1-a)(1-2a)(1-4a)}{(1-3a)}\right]^2 da$$

Where:

- $a_1$ : corresponding axial induction factor for $\lambda_r = \lambda_h$
- $a_2$ : corresponding axial induction factor for $\lambda_r = \lambda$

Also from equation (4.4.20):

$$\lambda^2 = \frac{(1-a_2)(1-4a_2)}{1-3a_2} \tag{4.4.27}$$

Equation (4.4.27) can be solved for the value of $a$ that correspond to operation at tip speed ratios of interest. Note also from equation (4.4.27), $a_2 = 1/3$ is the upper limit of the axial induction factor giving an infinitely large tip speed ratio.

## 4.5 Blade-element theory

The momentum theories, which have been developed in the previous sections, are based on a consideration of the mean axial and rotational velocity in the slipstream to determine the thrust and torque of a blade from the rate of decrease of fluid momentum. The theories determine an upper limit to the power coefficient of any blade, depending on the free-stream wind velocity and on the power extracted, but they restrict the understanding of the effect of rotor geometry (i.e. blade airfoil section, chord and twist). The blade-element theory is an alternative method of analyzing the behavior of blades due to their motion through air [28].

In this theory, the blade is assumed to be made up of a number of sections which are hydro dynamically isolated,that is, there is no hydrodynamic interaction between adjacent sections. The force on the whole blade can be derived by adding the contributions of all the elements along the blade. In figure figure 4.5.1 is shown the schematic annular control volume used for this analysis.

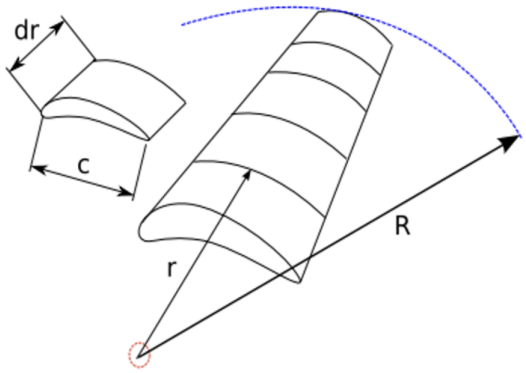


Figure 4.5.1: Schematic of the Blade Element model

The relative wind velocities $U_{rel}$ is the vector sum of the wind velocity at the rotor $U_\infty(1-a)$ (the vector sum of the free-stream wind velocity $U_\infty$, and the induced axial velocity $-aU_\infty$) and the wind velocity due to rotation of the blade. This rotational component is the vector sum of the blade section velocity $\Omega r$, and

the induced angular velocity $a'\Omega r$. Hence the relative wind velocity will be as shown on the velocity diagram figure 4.5.2. The minus sign in term $U_\infty(1-a)$ is due to the retardation of flow while the air approaching the rotor whereas plus sign in term $\Omega r(1+a')$ as shown in figure 4.5.2.

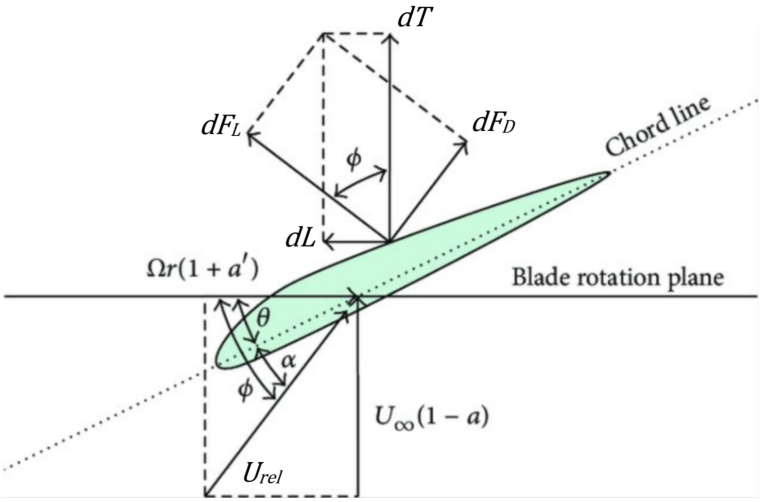


Figure 4.5.2: Forces and velocity triangles for an airfoil section of a rotating wind turbine blade

From the figure 4.5.2 the following relationship can be determined:

$$U_{rel} = \frac{U_\infty(1-a)}{\sin(\varphi)} \tag{4.5.1}$$

$$\tan(\varphi) = \frac{U_\infty(1-a)}{\Omega r(1+a')} = \frac{(1-a)}{(1+a')\lambda_r} \tag{4.5.2}$$

$$dF_D = C_D \frac{1}{2}\rho U_{rel}^2 c dr \tag{4.5.3}$$

$$dF_L = C_L \frac{1}{2}\rho U_{rel}^2 c dr \tag{4.5.4}$$

$$dN = dF_L\cos(\varphi) - dF_D\sin(\varphi) \tag{4.5.5}$$

$$dL = dF_L\sin(\varphi) - dF_D\cos(\varphi) \tag{4.5.6}$$

If the rotor has N number of blades, by rearranging equation (4.5.6) and (4.5.5) with the use of equation (4.5.1), (4.5.3) and (4.5.4), the total normal and tangential forces on the element at a distance $r$ are:

$$dN = N\frac{1}{2}\rho U_{rel}^2(C_L\cos(\varphi) + C_D\sin(\varphi)cdr) \tag{4.5.7}$$

$$dL = N\frac{1}{2}\rho U_{rel}^2(C_L\sin(\varphi) + C_D\cos(\varphi) \tag{4.5.8}$$

The elemental torque due to the tangential forces $dL$, operating at distance $r$ from the center is given by:

$$dM = rdL \tag{4.5.9}$$

Hence, the elemental torque by putting equation (4.5.8) into equation (4.5.9):

$$dM = N\frac{1}{2}\rho U_{rel}^2(C_L\sin(\varphi) + C_D\cos(\varphi))crdr \tag{4.5.10}$$

By defining solidity ratio, $\sigma$ as following:

$$\sigma = \frac{Nc}{2\pi r} \tag{4.5.11}$$

And inserting equation (4.5.1) and (4.5.11) into equation (4.5.7) and (4.5.10), the general form of elemental thrust and torque equations become:

$$dT = \sigma\pi\rho\frac{U_\infty^2(1-a)^2}{\sin(\varphi)}(C_L\cos(\varphi) - C_D\sin(\varphi))rdr \tag{4.5.12}$$

$$dM = \sigma\pi\rho\frac{U_\infty^2(1-a)^2}{\sin(\varphi)}(C_L\sin(\varphi) - C_D\cos(\varphi))r^2dr \tag{4.5.13}$$

Thus, from blade element theory, two equations (4.5.12) and (4.5.13) have been obtained.
They define the normal force (thrust) and the tangential force (torque) on an annular rotor section as a function of the flow angles at the blades and airfoil characteristics.

The following assumptions are at the bases of the blade element theory:

- The behaviour of an element is not affected by the adjacent elements of the same blade;
- The airfoil characteristics for the blade elements;

The independence of blade elements, assumed in the blade element theory and also in all later developments of theory, is analogous to the assumption adopted in the general momentum theory that the thrust on an elementary annulus of a rotor may be expressed as $dT = 2\rho u(u - U_\infty)dA$. In the discussion of general momentum theory it was pointed out that this equation could not be established rigorously. Similarly, in the blade element theory, it is not possible to give a rigorous proof of the independence of the blade elements and the validity of the assumption must be justified by an appeal to suitable experimental results.
If the assumption valid, the thrust on the blade element at radial distance $r$ with the blade angle $\theta$ should be independent of the variation of the blade angle along the remainder of the blade. A check of the assumption can therefore be obtained by taking two propellers of different pitch with blades of the same plan form and section and by rotating the blades of one rotor so that the blade angles of the two rotors have the same value at a chosen radial distance $r$. The thrust distribution along the blades should then show the same element of thrust on the blade elements under examination. By means of a series of experiments has been established the independence of the blade elements over the principal part of the blades.
The second assumption states that two-dimensional airfoil characteristics can be

used for the blade elements. Airfoil two-dimensional characteristics are usually determined from tests of a rectangular airfoil of different aspect ratio. Hence the lift and drag characteristics are dependent on aspect ratio. But in the fully-attached regime, airfoil section characteristics are not generally affected by aspect ratio. However, when two-dimensional data are used, a tip-loss factor must be added as will be described in the next chapter.

## 4.6 Blade element-momentum theory (BEM)

A number of authors have derived methods for predicting the steady state performance of wind turbine rotors. The classical analysis of the wind turbine was originally developed by Betz and Glauert (Glauert, 1935) in the 1930s. Subsequently, the theory was expanded and adapted for solution by digital computers (see Wilson and Lissaman, 1974; Wilson et al., 1976; de Vries, 1979). In all of these methods, momentum theory and blade element theory are combined into a blade element momentum theory (also called "strip theory") that enables calculation of the performance characteristics of an annular section of the rotor. The characteristics of the entire rotor are thus obtained integrating, or summing up, the values for each of the annular sections [27]. This approach is the one used in this section for the mathematical modelling of HAWTs.
As will be described later, the mathematical modeling of VAWTs differs slightly from that of HAWTs, although it derives from the latter.

### 4.6.1 BEM for HAWTs

In the general momentum theory, a particular attention was focused to the motion of the fluid in order to determine the forces on the blades. The defect of the general momentum theory was that it gave no indication of the shape of blade required to produce the reactions considered. The principle of the blade element theory was to consider the forces experienced by the blades of the rotor in their motion through the air and this theory was therefore intimately concerned with the geometrical shape of the blade. In order to overcome the gap between these two theories, the general momentum and the blade element, the blade element momentum theory (BEM), also known as the strip theory, has been developed [28].
The breakthrough of this theory is the effect of finite blade number. The assumptions for BEM theory are obviously the combination of those which were made for general momentum and blade element theory.
The foremost assumption in BEM theory is that individual streamtubes (the intersection of a streamtube and the surface swept by the blades) can be analyzed independently of the rest of the flow as assumed before for the blade element theory.
A second assumption associated with the development of BEM theory is that spanwise flow is negligible, so the airfoil profile data as previously assumed in the blade element theory are acceptable.
A third assumption is that flow conditions do not vary in the circumferential direction, i.e. axisymmetric flow. With this assumption, the streamtube under analysis

is equivalent to a uniform annular ring centered on the axis of revolution.
BEM theory refers to the determination of a wind turbine blade performance by combining the equations of general momentum theory and blade element theory. In this case by equating the elemental thrust force equations from general momentum theory and blade element theory (equations (4.4.15) and (4.5.12) respectively) the following relationship is obtained:

$$\frac{a}{(1-a)} = (\sigma C_L)\frac{\cos(\varphi)}{4\sin^2(\varphi)}\left[1 + (\frac{C_D}{C_L})\tan(\varphi)\right] \tag{4.6.1}$$

And equating the elemental torque derived in both general momentum theory and blade element theory ( equations (4.4.18) and (4.5.13) respectively):

$$\frac{a'}{1-a} = \frac{\sigma C_L}{4\lambda_r \sin(\varphi)}\left[1 - \frac{C_D}{C_L}\cot(\varphi)\right] \tag{4.6.2}$$

Equation (4.6.2) can be rearranged by using equation (4.5.2), which relates $a$, $a'$, $\varphi$ and $\lambda_r$ based on the geometric considerations:

$$\frac{a'}{1-a} = \frac{\sigma C_L}{4\cos(\varphi)}\left[1 - \frac{C_D}{C_L}\cot(\varphi)\right] \tag{4.6.3}$$

In the calculation of induction factors $a$ and $a'$ , accepted practice is to set $C_D$ zero for the purpose of determining induction factors independently from airfoil characteristics. For airfoils with low drag coefficient, this simplification introduces negligible errors. So equation (4.6.1), (4.6.2) and (4.6.3) can be rewritten considering $C_D \approx 0$.

$$\begin{aligned} \frac{a}{(1-a)} &= (\sigma C_L)\frac{\cos(\varphi)}{4\sin^2(\varphi)} \\ \frac{a'}{1-a} &= \frac{(\sigma C_L)}{4\lambda_r \sin(\varphi)} \\ \frac{a'}{(1-a')} &= \frac{(\sigma C_L)}{4\cos(\varphi)} \end{aligned} \tag{4.6.4}$$

By using these three equations the following useful relationship result after some algebraic manipulation:

$$\begin{aligned} C_L &= \frac{4\sin(\varphi)}{\sigma}\frac{(\cos(\varphi) - \lambda_r \sin(\varphi))}{(\sin(\varphi) + \lambda_r \cos(\varphi))} \\ a &= \frac{1}{\left[1 + \left[\frac{4\sin^2(\varphi)}{(\sigma C_L)\cos(\varphi)}\right]\right]} \\ a' &= \frac{1}{\left[1 + \left[\frac{4\cos(\varphi)}{(\sigma C_L)}\right] - 1\right]} \\ \frac{a}{a'} &= \frac{\lambda_r}{\tan(\varphi)} \end{aligned} \tag{4.6.5}$$

TTo determine the power coefficient of a wind turbine, the power contribution from each annular ring is then integrated along the length of the blade, the power coefficient $C_P$ can be obtained. The elemental power from each blade element was defined in equation (4.4.19) as:

$$dP = wdM$$

And the total power from the rotor is:

$$P = \int_{r_h}^{R} dP = \int_{r_h}^{R} wdM$$

Hence the power coefficient $C_P$ becomes:

$$C_P = \frac{P}{\frac{1}{2}\rho A U_\infty^3} = \frac{\int_{r_h}^{R} wdM}{\frac{1}{2}\rho A U_\infty^3}$$

Using the expression for the elemental torque, the power coefficient can be expressed as:

$$C_P = \frac{2}{\lambda^2} \int \sigma C_L \frac{(1-a)^2}{\sin(\varphi)} \left[1 - \left(\frac{C_D}{C_L}\right) \cot(\varphi)\right] \lambda_r^2 d\lambda_r \tag{4.6.6}$$

Finally, by using equation (4.6.4) and (4.6.5) in equation (4.6.6), the general form of power coefficient expression can be obtained as:

$$C_P = \frac{8}{\lambda^2} \int_{\lambda_r}^{\lambda} \lambda_r^3 a'(1-a) \left[1 - \left(\frac{C_D}{C_L}\right) \cot(\varphi)\right] d\lambda_r$$

Note that when $C_D \approx 0$, the equation above for $C_P$ is the same as the one derived from the general momentum theory.

### 4.6.2 BEM for VAWTs

The first momentum model for VAWTs was developed by Templin (1974), where a single streamtube passing through an actuator disk was used to represent the VAWT, similar to Froude's momentum theory applied to HAWTs [1].
Subsequently a multiple streamtube model was developed concurrently by Wilson and Lissaman (1974) and Strickland (1975), where the flow through the actuator disk is split into a number of equal streamtubes that are independent of one another. The momentum equation is thus applied to the blade elements that pass through each steamtube.
The double-multiple streamtube (DMST) model, developed by Paraschivoiu (2002), is the most elaborate variant, and has the best agreement with experimental results for momentum models [1]-[29].

The BEM model can then be classified into [30]:

- Single Streamtube Model;
- Multiple Streamtube Model;

- Double Multiple Streamtube Model;
- Double Actuator Disk Theory;

### 4.6.3 Single Streamtube Model

This model was first developed by Templin for the VAWT. It is based on the actuator disk theories applicable to the propellers and is the basic model of the momentum theory [30].
This model can predict the overall performance of low tip speed ratio for a lightly loaded turbine but it always predicts higher power than the experimental results. It does not predict the wind velocity variations across the rotor [30]. These variations gradually increase with the increase of the blade solidity and tip speed ratio. Single streamtube model does not take into account the difference in the induced velocities between the upstream and downstream streamtube of the rotor. The main drawback of this model is that they become invalid for large tip speed ratios and also for high rotor solidities because the momentum equations in these particular cases are inadequate [31].

### 4.6.4 Multiple Streamtube Model

In the single streamtube model the flow velocity within the streamtube was assumed to be uniform. Wilson and Lissaman assumed a sinusoidal variation in inflow velocity across the width of the turbine to account for non-uniform flow. In order to account for this effect more fully, Strickland extended the model so that the flow through the turbine is divided into multiple independent streamtubes as shown in figure 4.6.1. The momentum balance is carried out separately for each streamtube, allowing an arbitrary variation in inflow [32].
The accuracy is dependent on the number of streamtubes used. For each of these streamtubes the momentum equations have to be calculated, resulting in "n" interference (induction) factors. [30]

### 4.6.5 Double Actuator Disk Theory

The main disadvantage of the previous model is the inability to make a distinction between the upwind and downwind part of the turbine. To make this possible, two actuator disks are placed behind each other, connected at the center of the turbine (figure 4.6.2). In a similar way, as discussed in section 4.4, in this model, the velocities for the two actuator disks are determined by two interference factors, $a$ and $a'$. The induced velocity on the upstream will be the average of the air velocity at far upstream and the air velocity at downstream equilibrium [30].

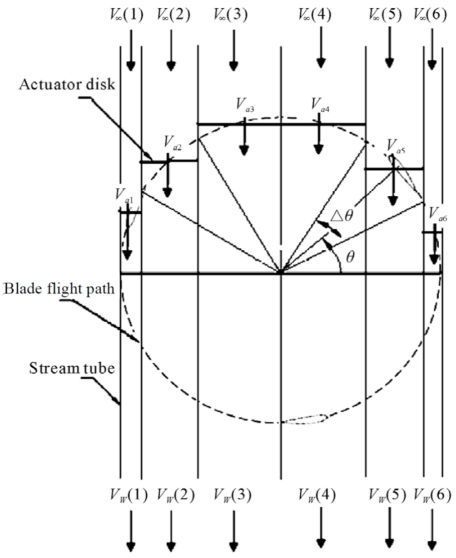


Figure 4.6.1: Principle of multiple stream tube model with 6 stream tubes divided by uniform $\Delta\theta$

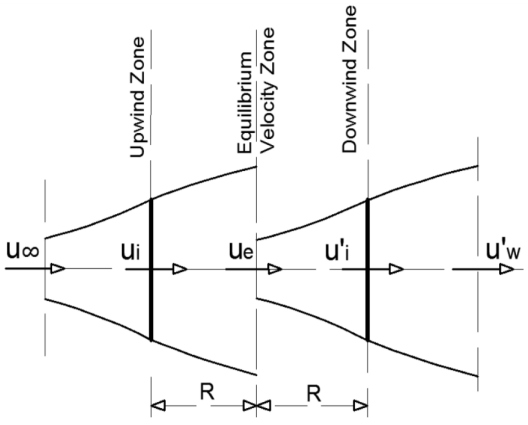


Figure 4.6.2: Schematic of the two actuator disk behind each other

### 4.6.6 Double Multiple Streamtube Model

The double multiple streamtube model described by Loth and McCoy (1983) and Paraschivoiu and Delclaux (1983), combines the multiple streamtubes model with the double actuator disk theory. It allows to model velocity variations in the direction perpendicular to the free stream flow and between the upwind and downwind part of the turbine [30].

The BEM model used for the analysis of VAWTs implies that the fluid current is divided into a finite number of streamtubes both in the longitudinal plane (figure 4.6.3) and in the transversal plane (figure 4.6.4).

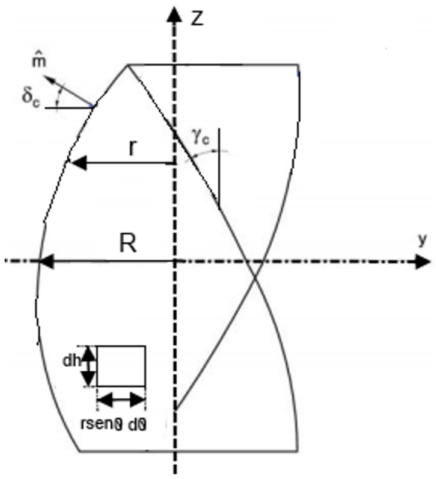


Figure 4.6.3: discretization in flow tubes of the VAWT rotor (longitudinal plane) the taper angle $\delta_c$ and the fordward angle $\gamma_c$ are highlighted

With this approach, the cross-sectional area of each individual streamtube remains constant as it passes through the rotor along the path from upstream to downstream, although it is expected that the wind speed will be reduced as it passes through the machine. Furthermore, the wind path is always considered orthogonal to this section, although in reality it should be slightly deflected due to interference with the movement of the blade. Each streamtube develops in the direction of the absolute wind speed $U_0$ through the machine and crosses two discontinuities of the static pressure field (actuator disks) in which the work exchange is concentrated. The introduction of this model allows to evaluate how the flow field inside the streamtube varies and to analyze the effects of factors that introduce asymmetries such as, for example, the pitch angle $\beta_c$, the curvature of the flow and the dynamic stall. In order to calculate the aerodynamic forces acting on the rotor, it is necessary to know the fluid dynamic conditions in the area around the blade profile. In this regard, where the equatorial cylindrical section of a generic vertical axis machine is reported with a symmetrical blade profile with a setting angle $\beta_c$ placed at a distance $r$ from the axis of rotation whose angular velocity is $w$.

Both $U_\infty$, the undisturbed wind speed upstream of the turbine and $U_{D1}$, the speed component near the blade in the upwind part of the orbital path (figure 4.6.4)

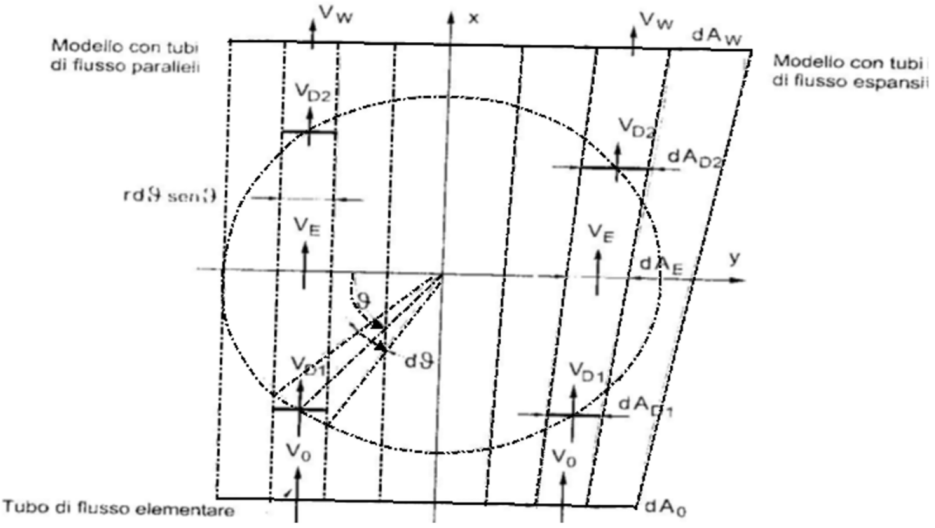


Figure 4.6.4: Discretization in flow tubes for the model with parallel rigid flow tubes (left side) or expanded (right side) in the generic equatorial plane of the VAWT rotor (transverse plane).

and parallel to the flow pipe, are related by the following equation:

$$U_{D1} = \alpha_v^{D1} U_0$$

Where the apex and the subscript $D1$ refer to the variables of the upstream region. The angle of attack $\beta_\infty$, the relative speed $U_{rel}$ and the local Reynolds number are:

$$\varphi_{\infty D1} = \tan^{-1}\left[\frac{U_{D1}\sin(\theta)\cos(\delta_c)}{(U_{D1}\cos(\theta)+wr)\cos(\gamma_c)}\right] = \tan^{-1}\left[\frac{\alpha_v^{D1}\sin(\theta)\cos(\delta_c)}{(\alpha_v^{D1}\cos(\theta)+X)\cos(\gamma_c)}\right]$$

$$U_{rel,D1}^2 = [(U_{D1}\cos(\theta)+U_{rel}r)\cos(\gamma_c)]^2 + (U_{D1}\sin(\theta)\cos(\delta_c))^2$$

$$R_e = \frac{cU_{rel,D1}}{\upsilon}$$

$$\beta_{\infty D1} = \varphi_{\infty D1} + \beta_c$$

Where $\upsilon$ is the kinematic viscosity, $c$ is the chord and $x = TSR = wr/U_\infty$. When the volumetric efficiency $\alpha_v$ is known, the local velocity triangles are determined. It is now possible to obtain the lift coefficients $C_L$ and the resistance coefficient $C_D$ because, once the aerodynamic profile has been chosen, they are uniquely identified by the local Reynolds number and the local angle of attack $\beta_{\infty D1}$.

Now introducing the two coefficients of normal force $C_N^{D1}$ and tangential force $C_T^{D1}$:

$$C_N^{D1} = C_L\cos(\beta_{\infty D1}) + C_D\sin(\beta_{\infty D1})$$
$$C_T^{D1} = C_L\sin(\beta_{\infty D1}) - C_D\cos(\beta_{\infty D1})$$

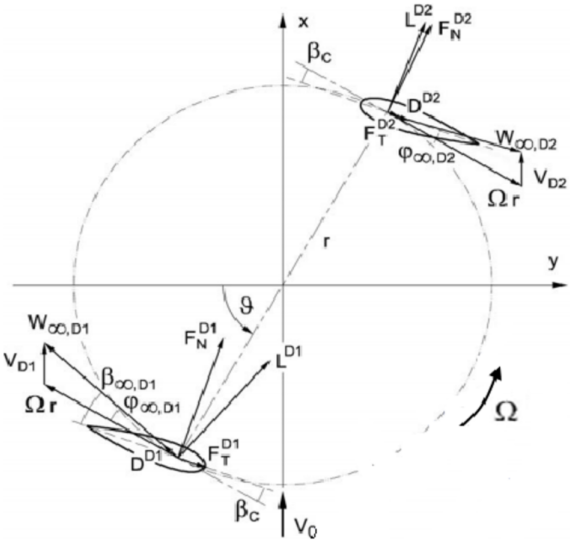


Figure 4.6.5: Velocity triangles and forces acting on the blades for a generic equatorial section of a vertical axis rotor

The normal force $dF_N$ and the tangential force $dF_T$ act on the blade element dh in plan section:

$$dN^{D1} = \frac{1}{2}\rho U_{rel,D1}^2 \frac{cdh}{\cos(\delta_c)\cos(\gamma_c)} C_N^{D1}$$

$$dL^D 1 = \frac{1}{2}\rho U_{rel,D1}^2 \frac{cdh}{\cos(\delta_c)\cos(\gamma_c)} C_T^{D1}$$

where $\rho$ is the water density.

The axial force $dF_X^{D1}$ (the resultant in the wind direction) is the sum of the components $dN^{D1}$ and $dL^{D1}$ in the section plan X-Y:

$$dF_X^{D1} = dN^{D1}\sin(\theta+\beta_c)\cos(\delta_c) + dL^{D1}\cos(\theta+\beta_c)\cos(\gamma_c)$$

Considering a generic rotor with $N$ blades where each blade passes through each streamtube twice (once in the upstream and the other in the downstream) taking a fraction of time equal to $d\theta/2\pi$. The result is an average axial force exchanged in each streamtube of $d\bar{F}_X^{D1}$ obtained from:

$$d\bar{F}_X^{D1} = N\frac{d\theta}{2\pi} dF_X^{D1}$$

At this point it is possible to calculate the average coefficient of thrust $C_X$ that occurs in each streamtube whose value is:

$$C_X^{D1} = \frac{d\bar{F}_X^{D1}}{\frac{1}{2}\rho U_\infty^2 dA_{D1}} = \frac{Nc}{2\pi r}\frac{U_{rel,D1}^2}{U_\infty^2}\left(\frac{C_N^{D1}}{\cos(\gamma_c)}\frac{\sin(\theta+\beta_c)}{|\sin(\theta)|} - \frac{C_T^{D1}}{\cos(\delta_c)}\frac{\cos(\theta+\beta_c)}{|\sin(\theta)|}\right)$$

Where $dA_{D1}$ is the area of the cross section of the streamtube before the rotor:

$$dA_{D1} = dhrd\theta\sin(\theta)$$

Now, referring to figure 4.6.4, it is possible to notice that the average force $d\bar{F}_X^{D1}$ acting on the pole elements in the streamtube is equal to the momentum according to the following expression:

$$d\bar{F}_X^{D1} = 2\rho dA_{D1} U_{D1}(U_\infty - U_{D1})$$

From which we can extract the value of the average thrust coefficient $C_X^{D1}$ equal to:

$$C_X^{D1} = \frac{d\bar{F}_X^D 1}{\frac{1}{2}\rho U_\infty^2 dA_{D1}} = \frac{2\rho dA_{D1} U_{D1}(U_\infty - U_{D1})}{\frac{1}{2}\rho U_\infty^2 dA_{D1}} = 4\alpha_v^{D1}(1-\alpha_v^{D1})$$

At this point, having all the elements and all the values, it is possible to proceed to the calculation of the torque developed by a section of blade of height dh placed at distance $r$ from the axis of rotation.

As for the upstream path:

$$\begin{aligned} dM^{D1}(\theta) =& dF_T^{D1}\cos(\beta_c)\cos(\gamma_c)r - dF_N^{D1}\sin(\beta_c)\cos(\delta_c)r + \\ &+ (dF_N^{D1}\cos(\beta_c)\cos(\delta_c))(b_s\cos(\beta_c)\cos(\gamma_c)) \end{aligned}$$

$$dM^{D1}(\theta) = dL^{D1}\cos(\beta_c)\cos(\gamma_c)r - dN^{D1}\sin(\beta_c)\cos(\delta_c)r + (dN^{D1}\cos(\beta_c)\cos(\delta_c))(b_s\cos(\beta_c)\cos(\gamma_c))$$

Considering $b_s$ the distance between the point of attachment of the blade to the support with the pressure centre and, neglecting the contribution of the tangential force $dL^{D1}$, the elemental torque can be expressed as:

$$\begin{aligned} dM^{D1}(\theta) =& \frac{1}{2}\rho U_{rel,D1}^2 \frac{cdhr}{\cos(\delta_c)\cos(\gamma_c)}[C_T^{D1}\cos(\beta_c)\cos(\gamma_c) + \\ &- C_N^{D1}\sin(\beta_c)\cos(\delta_c) + (C_N^{D1}\cos(\beta_c)\cos(\delta_c))(\frac{b_s}{r}\cos(\beta_c\cos(\gamma_c)))] \end{aligned}$$

And the elemental torque coefficient $C_M$:

$$C_M^{D1} = \frac{dM^{D1}}{\frac{1}{2}\rho U_{\infty,D1}^2 r dA_{D1}}$$

In conclusion, equalling the two different results just found for the thrust coefficient, it is possible to calculate in iterative way (on the value di $\alpha_v^{D1}$) the field of motion that the blades experience during each revolution of the rotor when they are in the upwind zone, and therefore doing so they also find the aerodynamic reactions that develop.
The study moves into the field of motion in the downwind region (apexes and subscripts D2) where taking into account the different values of the number of Reynolds and the different environment that meets the blade is necessary to introduce a second volumetric efficiency $\alpha_v^{D2}$ defined as:

$$\alpha_v^{D2} = \frac{U_{D2}}{U_E}$$

Where $U_{D2}$ is the local flow velocity at the blade in the downwind zone and $U_E$ is the inlet velocity in the streamtube, which is the same value of the outlet velocity of the above streamtube, therefore practically $U_E = U_{D1}$. The procedure is completely analogous to what has been done in the upwind, differentiating this case with the apexes and the subscripts D2 and making valid the same considerations made for the case upwind.

Finally the equation of power can be written as:

$$P = \frac{N}{N_\theta} \sum_{i=1}^{N_L} (\sum_{i=1}^{N_\theta^{D1}} w dM^{D1} + \sum_{i=1}^{N_\theta^{D2}} w dM^{D2})$$

Where: $N_L$ is the number of streamtubes along the z coordinate (figure 4.6.3) that divide the area swept by the rotor.
$N_\theta = \frac{2\pi}{d\theta}$ is the number of streamtubes that cross the equatorial plane of which $N_\theta^{D1} = \frac{\pi}{d\theta}$ are in the upstream position and as many $N_\theta^{D2}$ are in the downstream position (figure 4.6.4).
In an analogous way to the power equation, the expression for the axial thrust on the entire rotor $F_X$ is obtained:

$$F_X = \frac{N_p}{N_\theta} \sum_{i=1}^{N_L} (\sum_{i=1}^{N_\theta^{D1}} dF_X^{D1} + \sum_{i=1}^{N_\theta^{D2}} dF_X^{D2})$$

Finally, after the axial force and power, the power coefficient $C_P$ can be calculated as

$$C_P = \frac{P}{\frac{1}{2}\rho U_\infty^3 A}$$

The BEM theory gave good agreement with experimental results of the overall performance for light-loaded, low-solidity rotors, but it suffers both numerically and in accuracy when the rotor has a high solidity, is heavily loaded and/or is operating at high tip-speed ratios [30].

## 4.7 Cascade models

These models are based on cascade theory used in turbo-machinery design. The blades of the rotor are assumed to be positioned on a plane surface, known as a cascade, with the spacing between adjacent blades equal to the rotor circumference divided by the number of blades, as illustrated in figure 4.7.1. The development and implementation of this model then follows a similar route as the DMST momentum model.

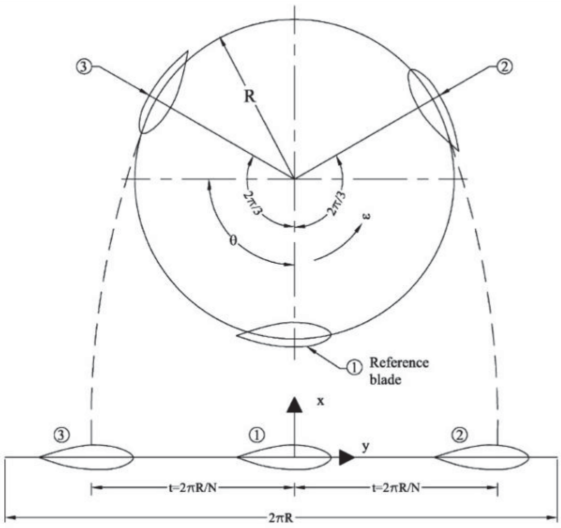


Figure 4.7.1: Cascade model configuration, adapted by Islam

An improvement over the model presented by Hirsch and Mandal was proposed by Mandal and Burton to include flow curvature and dynamic stall. These modifications allowed the model to more accurately represent the flow and loading characteristics experienced by a VAWT in reality,providing for local blade force predictions and generated power in better agreement with experimental data in the study.
Although this model requires more computational time than its momentum model counterpart, it provides more accurate overall values for both low and high solidity rotors, and does not suffer convergence problems at high solidities and high tip speed ratios [1].

## 4.8 Vortex theory

An alternative theory to BEM is vortex theory which provides a method to analyse the rotor performance.
Vortex models assume potential (i.e. inviscid) flow. The velocity field in the vicinity of the rotor is obtained by calculating the influence of vorticity in the wake of the blades. In this model the aerofoil blades are split up into a number of elements, and each element is replaced by a bound (or substitution) vortex filament, also known as a lifting line. With each time step vortices are shed and these influence the induced

velocity of the blade, as illustrated in figure 4.8.1.

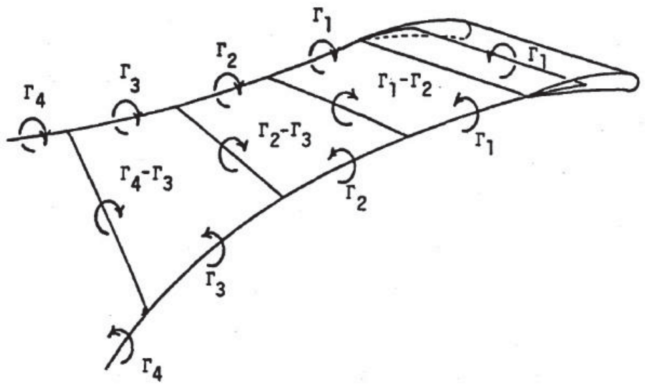


Figure 4.8.1: Vortex element schematic diagram with progression of shed vortices, adapted from Strickland

Two dimensional vortex models for VAWTs were first proposed by Larsen, and further two dimensional models were presented by Fanucci and Walter, Holme and Wilson. These models made several assumptions such as: high tip-speed ratios, lightly loaded rotor, small angles of attack to ignore stall, and high height-to-diameter ratios (for two-dimensional flow). These assumptions limited the vortex models to a specific range of applications and operating conditions. The first three-dimensional model was presented by Strickland. Further improvements by Strickland included dynamic effects, such as dynamic stall, pitching circulation and added mass. When compared with experimental results, it was found that there was good correlation for instantaneous blade forces and near-wake velocities [1].

This theory explains the origin of axial and angular induction factors which have been already introduced in both general momentum theory and blade element theory without giving any physical meaning about their existence.
The vortex theory depends fundamentally on the conception that the lift of an airfoil section is associated with a circulation of the flow around its contour [28].
According to modern airfoil theory the lift $L$ per unit length of an airfoil section in two-dimensional motion is related to the circulation $\Gamma$ around its contour by the following equation:

$$L = \rho U \Gamma$$

By applying this concept of airfoil theory to the problem of the rotor blades, it is evident that there must be circulation of the flow around the blades of the rotor in order to produce the aerodynamic force experienced by the blades.
In general the circulation $\Gamma$ around the blade element will vary along the blade, but to explain the mode of action of the blades it is simpler to assume as a first step that the circulation is constant along the whole blade.
The existence of this circulation can be expressed also by the statement that there is a vortex line of strength $\Gamma$ , bound to the blade and running along it from root

to tip. But a vortex line can not begin or end abruptly; unless it forms a closed curve in the body, it must be continued as a free vortex line in the fluid and in this latter form it follows the general motion of the fluid as a trailing vortex behind the body. Thus the bound vortex must be continued by two free vortices in the fluid, one springing from the root of the blade and the other from its tip.
As shown in figure 4.8.2 below the free vortex springing from the roots of propeller blades will be straight line along the axis of the propeller and its strength will be $N\Gamma$ for a propeller with $N$ blades. The tip vortices, each of strength $\Gamma$ , will be of helical shape and will be tracing out the paths described by the tips of the propeller blades.

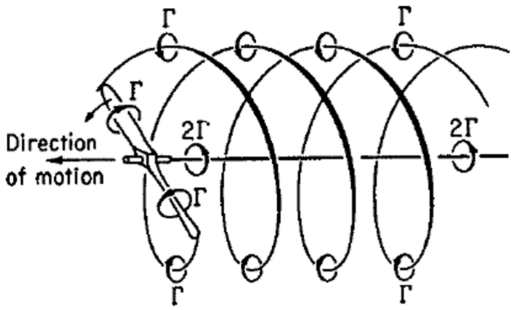


Figure 4.8.2: Tip and root vortices

Up to this point the vortex system of a rotor or propeller has been based for simplicity on the assumption that the circulation along the blade is constant.
More generally, however, the strength of the circulation will vary along the blade and indeed the condition of constant circulation along the whole blade is physically impossible. Because the pressure difference between the top and bottom surface of the blade causes flow and pressure equalization near the blade tips.
For an illustration the actual variation of the circulation along the blade is given in figure 4.8.3 below. Due to the variation of the circulation along the blade, trailing vortices will arise, not only at the root and tip of the blade, but from every point of its trailing edge, forming a continual screwlike vortex sheet.

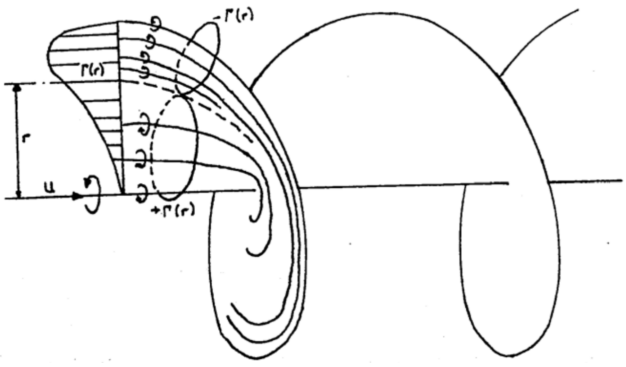


Figure 4.8.3: Variation of bound circulation along blade length

If $\delta\Gamma$ is the increase of circulation between the points $r$ and $(r+\delta r)$ of the blade,

then the strength of the helical vortex springing from this element will be $-\delta\Gamma$. The vortex line springing from one blade form a vortex sheet in the form of a screw surface and there will be one such surface for each blade. The slipstream of the rotor consists of these vortex sheets and of the fluid contained between them.
The disturbance of the flow caused by a rotor can be represented as the induced velocity of the completed vortex system, comprising the bound vortices of the propeller blades and the free vortex sheets of the slipstream and the motion of the fluid relative to the propeller is the resultant of the axial velocity and its induced velocity. Owing to the difficulty of calculating the induced velocity of the system of helical vortex sheets which constitute the slipstream of a rotor, the induced velocity is usually calculated on the assumption that the propeller has a very large number of blades. This assumption implies that the vorticity of the slipstream is distributed throughout the whole of the fluid instead of being concentrated on a few vortex sheets and the vorticity can then be assumed to be grouped in the following manner.
Considering first the condition of constant circulation along the blades, the boundary of the slipstream is a cylindrical vortex sheet as shown in figure 4.8.4.

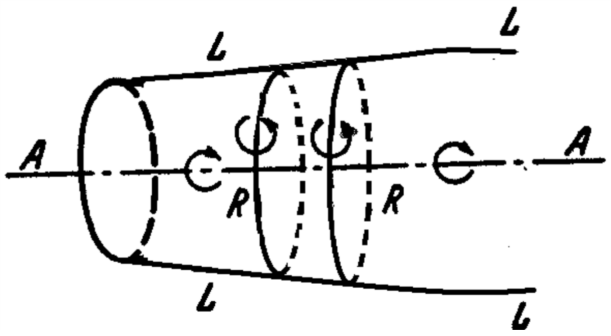


Figure 4.8.4: Helical vortices replaced by axial and circumferential vortex lines

In place of the helical vortex lines covering the surface, the vorticity of the sheet may be considered a close succession of vortex rings RR whose vorticity represents the decreased axial velocity of the slipstream and a surface of vortex lines LL whose vorticity represents the rotation of the slipstream. The vortex system is completed by the axial vortex AA. More generally, with circulation varying along the blades of the propeller, the whole slipstream must be considered as full of vortex systems of this simpler type.
The induced velocity of the vortex system in the ultimate wake far behind the rotor plane will be an axial velocity $(U_\infty - u_w)$ and an angular velocity $w_w$ , which will be function of the radial coordinate $r_w$. In this wake the induced velocity of the bound vortices of the blades is negligibly small. At the disk also the bound vortices can not give any component to the axial velocity owing to the symmetrical distribution of this vorticity relative to any arbitrary point of the disk and hence the axial induced velocity $(U - U_\infty)$ will be due wholly to the trailing vortex system. Also if the expansion of the slipstream can be ignored in calculating these induced velocities, it can easily be seen that the axial induced velocity at the rotor disk is half that in the ultimate wake; for the vortex system is then simply a long cylinder extending

indefinitely in one direction from the rotor disk and the induced axial velocity at a point of the wake, where the cylinder extends indefinitely in both directions, must clearly be double that at the corresponding point of the rotor disk.

Thus

$$(U_\infty - u) = \frac{1}{2}(U_\infty - u_w)$$

Or

$$u = \frac{1}{2}(U_\infty + u_w)$$

Which is the well known equation of the momentum theory described previously from which the axial induction factor has been defined.
The induced angular velocity $w'$ immediately behind the rotor disk can be related to the corresponding angular velocity $w_w$ in the wake by considering the constancy of circulation of the fluid. The ring of fluid of radius $r$ immediately behind the rotor disk has the circulation $2\pi w r^2$ and by the laws of hydrodynamics this circulation must remain constant as the ring of fluid passes down stream. In the wake the radius of the ring has expanded to $r_w$ and there must therefore be a decrease of the angular velocity governed by the equation (4.4.2) as described in section 4.4.

Immediately in front of the rotor disk there can be no such circulation, since the fluid approaching the rotor is in irrotational motion. Also the bound vorticity of the rotor blades must cause equal and opposite induced angular velocities $\pm w'$ immediately before and behind the rotor disk and hence the induced angular velocity of the trailing vortex system must have the value $w'$ at the rotor disk in order to cancel the effect of the bound vortices in front of the disk.
It follows that the total induced angular velocity immediately behind the rotor disk is $2w'$ and this is the angular velocity previously denoted by $w$. Hence the induced angular velocity of the trailing vortices at the propeller disk is $1/2w$ and the angular induction factor in section 4.4 has been defined by taking this value as a basis.
Vortex theory shows also the independence of blade elements which has been assumed in blade element theory in previously section 4.5 and tried to explained physically. Here it will be explained with the help of vortex theory as well by taking the consideration of the system of trailing vortices which leads to the conclusion that induced flow experienced by the blade elements at radial distance $r$ from the axis depends solely on the forces experienced by these elements and is not influenced by the blade elements at greater or less radial distance. Consider the action of the blade elements $dr$ at radial distance $r$ when the remainder of each rotor blade is inoperative.
The trailing vortices which spring from the ends of the element lie on the surfaces of two circular cylinders of radius $r$ and $r + dr$ espectively and the vorticity may be resolved into two components as described before; one having its axis parallel to the rotor axis and the other being circumferential and similar to a succession of vortex rings. The first component of the vorticity acts as the roller bearings between the rotating shell of air bounded by the cylindrical surfaces and the general mass of air. Now the general mass of air can not acquire any circulation about the axis and hence the rotation due to the torque of the blade elements is confined to the region

between the two cylindrical surfaces. Hence also the rotational interference due to the vortex system is experienced by those blade elements which gave rise to the vorticity. A similar argument can be applied to the second component of the vorticity and thus the independence of the blade elements at different radial distances from the axis of the rotor is established.

It may be summarized the results of the vortex theory as follows:

- The induced flow at any radius r depends inly on the thrust and torque grading at this radius. In other words, the blade elements at differing radius are hydrodynamically independent. This proves the validity of the assumption about this result mentioned in the blade element theory in section 4.5;

- The induced axial velocity at a blade element is just half the axial velocity in the distant part of the slipstream which comes from the element at that radius. This is in agreement with the findings of the actuator disk theory in section 4.3;

- The induced circumferential or rotational velocity of inflow at a blade element is just the half the rotational velocity in the distant part of the slipstream which comes from the elements at that radius which is what done while defining angular induction factor in the general momentum theory in section 4.4.

Before closing this section a few words about the advantages and disadvantages of the vortex theory over the BEM theory are the following; the BEM theory offers the method of ease of understanding and use as well as minimal computation requirements. However there are a number of situations where it is not reasonable to expect BEM methods over the vortex methods since vortex methods offer the greatest accuracy. Though methods are available for incorporating some complex effects such as yawed flow and unsteady aerodynamics into a BEM analysis, it is much more desirable to seek analytical methods of vortex theory which are fundamentally better suited to complex flows. The greatest obstacle to widespread use of vortex methods is the computation burden.

## 4.9 Panel models

This approach is based upon discretizing the 3D surface of the rotor into a number of panels and assumes a potential flow regime, as shown in figure 4.9.1. On each panel, an ideal flow element (such as a source or doublet) is placed with a prescribed strength and the Laplace equation is subsequently solved for the inviscid and incompressible flow. Panel models can be considered as an extension to vortex models. Vortex models represent an airfoil as a single blade element, using look up tables for lift and drag characteristics to derive the corresponding vortex strength of the element. Panel models represent the airfoil using a series of body conforming panels at which 3D flow properties are calculated and consequently are generally more accurate. This method has been applied extensively in naval hydrodynamics as well as aircraft aerodynamics, as reviewed by Erickson. [1]

The relatively fast computational time in comparison to using higher-fidelity CFD simulations is one of the main benefits of this method. Another major benefit of panel method is that any geometry can be modelled, and does not rely on the interpolation/extrapolation of two-dimensional aerofoil data obtained through experiment or CFD.
Since this type of model is based on potential flow, viscous effects such as stall are not implicitly included. Therefore there is a need to incorporate a boundary layer model such as the lag-entrainment method.

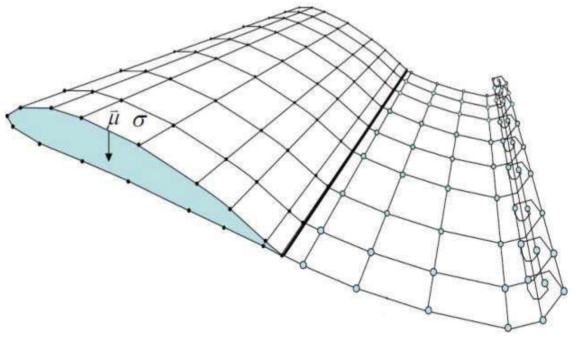


Figure 4.9.1: Panel discretisation of a VAWT blade section and wake roll up

## 4.10 Comparison

Generally for the mathematical modeling of both VAWTs and HAWTs are used the most "elaborate" theories such as the Blade Element Momentum (BEM) model, Cascade model and Vortex model and panel methods. A brief comparison is shown in 4.1.

| | **BEM model** | **Cascade model** | **Vortex model** | **Panel model** |
|---|---|---|---|---|
| *Complexity* | Low-Medium | Low-Medium | Medium-High | High |
| *Ease of implementation* | Easy-Medium | Easy-Medium | Medium | Hard |
| *Computational effort* | Low | Low | Medium-High | Medium-High |
| *Restricted to known airfoils* | Yes | Yes | Yes No | |
| *Incorporate unsteady* | Limited | Limited | Yes | Yes |
| *Rotor-wake/mutiple rotor interactions* | No/No | No/No | Yes/Limited | Yes/Yes |

Table 4.1: Comparison of aerodynamic models [1]

# Chapter 5

# Analysis of Hydrokinetic Turbine Blade Sections

## 5.1 Introduction

The cross-sections of hydrokinetic turbine blades are known as hydrofoils. In this section the observations made will refer to the blades of horizontal axis turbines, as they are generally more complicated.

The turbine blades are used to produce a lift force in order to rotate and extract the optimum power from the system. Each blade of a hydrokinetic turbine is designed from one or more types of hydrofoils. The efficiency and performance of the rotor is mostly dependent on the shape of hydrofoil used. Generally, the thin hydrofoils deliver more efficiency than the thick ones. However, from the structural strength point of view, the thickness of the cross-sections of the hydrofoils near the blade root should be increased. The design thickness of the blade sections depends also on the span length and the hydrodynamic requirements. In large rotor diameter turbines, relatively thicker hydrofoils should be employed in order to accomplish structurally strong blades. Owing to the high density of water, compare to the density of air, the hydrodynamic forces acting on hydrokinetic turbines are greater than the aerodynamic forces on wind turbines. Therefore the blade sections of hydrokinetic turbines should be relatively thicker than that of wind turbines [33].
The main goal of blade and wing design is to increase the lift coefficient and decrease the drag and pitching moment coefficients. Cavitation is the biggest restriction in choosing a hydrofoil for a hydrokinetic turbine rotor. Thin blade sections especially the hydrofoils that are used at the blade tip are more susceptible to cavitation. In order to design a high performance rotor, the cavitation number should be as low as possible while the lift coefficient and the lift to drag (Cl/Cd) ratio should be as high as possible. Numbers of institutions are making special efforts to perform theoretical and experimental studies in order to develop foils. NASA (U.S. National Aeronautics and Space Administration), NREL (U.S. National Renewable Energy Laboratory), Gottingen, Eppler, Wortmann and RISØ are among the most well-known foil developers.

## 5.2 Hydrofoil Terminology

A detailed representation of a hydrofoil and its terminology is given in figure 5.2.1. A hydrofoil principally has an upper and a lower surface. In most of the hydrofoils, the curvature of the upper surface is higher than that of the lower surface. The intersection points of both surfaces at the forward and rearward regions are known as leading and trailing edges, respectively. The flat line connecting the leading and the trailing edges is called chord line; its length is denoted by $c$. The line which is the locus of the mid-points between the upper and the lower surfaces of a hydrofoil is known as camber line. The camber of a hydrofoil is defined as the vertical distance between the chord line and the camber line, the greatest value of that distance is called the maximum camber. The distance between the upper and the lower surfaces measured perpendicular to the chord line is the thickness of the hydrofoil. The angle of attack, which is represented by $\alpha$ is the geometric angle between the relative velocity vector, $U_{rel}$ and the chord line. The span is the perpendicular length of the blade relative to the cross section.
Hydrofoils are characterized by the coordinates of both the upper and lower surfaces. They are generally numbered by using a few parameters such as the maximum thickness, the maximum camber, the position of the maximum thickness, the position of the maximum camber and the nose radius [33].

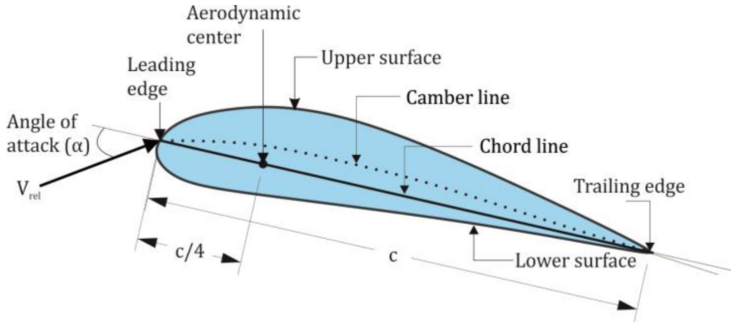


Figure 5.2.1: Hydrofoil nomenclature

## 5.3 Hydrodynamic Forces

A hydrofoil submerged in a stream flow is subjected to various forces due to pressure and velocity changes and the viscosity of the fluid. The forces exerted on the hydrofoil are drag force, $F_D$, lift force, $F_L$ and pitching moment, $M_P$. Drag force is the force that is exerted on the body by the fluid, parallel to the flow direction. The viscous friction and the unequal pressures at the hydrofoil surfaces bring up the drag force. When the fluid moves over the hydrofoil, the velocity of the fluid particles at the upper surface become higher than that of lower surface due to the camber and the angle of attack. High velocity generates a low pressure zone at the upper surface of the hydrofoil while low velocity at the lower surface produces a high pressure zone. Unequal pressure distribution between two surfaces of hydrofoil creates the

lift force. The direction of the lift force is normal to the chord line. Similarly, the pitching moment originates as a function of the integral of the moments of pressure forces over the surfaces of the foil. The application point of these three loads on the hydrofoil is generally accepted to be at c/4 distance from the leading edge on the chord line. The hydrodynamic loads vary with the flow velocity, density of the fluid and the frontal area as well as the size, the shape and the orientation of the body [33].

## 5.4 The Effect of Reynolds Number and Angle of Attack

The Reynolds number ($R_e$) has a significant importance on the behavior of the foils. When $R_e$ decrease, the relative magnitude of the viscous forces become more than the inertial forces. Thus, surface friction and pressure gradients increases. This process results increase in the drag coefficient and reduction in the lift coefficient. In symmetrical foils, the lift coefficient is zero at zero angle of attack ($\alpha$). At low angle of attacks, the lift coefficient is small and increases linearly with increasing the angle of attack. $C_L$ can be increased at low $\alpha$ by using a cambered foil. After $\alpha$ reaches a specific point an abrupt decline is observed in the foil performance and then it stalls. This point is known as maximum lift. The lift behavior of the foil is more or less the same for negative angle of attacks. Generally, the drag coefficient increases with increase in angle of attack [33].

## 5.5 Cavitation Problem

Cavitation on water turbines mainly depends on the pressure coefficient of the blade section. Pressure coefficient ($C_{pr}$) is a non-dimensional parameter which shows the relative pressure on the surfaces of the foil. The typical distribution of pressure on the upper and lower surfaces of a foil is given in figure 5.5.1. The coefficient of pressure is equated as:

$$C_{pr} = \frac{P - P_\infty}{\frac{1}{2}\rho U^2}$$

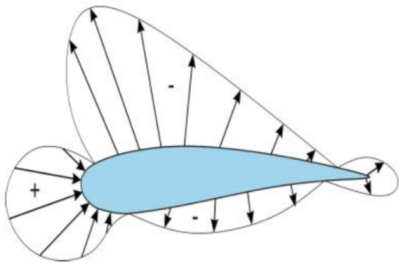


Figure 5.5.1: Positive and negative pressure distributions along hydrofoil surfaces

For simplification, the pressure coefficient can bew ritten as the function of velocity:

$$C_{pr} = 1 - \left(\frac{U}{U_\infty}\right)$$

where $P$ is the local static pressure, $P_\infty$ is the free stream static pressure, $U$ is the fluid particle's velocity.

When the pressure inside the water flow falls below the vapor pressure of the fluid, local boiling occurs and water bubbles develop. Under this condition, the bubbles grow and produce shock waves, noise and some other dynamic effects. This situation results the cavitation on the turbine blades. Cavitation significantly damages the blades, decreases the performance and sometimes causes failure. Especially the parts of turbines, which move with high speed such as blade tips, are subjected to more cavitation. Cavitation is one of the biggest constraints to be considered while modelling a water turbine. It should be taken into account in the designing stage. The equations required to calculate the existence and the amount of cavitation in any section of a turbine blade is given below;

$$\sigma_c = \frac{P_0}{P_v}$$

$$P_0 = P_{atm} + \rho g h + \frac{1}{2}\rho U_\infty^2 a(2-a) - \frac{1}{2}\rho(\Omega r b)^2$$

$$q = \frac{1}{2}\rho U_{rel}^2$$

$$U_{rel} = \sqrt{U_\infty^2(1-a)^2 + (\Omega r)^2(1+b)^2}$$

where, $P_0$ is the local pressure, $P_v$ is the vapor pressure and $q$ is the dynamic pressure. If the absolute value of pressure coefficient becomes greater than the cavitation number, ($|C_{pr}| \geq \sigma_c$), the blade instigates cavitation. Likewise, the blade does not expose to cavitation until cavitation velocity ($U_{cavitate}$) exceeds the relative velocity ($U_{rel}$) [33].

$$U_{cavitate} = \sqrt{\frac{P_{atm} + \rho g h + \frac{1}{2}\rho U_\infty^2 a(2-a) - \frac{1}{2}\rho(\Omega r b)^2 - P_v}{-\frac{1}{2}\rho C_{pr,min}}}$$

where $C_{pr,min}$ is the minimum pressure coefficient.

# Chapter 6

# TABASCO

## 6.1 Introduction

In 2012, the Polytechnic of Turin was commissioned to carry out a study on the design of a river kinetic turbine. Just like today, there were already few applications in this field because the energy extracted from water was mainly used in large hydroelectric power plants. However, these plants have two main disadvantages: they are extremely expensive and their construction includes works that damage the surrounding area. For these reasons it is convenient, in the case of small applications, to harness the kinetic energy of small watercourses to produce electricity.
The first step concerns the evaluation of the state of the art of these projects to understand the rivers potentialities in the regions of north-eastern Italy, such as Piedmont. To have more details, a campaign of study was conducted with different freeware software, using GPS location data, to determine how much energy could be extract from these rivers. The formula is always the same that is used for the water turbine that product mechanical energy from potential energy, but with the differences that the energy source available is kinetic energy.

$$P_{available} = \frac{1}{2}\rho A U^3$$

In table 6.1 is reported a survey about the productivity of water channels in Piedmont. As can be seen, there are around 90 % of water channels in Piedmont that are suitable to install a small power plant, with power between 1 and 5 kW. This is a good result and a good perspective about the usefulness of small kinetic turbine.

## 6.2 Study overview

A lot of knowledge was required for the choice of the hydrofoil profile, so a partnership between the DIMEAS (mechanical and aerospace department of Polytechnic of Turin) and the DELTATRONIC was useful for this study. DELTATRONIC is an industry near Turin focusing into the construction of wind turbine, which design is very similar to water turbine. The aim of this project is to create an autonomous, low-cost and long-life system (hence the name TABASCO, a sort of acronym in

| Power band [kW] | numb. of Section | % |
|---|---|---|
| $P > 1000$ | 2 | 0.15 |
| $250 < P < 500$ | 1 | 0.07 |
| $100 < P < 250$ | 3 | 0.22 |
| $50 < P < 100$ | 9 | 0.67 |
| $30 < P < 50$ | 46 | 3.41 |
| $20 < P < 30$ | 6 | 0.44 |
| $15 < P < 20$ | 7 | 0.52 |
| $10 < P < 15$ | 13 | 0.96 |
| $5 < P < 10$ | 50 | 3.70 |
| $1 < P < 5$ | 1213 | 89.85 |
| **Total** | **1350** | **100** |

Table 6.1: Piedmont's small rivers potentiality

Italian for "low cost turbine"). The main innovation of this project consists in the use of a duct to increase the speed of the fluid at the turbine inlet; this leads to a reduction in the size of the rotor and subsequently in the cost of production.
An control algorithm is used in addition to adjust resistant torque in the generator for each water speed, in order to maximize the energy production. To facilitate this work, a numerical model in MATLAB has been developed to simulate the turbine performance. Once the optimized setup of the real model was obtained, the turbine was tested in a channel in Agliè, a small village in the province of Turin.

## 6.3 Installation site model full-scale

The channel selected for this application has a rectangular section with the following characteristics:

| Width | Height | Water depth | Water speed |
|---|---|---|---|
| 5-6 m | 2.5 m | 0.8 m | 2-2.5 m/s |

## 6.4 Numerical model

The numerical model created in MATLAB environment implements the BEM (blade element momentum) theory. To validate the model, the simulated data were compared with those present in the literature for the Darrieus three-blade turbine of SANDIA with a diameter of 5 m and a solidity ratio of about 0.2 [34].

The comparison was made by analyzing different parameters such as angles of attack and torque and power coefficients, obtaining results that are slightly overestimated, maybe related to the fact that the model does not take into account the

corrections needed to operate at low numbers of Reynolds.
In this case the model uses a database of aerodynamic coefficients for Reynolds values between 80000 and 1000000 and calculates the local Reynolds value using a linear interpolation among the available data. However, if the local value exceeds the maximum or minimum tabulated value, an approximation shall be made by adopting the values at the closest dispositions to those required.

## 6.5 Turbine parameters

The turbine chosen for this application is a Darrieus 'H-type'. In order to create the prototype and the subsequent full scale model, several 4-digit symmetrical NACA profiles were compared. For an easy calculation and realization, a zero blade pitch angle was adopted. In the literature, depending on the type of profile chosen and on the Reynolds numbers relating to the fluid conditions, there can be found the trends of the coefficients of lift and drag as a function of the angle of attack. [23]

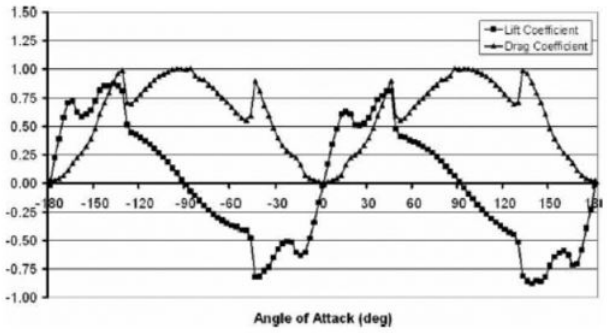


Figure 6.5.1: Aerodynamic coefficients vs angle of attack

### 6.5.1 Prototype

The prototype, based on a model already developed by the company DELTA-TRONIC, has the following characteristics:

- Turbine radius (r) = 0.25 m;
- Blade height (h) = 0.6 m;
- Water depth (H) = 0.8 m;
- Number of blades ($N$) = 3;
- Setting angles of pitch ($\beta_c$), forward ($\gamma_c$) and taper ($\delta_c$) = 0;
- Current speed ($U$) = 0.1 - 0.5 m/s;

- Rotational speed ($w$) = 40 - 90 rpm;

However, the choice to use the model studied by the company has not allowed the simulation of the behavior in the laboratory of the Polytechnic of Turin because of its excessive size.
The prototype was tested by evaluating the performance of different types of symmetrical hydrofoils (NACA 0012, 0015 and 0018) varying the chord length (from 0.08 to 0.2 m).
In this way, the effect of the turbine's solidity factor could be evaluated. Changing the value of the tip speed ratio by varying the current speed for a known rotor speed, one can evaluate the turbine's performance under different operating conditions.

### 6.5.2 Full scale

Once the optimal variables were reached by testing the prototypes, a full-scale model was created based on the size of the channel. The main features are:

- Turbine radius(r) = 0.75 m;
- Blade height (h) = 0.6 m;
- Water depth (H) = 0.8 m;
- Number of blades ($N$) = 3;
- Setting angles of pitch ($\beta_c$), forward ($\gamma_c$) and taper($\delta_c$) = 0;
- Current speed (U) = 2 - 2.5 m/s;
- Rotational speed ($w$) = 40 - 110 rpm

Several tests have been conducted on NACA 0015 for chord values between 0.15 and 0.45 m [23].

## 6.6 Gearbox

The gearbox chosen (Bonfiglioli C35 3 20.2) for the real application allows to increase the speed of the turbine shaft up to about 1500 rpm useful for normal electric generators with 2 polar pairs operating at a mains frequency of 50 Hz. The torque values of the turbine vary between 165 and 300 Nm for the corresponding values of 140 and 90 rpm. The power in the speed range examined varies between 2.41 and 2.82 kW.

| Torque [Nm] | Rotational Speed [rpm] | Power [kW] |
|---|---|---|
| 300 | 90 | 2.82 |
| 260 | 100 | 2.72 |
| 230 | 110 | 2.65 |
| 200 | 120 | 2.51 |
| 165 | 140 | 2.41 |

Table 6.2: Power and torque for different rotational angular speed

## 6.7 Electric generator and inverter

The torque managed by the electric generator (Bonfiglioli BTD5 1870) varies in the range 8 - 14.85 Nm. The inverter is a bidirectional type (Bonfiglioli AGL402 19) and also includes a braking device to limit the load when there is little demand for electricity. The unit is oversized in relation to the actual load to take account of possible current peaks.

## 6.8 Results

### 6.8.1 Prototype

Figure 6.8.1, 6.8.2 and 6.8.3 show that there are small differences between the profiles as the chord evolves. A possible choice would be NACA 0015 or 0018 profiles as they allow to have almost the same $C_P$ for different solidity values. For chord values higher than 0.16, a reversal trend is observed of the trend is observed, which in some cases leads to exceeding the Betz limit, maybe due to the fact that the model studied does not give plausible results at high values of solidity.
Increasing the value of the chord is equivalent to the expansion of the surface of the blade. The flow that invests a blade can therefore be more disturbed by the previous blades, which results in losses during operation. In particular, since it is preferable to have the solidity close to the theoretical values (0.1-0.2), the choice would be in the profile NACA 0015 (with chord = 0.08 m, solidity factor about 0.15) as it permits to have a good power coefficient $C_P$ trends and at the same time, to have a good $C_P$ for small chords. In conclusion, it's shown the trend of $C_P$ with the variation of the rotational speed.

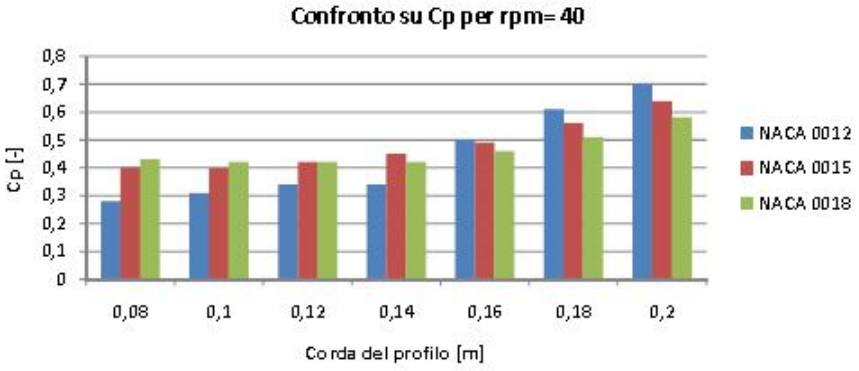


Figure 6.8.1: $C_P$ vs chord, $w = 40$ rpm

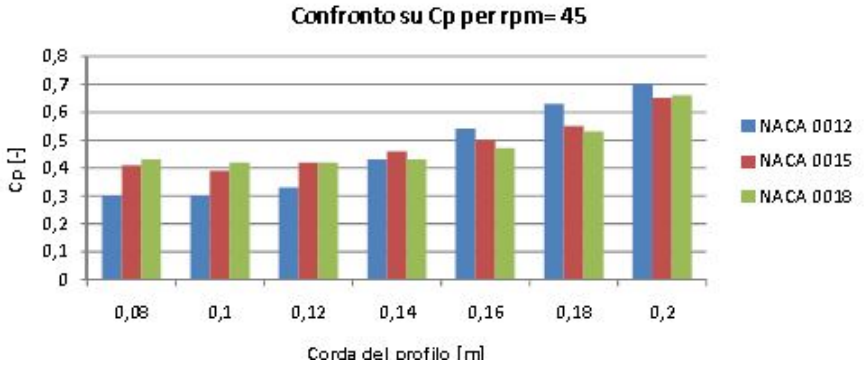


Figure 6.8.2: $C_P$ vs chord, $w = 45$ rpm

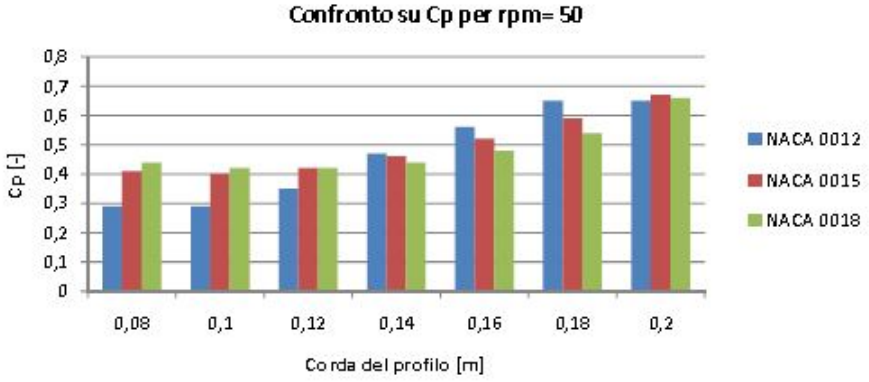


Figure 6.8.3: $C_P$ vs chord, $w = 50$ rpm

- Chord 80 mm;

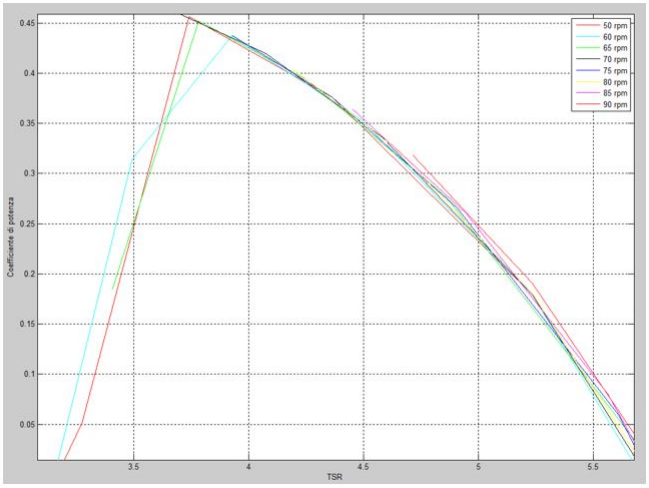


Figure 6.8.4: $C_P$ vs TSR, chord 80 mm

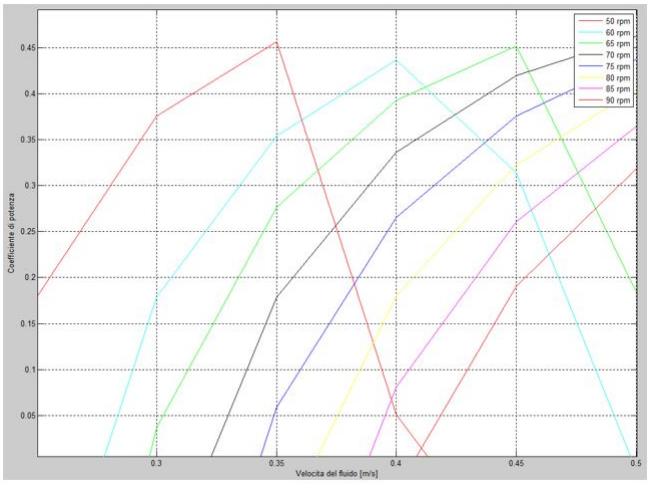


Figure 6.8.5: $C_P$ vs $U$, chord 80 mm

- Chord 140 mm;

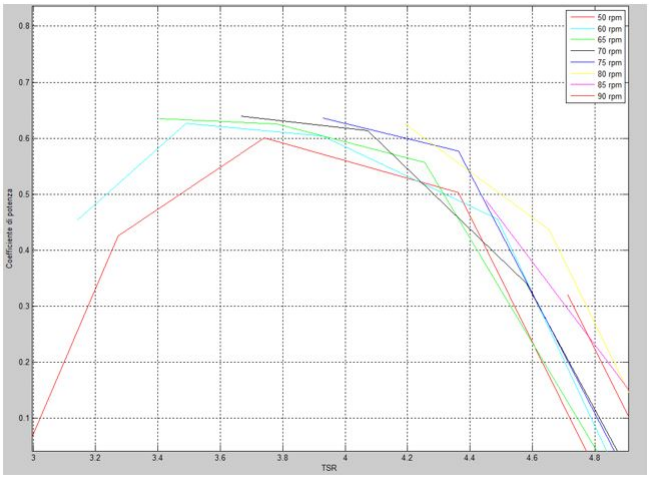


Figure 6.8.6: $C_P$ vs TSR, chord 140 mm

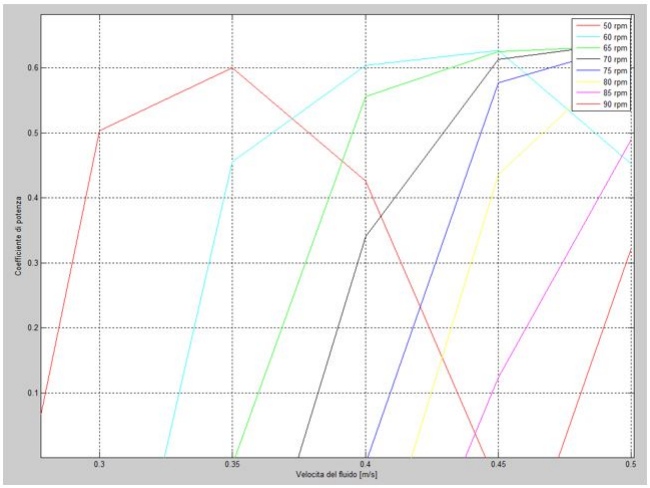


Figure 6.8.7: $C_P$ vs $U$, chord 140 mm

However, the results obtained here in the prototype phase may not be very reliable as they have not been validated by experimental data.

### 6.8.2 Full scale

In order to minimize the solidity value, the profile adopted will be the NACA 0015 with a chord length of 0.15 m. Below are reported some results of the simulated model in real scale.

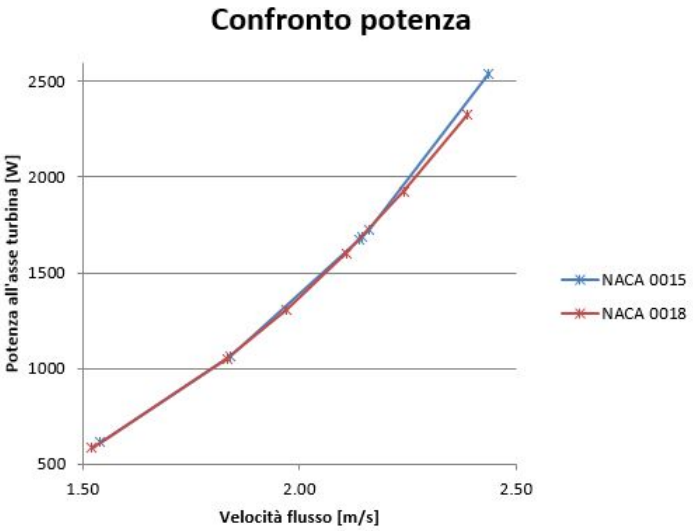


Figure 6.8.8: Power vs current speed for different airfoils

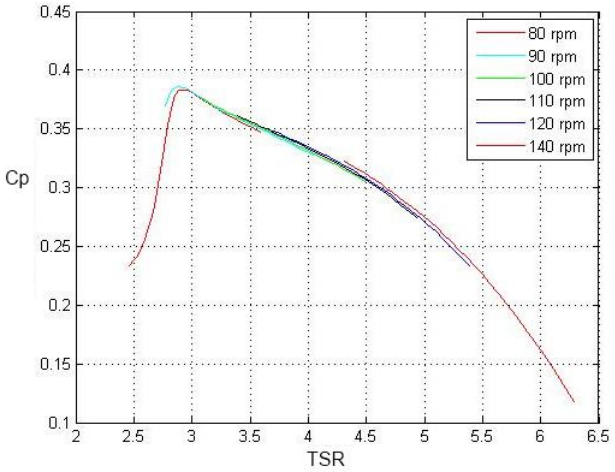


Figure 6.8.9: CP vs TSR, fullscale model

A particular detail of the curve made at 90 rpm is given in figure 6.8.10. At the TSR value of 2.9, corresponding to a $C_P$ value around 0.38, the velocity of the fluid is about 2.4 m/s, a value close to the expected application limit of 2.5 m/s. It is interesting to note that the trend of the $C_P$ for $TSR$ values between about 2.9 and

3.7 is rather linear. As shown in the figure 6.8.11, it is convenient to work with a rotation speed between 80 and 110 rpm in order to obtain the maximum value of the $C_P$ available.

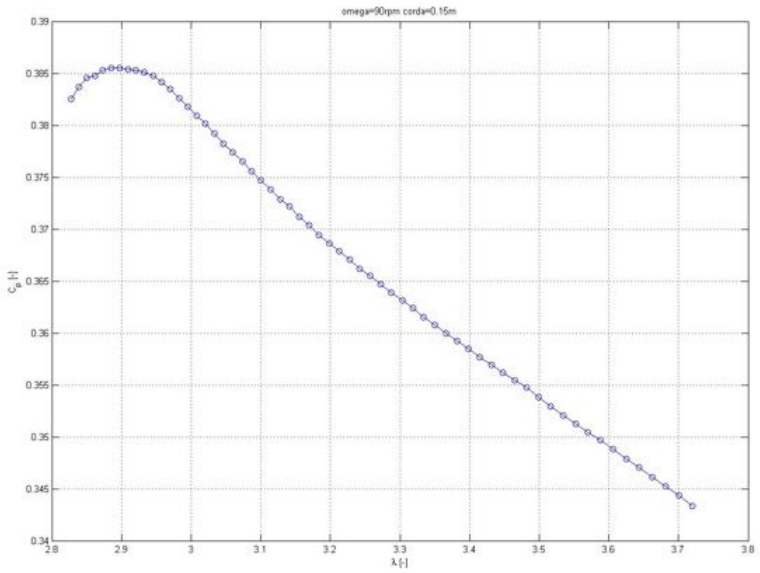


Figure 6.8.10: CP vs TSR, 90 rpm

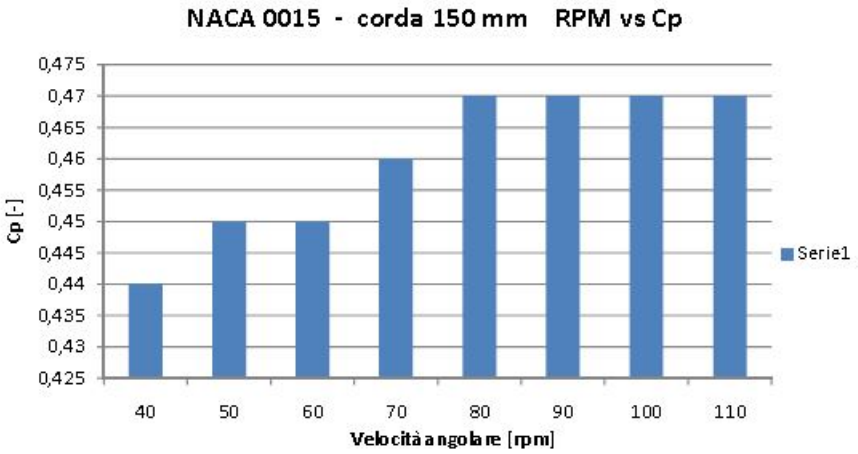


Figure 6.8.11: CP vs TSR, rotor speed variable

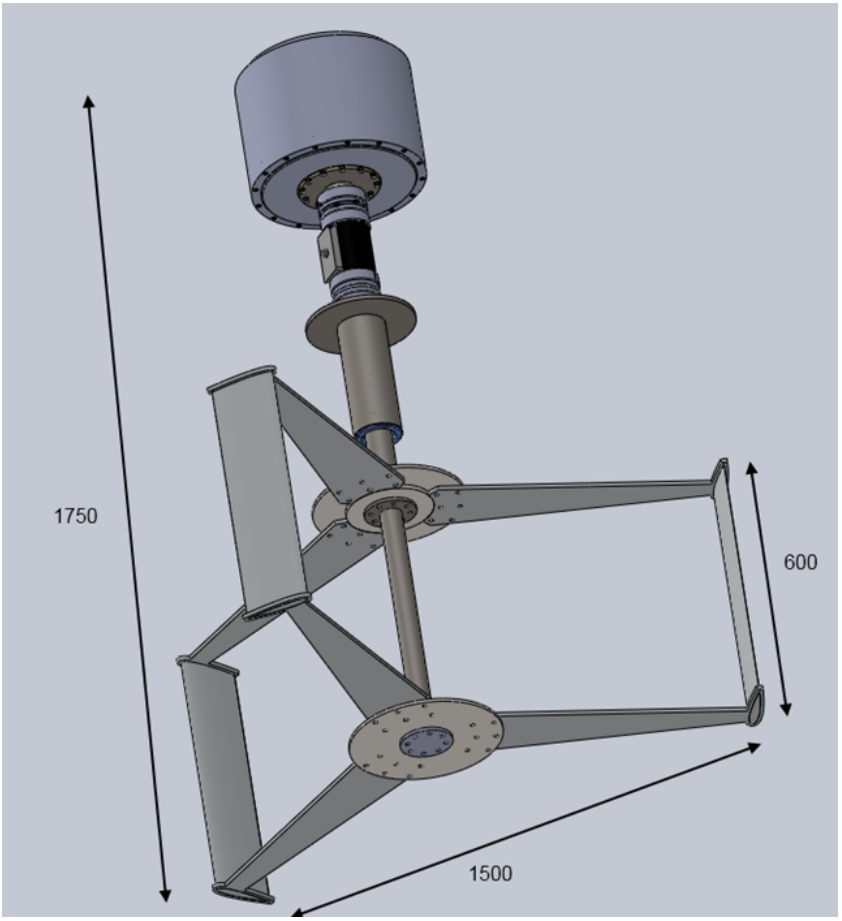


Figure 6.8.12: TABASCO 3D model

# Chapter 7

# Technologies and Companies

In the following chapter, some companies and a short outline of their products will be presented. Table 7.1 gives a summary of the hydrokinetic turbine that are in a commercial and pre-commercial stage.

## 7.1 Thropton Energy Services

Thropton Energy Services specialises in "zero head" hydro power in the form of Water Current Turbines (WCTs). These turbines are quiet and pollution free in use. Minimum site requirements are a water current speed of at least 0.5 m/s and a depth of 1.75 m or more. They provide a complete range of services relevant to WCTs from resource assessment to design and supply local manufacture. The company claims to have twenty years of experience in this field and have worked in UK, Sudan, Somalia, Egypt and Peru [35].
The company is the designer and manufacturer of the Garman turbine, which can be used for both water pumping and electricity generation.
The turbine is axial and can be thought as an underwater wind-mill which floats on a river or canal with the rotor completely submerged. It is moored in freed stream to a post on one bank, making installation simple and cheap and minimising obstruction to river traffic. The propeller fan style turbine, available in diameters of 4, 3.4, 2.8, 2.2 and 1.8 m drives an above-water generator.
The turbines are stand-alone units and have a maximum power output of about 2kW. To keep the capital cost down, Thropton has designed the turbine so that it can be locally manufactured.

## 7.2 Alternative Hydro Solutions Ltd

Alternative Hydro Solutions Ltd. Believes that the Darrieus turbine is the best choice for small and medium river sites. The advantages that Darrieus turbines have over propeller type turbines include:

1. Their ability to have a grater diameter than depth which enables more area to be swept in a shallow stream and therefore more power production per turbine;

2. The vertical shaft provides easy maintenance as the electrical components and bearings are above water;

3. Increased efficiency over propeller turbines not specifically designed as water current turbines.

At lower ratational speeds relative to the water speed the turbine blades reach their stall point and therefore the turbines overspeed is naturally limited, at this poin power production also starts to taper off. The water flow speed that is generally accepted as the minimum for power production is 0.8 m/s [36].
The sizes is diameter are: 1.25, 1.5, 2.5 and 3.0 m in varying shaft depths [36]-[37].

## 7.3 New Energy

New Energy Corporation Inc. have developed a series of turbine/generator sets that produce between 5 kW and 25 kW of power and are supposed to be used in rivers, irrigation canals, industrial outflows, and tidal estuaries. The EnCurrent generator is based on the vertical axis hydro turbine. Since the axis of rotation is vertical, the turbine rotates in the same direction regardless of the direction of the water current, typically capturing between 30% and 40% of the energy in the water stream. The turbine rotates at a very low speed of between 2 and 2.5 times the speed of the water in which it is submerged minimizing risk to aquatic life. Since hydrokinetic turbines extract energy from the naturally occurring kinetic energy in the moving stream of water, there is very little environmental impact on the stream. Floating systems only require an anchor or cable to shore to hold the system in position, and an electrical cable running either overhead or along the channel bottom. Systems can be mounted on a floating structure, or fixed in position by mounting to an existing structure or customized rigid mount, depending on the requirements of a specific application [38].

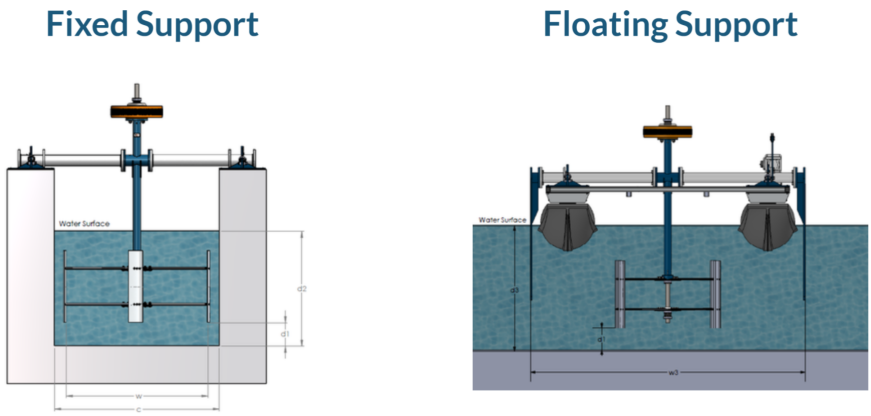


Figure 7.3.1: Anchor Systems of New Energy Turbines

## 7.4 WateRotor Technologies Inc.

Waterotor Energy Technologies Inc., is an Ottawa, Ontario, Canada, based company incorporated in late 2010. The notable aspects are that the waterotor stands alone as a technology that simplifies the extraction of a high level of energy from very slow-moving water. The technology can be scaled from small units to ocean sized rotors. Waterotor claims to be unique in that its highly developed design can extract a very high level of energy (Coefficient of Power) from very slow flowing water. Waterotor has been verified for maximum energy extraction for a water flow speed range from 0.45 m/s to over 9 m/s [39] (size and generator match "selection" per size and flow conditions). The Waterots system is designed to be either a buoyant device secured by anchors, or alternatively, a heavier than water device that can be lowered from bridge, barge, boat, or buoy [40]. The company has stated that Waterotors will be built in a variety of sizes from 5 kW to over 1 MW with output energy supplied at less than 5 cents per kW hour output.
The advantages of waterotor are:

1. Operates in slow-moving water; as lower than 1.5 mph;
2. Strong yet simple structural integrity;
3. High coefficient of power (high-energy output vs size);

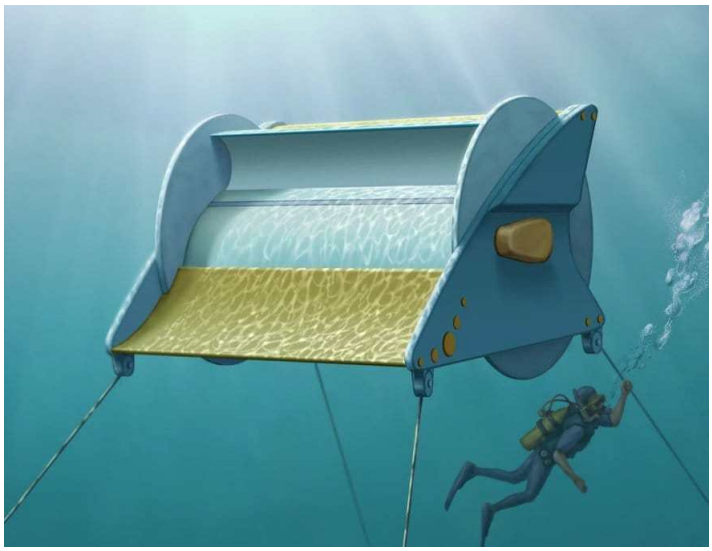

Figure 7.4.1: WateRotor Technology

## 7.5 Hydroquest

After ten years of research in specialist hydroelectric laboratories in Grenoble, France, HydroQuest is a global leader in the operation of hydrokinetic turbines in difficult conditions and guarantees the reliability of its technology to energy producers throughout the world. HydroQuest is also the first hydro turbine builder to connect a river current turbine to the French national grid. HydroQuest designs, develops, manufactures and installed hydrokinetic turbine farms throughout the world. It is one very few producers to be able to meet river turbine equipment needs with its formidable HydroQuest River range of hydrokinetic turbines and in a very near future, marine current turbines with its HydroQuest Ocean range. Hydrokinetic turbines made by world market leader HydroQuest are reliable, modular, compact, quick to install and offer multiple benefits:

- Predictable, regular and economical energy;
- High energy yield;
- Rapid implementation and installation;
- Lifetime spanning more than 25 years;
- Simple operation and maintenance;
- Configuration suited to your site;
- Very low impact on the environment;

Hydroquest manufactures modular turbines and has two main models suited to water depth on sites. The two turbine models have a nominal power output of 40 kW and 80 kW respectively. The minimum depth required for installation is 2.2 m [41].

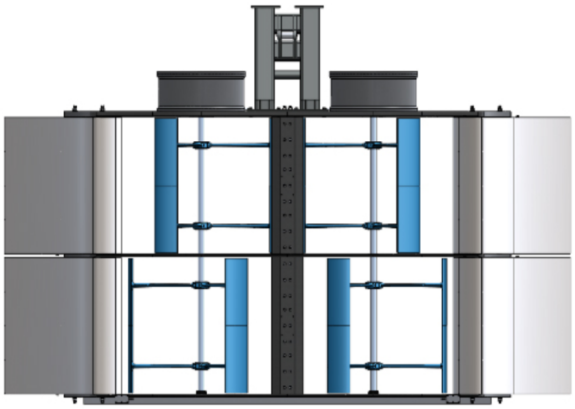

Figure 7.5.1: HydroQuest River 2.8

## 7.6 ORPC RivGen

The RivGen® Power System generates emission-free electricity from river currents and connects directly into existing remote community grids using smart grid technology. It consists of three major subsystems: shore-side power electronics, mooring system, and turbine generator (TGU) device. Many remote communities rely on local power distribution grids connected to diesel generators, which leave a huge carbon footprint and are growing increasingly expensive to fuel and operate. The RivGen® Power System is designed to connect directly into existing diesel-electric grids, operating either in parallel with diesel generators to offset diesel power generation and fuel use, or in "grid-forming" mode, which allows diesel generators to be shut off entirely when RivGen® power output meets or exceeds local demand.
The core component of the RivGen® Power System is ORPC's (Ocean Renewable Power Company) proprietary and well proven turbine generator until. The RivGen® device has a low vertical profile allowing it to be more easily installed in shallower rivers and tidal estuaries than most competing systems. RivGen® Power System components are shop-fabricated, easier to ship to remote sites, simpler to assemble, easier to install and retrieve, and more robust in the underwater than competing technologies. All power system components are located on shore or below the water surface so there is no impact on natural water landscapes, and the system is not affected by floating debris or boat traffic.
Any number of RivGen® devices, each with a rated capacity of 25 kilowatts, can be installed at a site in this manner, depending on community needs and site characteristics.
RivGen® Power System components include the turbine generator unit (TGU) consisting of two turbines connected through a single driveline to an underwater generator in the center; pontoon support structure which supports the TGU; power electronics and control system; underwater power and data cabling; debris protection system(if needed).
Power output of a single RivGen® device varies with water current speed, but in 2 meters per second river current, it will generate 25 kilowatts [42].

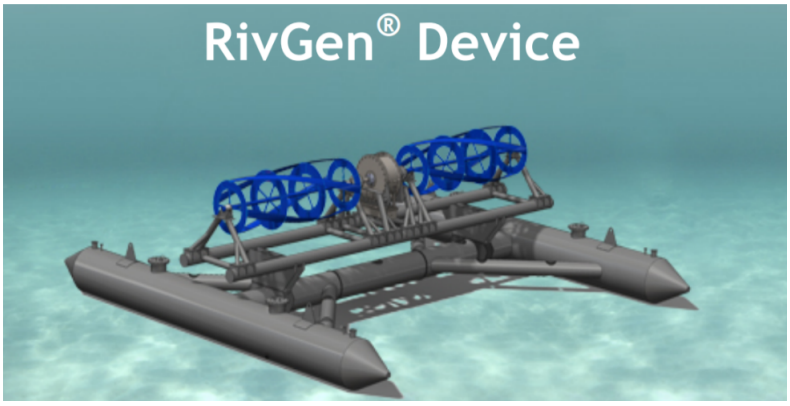


Figure 7.6.1: RivGen device

## 7.7 Smart Hydro Power

These turbines for rivers and canals allow for the introduction of a base load supply, providing a complete renewable energy solution for the best cost-benefit possible. This proprietary technology is standardized and easily scalable. Although qualifying as “green”, these products are positioned as the best alternative for decentralized electrification along rivers.
The Smart Hydro Power turbine was developed to produce a maximum amount of electrical power with the kinetic energy of flowing waters. Because it is powered by kinetic energy instead of potential energy, it is known as a so-called “zero-head” or “in-stream” turbine. As such, no dams and/or head differential are necessary for the operation of this device; the course of a river remains in its natural state and no high investments in infrastructure are required. Because the amount of kinetic energy (velocity) varies from river to river, a greater amount of energy is generated with a higher velocity of water flow. The unique and proprietary river turbines are built up in modules and can be integrated together with photovoltaics into a hybrid system.
Smart Hydro has three different types of turbines (one of which is still at the development stage) depending on operating conditions [43].

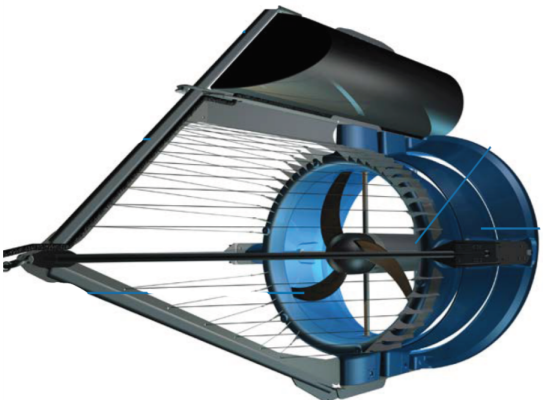

Figure 7.7.1: SMART Monofloat

## 7.8 Hydrovolts

Hydrovolts turbines leverage several revolutionary technologies, including the patent-pending Flipwing rotor design and switchblade chassis, to generate up to 12 kW of clean power. The cross-axial design sits perpendicular to the water flow, maximizing swept area and therefore power potential. Optimized for artificial waterways such as irrigation canals, Hydrovolts turbines are designed to be non-fouling: they rest at the bottom of the waterway below the bulk of surface debris, and all rotors are self-clearing. Depending on site qualifications, products can be installed singly or chained together along the length of a canal to produce more total power [44].

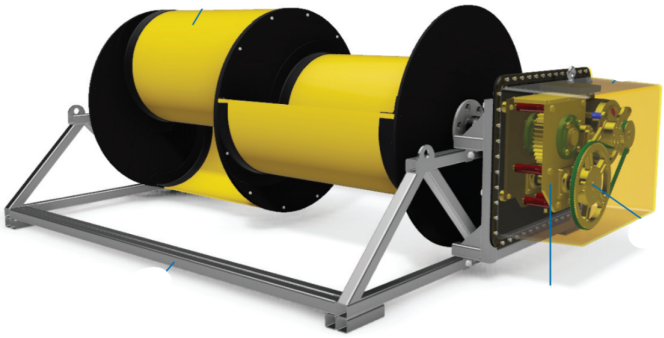

Figure 7.8.1: Hydrovolts C-12 Canal Turbine

Table 7.1: Technologies and Companies

| **Company** | **WCT device name** | **Min/Max Depth** | **Min/Max Velocity** | **Axis of Rotation** | **Unit Power Output** |
|---|---|---|---|---|---|
| Thropton Energy Services | Water Current Turbine | Min 1.75 | Min 0.5 | Horiz | Up to 2kW |
| Alternative Hydro Solution Ltd | Free stream Darrieus Water Turbine | - | Min 0.8 | Vert | Up to 2kW |
| New Energy | EnCurrent Hydro Turbine | Min 1.22 | Min 0.5 | Vert | Over 5kW |
| WateRotor Energy Technologies Inc. | WateRotor | - | Min 0.8 | Horiz | - |
| HydroQuest | Hydroquest River | Min 2.2 | Min 1 | Vert | Up to 80kW |
| ORPC | RivGen Power System | - | Min 1.25 | Horiz | Up to 18 kW |
| Smart Hydro Power | Smart Monofloat | Min 2 | Min 1 | Horiz | Up to 5 kW |
| Hydrovolts | C-12 Canal Turbine | - | Min 1.5 | Horiz | Up to 12kW |

# Chapter 8

# Africa

## 8.1 Introduction

Environmental degradation and global warming are among the major challenges facing many nations of the world. The discourse on issues that concern impacts of human activities on the global climate system has increased tremendously since the beginning of the first decade of the twenty-first century. This debate has taken place in different sectors of the economy both at national and international levels. Global, regional and national institutions, development agencies, non-govermental organisations and public citizens have also engaged in the discussions.
The increase in the intensity of the debates is strongly connected with the Intergovernmental Panel on Climate Change evidence about accelerated global warming. Its reports in 2007 and 2013 gave credence to its earlier release and supported strongly the link between human activities and global warming.
Unfortunately, Africa with its low adaptive capacity has been reported as on the most vulnerable continents to climate change impacts. In addition to this, the interaction of "multiple stresses", occurring at various levels, and high level of risk have been rather challenging on the continent. However, there are many uncertainties regarding the reality of climate change impacts such as predicting the exact rate of warming, and the nature and magnitude of changes in temperature and rainfall. The impacts of global climate change have compelled many African countries to explore the potentials of renewable energy technology (RET) for sustainable development.
Many African energy analysts have come to terms with the fact that RET provides a sustainable energy to most of African countries thanks to the abundance of unexploited renewable energy resources such as biomass, hydropower, solar, geothermal and wind.The renewable energy industrial sector in Africa could still be regarded as an emerging industry with a lot of potential for development. Research and development of new and improved products, has played a significant role in the economic activities of the developed countries.. However, in Africa there is little linkage between "research" and "development" and this problem has increased preference for foreign technology, which has not helped the process of technological learning and capacity building on the continent.
Many countries are now thinking to invest in RET. Although many developed countries such as the USA, Germany, Russia and Japan have long been involved in the

development of renewable energy, African countries should take the lead in this new energy development pathway because of their comparative advantage in terms of the abundance of renewable energy resources.
The World Bank (International financial institution that provides loans to countries of the world for capital projects, which goal is the reduction of poverty) remains committed to continuing its support for well-designed and well-implemented hydropower projects of all sizes for both local development and climate mitigation, while noting that resettlement of communities, flooding of large areas of land and significant changes to river ecosystems must carefully considered and mitigated [7]. Under the Africa Climate Business Plan, launched at the Paris climate conference in late 2015, the Bank highlighted the importance of deploying hydropower (and associated water regulation), along with other renewable power technologies, as a key component in its efforts to accelerate climate-resilient and low-carbon development in sub-Saharan Africa.
The Bank aims to increase the share of hydropower in sub-Saharan Africa's energy mix from 24% in 2016. Also in 2016, the World Bank suspended financing for the 4.8 MW Inga-3 Basse Chute project in the Democratic Republic of the Congo following the country's decision to deviate from a previously agreed strategic direction. However, the Bank said it would continue dialogue with the government, with the goal of ensuring that the project follows international good practice.
In 2016, Power Africa announced USD 1 billion in new commitments to help double access to electricity in sub-Saharan Africa by adding 30 GW of capacity and 60 million household connections to the grid by 2030. This included 20 new USD 100,000 grants from the US African Development Foundation for African energy entrepreneurs in the newest round of the Off-Grid Energy Challenge. At the 22nd session of the UN climate conference (COP22) in November 2016, Power Africa nad USAID announced USD 4 million in the new investments to eight companies that are revolutionising household solar power across Africa through the Scaling Off-Grid Energy Grand Challenge for Development. The AfDB, through its New Deal on Energy for Africa project, aims to achieve universal access to modern energy services for the continent by 2025. Among the project's goals are to increase off-grid generation by adding 75 million grid connections by 2025, 20 times the current total [45].
A lack of power infrastructure, especially in sub-Saharan Africa, is hindering the region's economic and social development [46]. Over 30 African countries are currently experiencing power shortages, resulting in outages and over-reliance on expensive and often environmentally unfriendly temporary solutions. While the traditional approach has been to increase generation capacity, countries are tending to cooperate more to improve energy access. Greater regional integration through transmission interconnectors and shared power pools is enabling countries to maximise the benefits of abundant, yet unevenly distributed, natural resources. Greater transmission can help alleviate temporary shortfalls in production and further monetise surpluses.

## 8.2 Central Africa Power Sector

Central Africa currently has the lowest electrification rate on the continent, at 20%. In 2010 total installed capacity was 5.6 GW, with a net electricity production of about 20 TWh. Three countries, DRC, Angola and Cameroon, are responsible for more than 80% of production. Approximately 75% of total installed capacity comes from hydropower, with most of the rest from thermal plants.
The analysis of future demand in the region is based on the African Energy Outlook. Electricity demand is expected to increase from about 20 TWh in 2010 to 90 TWh in 2030 (see figure 8.2.1). Urban, industrial and rural demand are projected to account for 57%, 39% and 4% respectively of final electricity demand in 2030. The current share of rural electricity demand is negligible.
All countries in the region except Equatorial Guinea have significant levels of hydro potential. Various sector studies, including the EAPP and SAPP master plans and Platts' database (Platts, 2012) identified hydro projects that amount to more than 30 GW [47].

Because hydropower facilities have a longer lifespan than other power plants only 700 MW of existing generation capacity (5.6 GW) is expected to be retired by 2030. Under the scenario assuming full regional integration, an additional 33 GW in capacity would be needed to meet growing demand between 2011 and 2030. This would imply a total installed capacity of 36 GW by 2030. Renewable sources would account for 29 GW of that total, with hydro being the most prominent (14 GW). The expected full commissioning of the next phase of Grand Inga (Grand Inga 3 Phase 1) would add 4.8 GW in 2023. The installed generation capacity mix between 2010 and 2030 under this scenario is shown in figure 8.2.2.
Hydropower will still be the most common energy source by 2030, but the scenario envisions its share of total generation dropping from a current level of 70% to 45% as potential from other sources is developed.

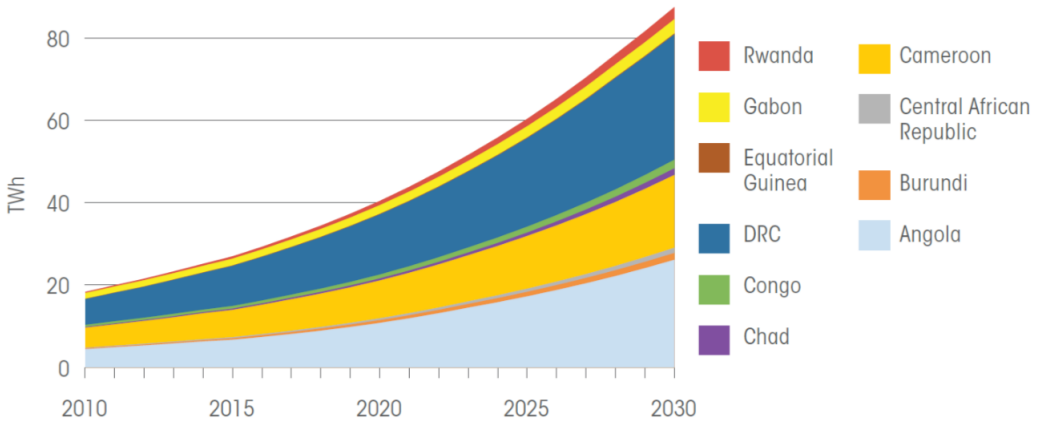


Figure 8.2.1: Electricity demand by Country

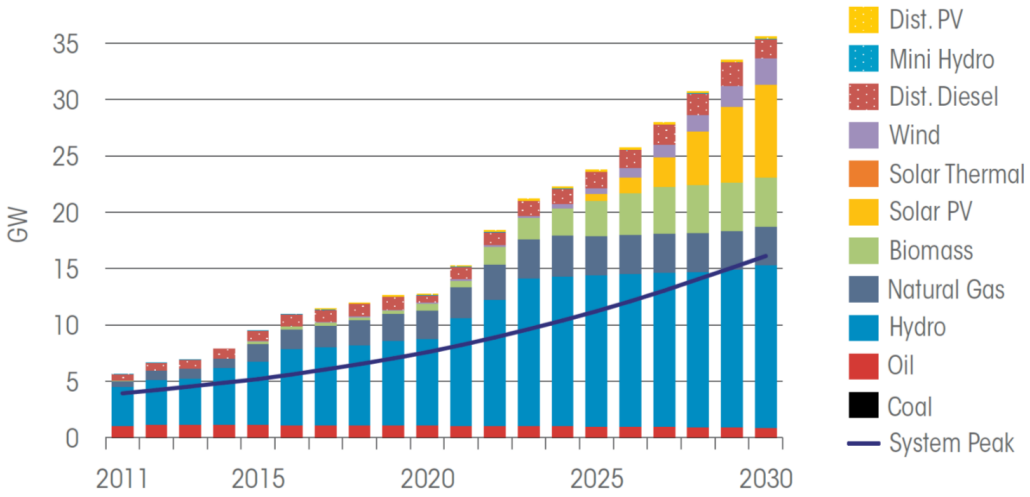


Figure 8.2.2: Installed Capacity by source under the full-integration scenario

## 8.3 Congo

The Republic of Congo has a dense hydrographic system that is organized around two major river basins: the Congo River basin, which covers about 72% of the total area of the country and the Kouilou-Niari, covering about 16%. Other two less important coastal basins are Loémé and Nyanga. Groundwater is also abundant. The potential of hydropower has been estimated to be around 14,000 MW [4].
International organizations, notably the World Bank and the International Monetary Fund, support economic reforms. Privatization and renewing cooperation with international financial institutions are slowly progressing.
The privatization of the national utilities for water and electricity plays an important role in the process of establishing regulatory agencies within these sectors.

**REPUBLIC OF CONGO FACTS**

| | | |
|---|---|---|
| Population | 6.62 | Mio. |
| Access to electricity | 42 | % |
| Installed hydro capacity | 213 | MW |
| Hydro capacity under construction | 19 | MW |
| Share of generation from hydropower | 90 | % |
| Hydro generation | 1,500 | GWh |
| Technically feasible hydro generation potential | 10,000 | GWh |

Figure 8.3.1: Republic of Congo facts

Despite the important river system of the Congo, the power potential is not exploited for the production of electrical energy. So far there are only three hydropower plants existing [48] – HPP Imboulou with 120 MW, HPP Moukoukoulou with 74 MW and HPP Djoué with 19 MW but not in operation since 2007. The Republic of Congo has a technically feasible hydropower potential equivalent to 3,942 MW, of which only about 4% has been developed. A big part of it could be developed in the north of the country in the Plateaux region, the Sangha region and Cuvettes and Cuvettes-Ouest. The south of the country also offers opportunities - almost 1,400 MW. The hydropower plant Chollet with about 600 MW is in planning together with the government of Cameroon. A feasibility study for HPP Sounda (with different scenarios from 600 MW to 1200 MW) is underway. Studies for new greenfield projects HPP Murala (150 MW), Kouembali (150 MW) and Loufoulakari (50 MW) started in 2017.


Figure 8.3.2: Hydropower plants map location in Congo [4]

# Chapter 9

# Renewable Energy in Congo

In this section the potential of the different renewable energy sources is evaluated: wind, photovoltaic and hydropower, in Congo but especially in Oyo in order to evaluate the best solution.

It is then necessary to calculate the energy demand in Oyo. In 2010, Oyo's population was over 5000 inhabitants. According to the data collected by the surveys of recent years, a growth rate of about 23% has been estimated in Congo [49]; therefore this growth rate has been applied to the population of Oyo to have a more updated estimate of the population.
About 6200 inhabitants have been estimated, with an electricity demand of 1223.2 MWh.

## 9.1 Wind Resources

Since the wind is free, operational costs are nearly zero once a turbine is erected. Mass production and technology advances are making turbines cheaper, and many governments offer tax incentives to spur wind-energy development [50].
Wind is a variable resource on a short time scale, his variability is subjected to seasonal variations; the annual variation exists, but it is not so significant.

### 9.1.1 ECMWF and ERA

The European Centre for Medium-Range Weather Forecasts (ECMWF) is an independent intergovernmental organisation supported by 34 states. ECMWF is both a research institute and a 24/7 operational service, producing and disseminating numerical weather predictions to its Member States. This data is fully available to the national meteorological services in the Member States. The Centre also offers a catalogue of forecast data that can be purchased by businesses worldwide and other commercial customers. The organisation was established in 1975 and now employs around 350 staff from more than 30 countries [51].
Some of the services offered by ECMWF are:

- produce numerical weather forecasts and monitor the Earth system;
- carry out scientific and technical research to improve forecast skill;
- maintain an archive of meteorological data.

To deliver this core mission, the Centre provides:

- twice-daily global numerical weather forecasts;
- air quality analysis;
- atmospheric composition monitoring;
- climate monitoring;
- ocean circulation analysis;
- hydrological prediction.

ERA5 is a climate reanalysis dataset, covering the period 1950 to present. ERA5 is being developed through the Copernicus Climate Change Service (C3S). The name ERA refers to 'ECMWF ReAnalysis', with ERA5 being the fifth major global reanalysis produced by ECMWF (after FGGE, ERA-15, ERA-40, ERA-Interim). The next reanalysis, ERA6, is planned for around 2020. ERA5 data is open access and free to download for all uses, including commercial use [52].
It provides estimates of atmospheric parameters, such as temperature, air pressure, wind speed, humidity and also surface parameters such as rainfall, soil moisture, and so on. The reanalysis of this data could be used to monitor changes in the Earth's temperature or to understand other aspects of weather and climate change. "Reanalysis combines model data with observations from across the world into a globally complete and consistent dataset using the laws of physics. This principle, called data assimilation, is based on the method used by numerical weather prediction centres, where every 12 hours at ECMWF a previous forecast is combined with newly available observations in an optimal way to produce a new best estimate of the state of the atmosphere, called analysis, from which an updated, improved forecast is issued. Reanalysis works in the same way, but at reduced resolution to allow for the provision of a dataset spanning back several decades. Reanalysis does not have the constraint of issuing timely forecasts, so there is more time to collect observations, and when going further back in time, to allow for the ingestion of improved versions of the original observations, which all benefit the quality of the reanalysis product. The assimilation system is able to estimate biases between observations and to sift good-quality data from poor data. The laws of physics allow for estimates at locations where data coverage is low, such as for surface temperature in the Arctic. The provision of estimates at each grid point around the globe for each regular output time, over a long period, always using the same format, makes

reanalysis a very convenient and popular dataset to work with" [53].
ERA5 benefits from a decade of research and development and the latest technologies that ERA-Interim did not incorporate. Results show improved global hydrological and mass balance, reduced biases in precipitation, and refinement of the variability and trends of surface air temperature. The enhanced spatial and temporal resolution enables ERA5 to improve on ERA-Interim for many synoptic situations.
To get a better idea of the potential offered by wind, the Word Bank website shows a map of the capabilities of wind power for every country in the world.

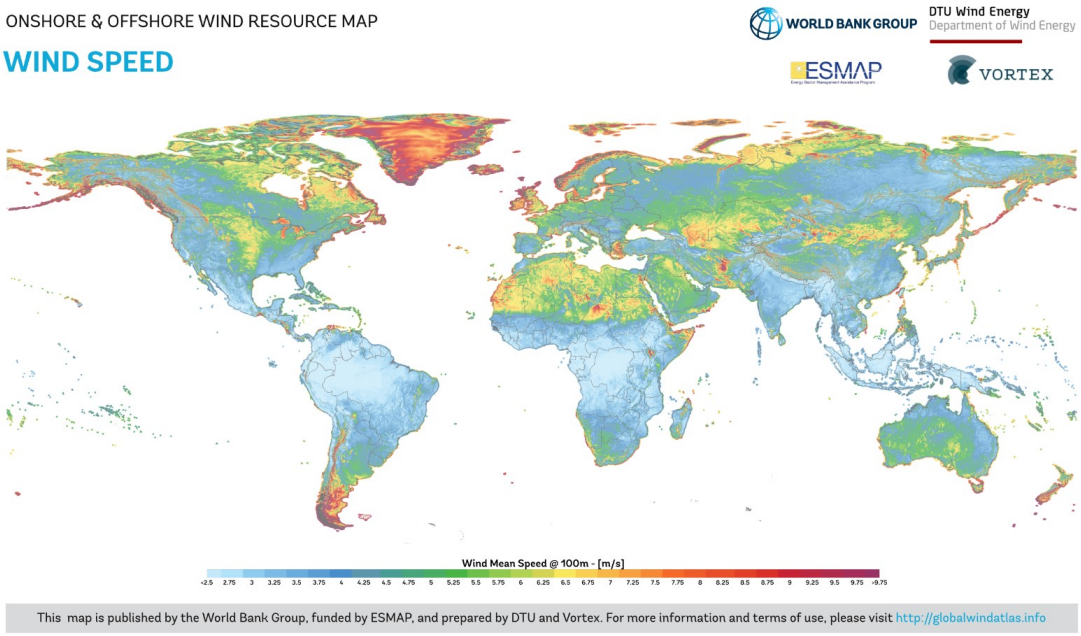


Figure 9.1.1: Global potential wind

Daily temperature changes determine different pressure levels in the atmosphere which leads to the flow of wind , i.e. the movement of air masses in the atmosphere from a higher to a lower pressure area. Forecasts are necessary to maintain grid stability and to allow balance in the electricity generation.

### 9.1.2 Wind Potential in Congo

Through climate reanalysis dataset "ERA5", a wind analysis on the planet can be made. A great deal of information is contained in the archives, available on the website [54]. However, to make an initial preliminary wind analysis, it is necessary to consider the components $u$ and $v$ of the wind speed.

Flow from west to east signifies a positive u component whereas a flow from the south to north the north signifies a positive v component [55].
The wind data from the numerical models and the objective analysis systems are always reported as the magnitude of the component vectors $u$ and $v$. Hence, they are scalar fields. Software packages for looking at weather data will have ways to

combine the $u$ and $v$ wind component data for display of wind arrows or streamlines. The aim of this work is to focus on the magnitude of the wind vector using Pythagorean Theorem involving thw two components $u$ and $v$. These wind speed components, examined for each month in the period of interest, are provided through databases for each geographical coordinate value (latitude and longitude) of interest. Since it is often necessary to manage a huge amount of data that will have to be processed, it is better to use an interface program between the databases and numerical language programs such as MATLAB. One of the software that is widely used for these purpose is Python.

In technical terms, Python is an object-oriented, high-level programming language with integrated dynamic semantics primarily for web and app development. Most importantly, it is an interpreted language, which means that the written code is not actually translated to a computer-readable format at runtime. Whereas, most programming languages do this conversion before the program is even run. This type of language is also referred to as a "scripting language" because it was initially meant to be used for trivial projects. The concept of a "scripting language" has changed considerably since its inception, because Python is now used to write large, commercial style applications. A large majority of web applications and platforms rely on Python, including Google's search engine and also YouTube. Python can also be used to process text, display numbers or images, solve scientific equations, and save data [56].

Referring to the data on ERA5, a grid of the Congo region is created, divided by latitude and longitude. By setting the equator as the reference, the latitudes above the equatorial line are positive, while the longitudes east of the Greenwich meridian are positive.

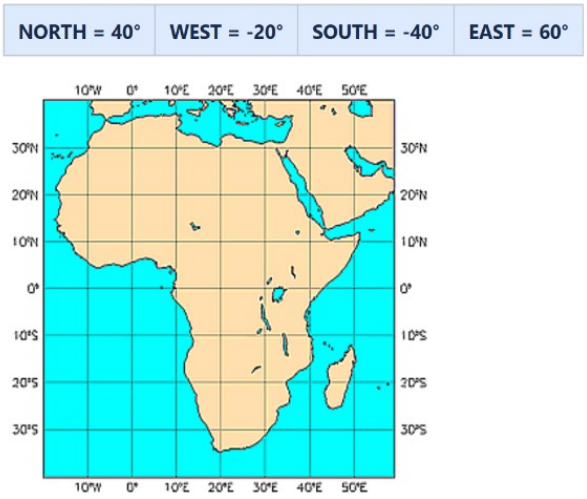


Figure 9.1.2: Partition grid of whole Africa

The ERA5 HRES (high resolution) atmospheric data has a resolution of 31 km, then the base unit of the grid is a square 0,25° x 0,25°. In accordance with these

data, the limits of the Congo partition grid extend to :

North = 4°, Sud = -5°, West = 11°, East = 19°.

The speed data available in the database, 10 or 100 meters, are referred to different heights starting from the surface level. Since the focus of this study was on a small size application for residential use, it was decided to adopt the speed data obtained at 10 meters above ground level, figure 9.1.3. The purpose of this study is to initially quantify the hourly wind speeds along the grid between 1 January 2017 and 31 December 2017; subsequently, after choosing a turbine according to the desired application, with the power curve it is possible to evaluate the corresponding power generated. By applying this procedure for each node of the grid and for each hour of the year, it is possible to determine the annual productivity of the turbine in the entire region of Congo.

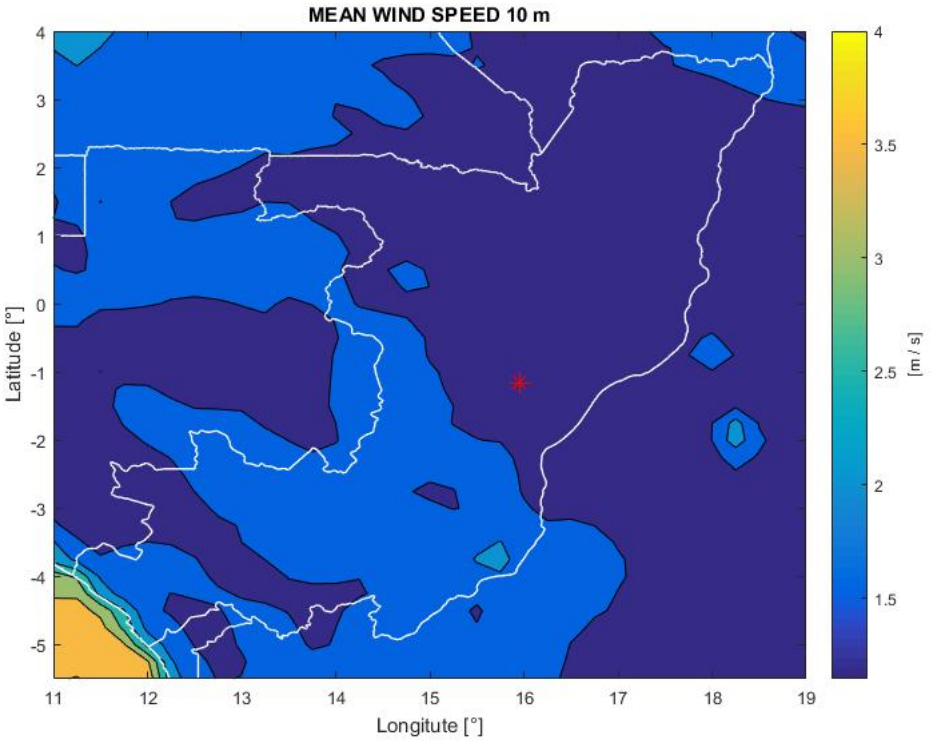


Figure 9.1.3: Congo's mean wind speed 10 at meters height

As can be seen in figure 9.1.3, the average wind speed in the Congo is weak, compared to that required for a feasible wind application. The best compromise for a possible application was achieved by a Honeywell turbine, model WT6500.

The innovative Blade Tip Power System (BTPS) is the patented technology created by WindTronics TM. The Honeywell Wind Turbine utilizes a system of magnets and stators surrounding its outer ring capturing power at the blade tips where


Figure 9.1.4: Honeywell WT6500

speed is greatest, practically eliminating mechanical resistance and drag. Rather than forcing the available wind to turn a generator, the perimeter power system becomes the generator by swiftly passing the blade tip magnets through the copper coil banks mounted onto the enclosed perimeter frame. The Blade Tip Power System addresses past constraints such as size, noise, vibration and output. The enclosed perimeter shrouds the system and is more distinguishable to wildlife. The Honeywell Wind Turbine is a gearless wind turbine that measures just 6 feet (1.8 m) in diameter, weighs 185 lbs (84 kgs) and produces up to 1500 kWh per year depending on height and location.The Honeywell Wind Turbine's BTPS perimeter power system and unique design of multi-stage blades allows the system to react quickly to changes in wind speed. This ensures that the maximum wind energy is captured without the typical noise and vibration associated with traditional wind turbines. The Honeywell Wind Turbine has an increased operating span over traditional turbines with a start-up speed as low as 0.5 mph (0.2 m/s), with an auto shut off at 38 mph (17.0 m/s), traditional gearbox turbines require minimum wind speeds of 7.5 mph (3.5 m/s) to cut in and start generating power [57].

While for some wind turbines that have a rather flat characteristic at high speeds it is easy to determine the rated power, in others such as the one in figure 9.1.5, the decision on which design power to use may be ambiguous. In this case it was decided to adopt as the rated power the value of the power produced at maximum speed (4715 W).
By entering to the x-axis with the respective speeds defined hour by hour in the previous grid, the corresponding power output can be calculated. Making the average of the 8760 hours of the year, the resulting power produced can be displayed in a color map. To measure how much power a wind turbine actually produces compared to how much it would produce if it operated at full nameplate capacity, "capacity factor" concept is introduced. It is an unitless ratio between the actual energy output over a given period of time and the maximum possible electrical energy output over that period [58].

The actual energy production is the sum of all the powers that follow one another hour by hour in each latitude and longitude for the examined grid.

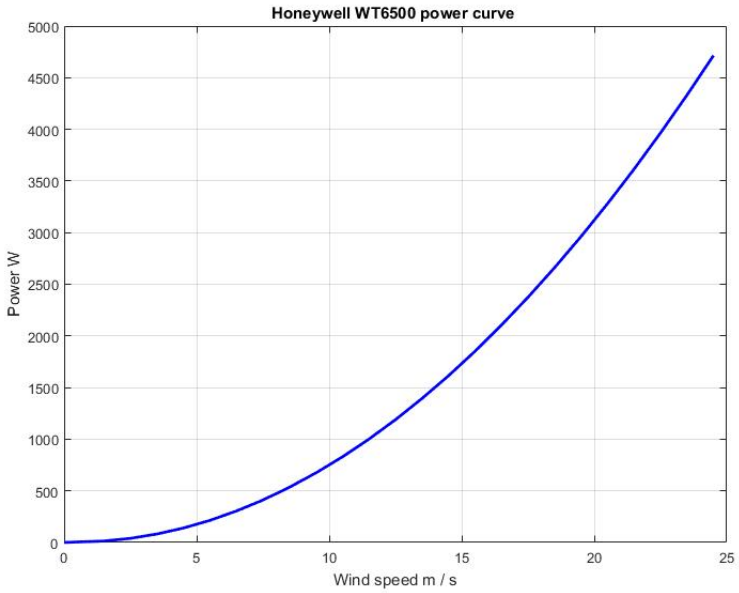


Figure 9.1.5: Power curve Honeywell WT6500

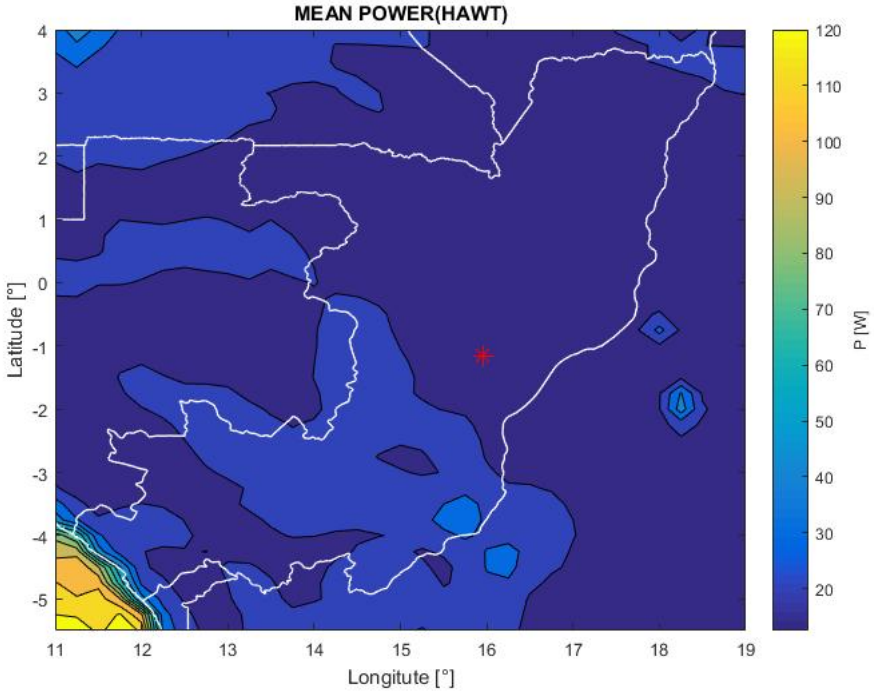


Figure 9.1.6: Mean power of Honeywell WT6500 turbine in the Congo

Typical value of capacity factor are for an onshore wind plant between 18% and 40%, whereas for offshore are between 30% and 45% [59]. The result shown in the figure leads to the conclusion that it is not convenient to use this small wind application

in the Congo. To complete this survey, the values of the capacity factors obtained in the city of Oyo are reported in figure 9.1.8.

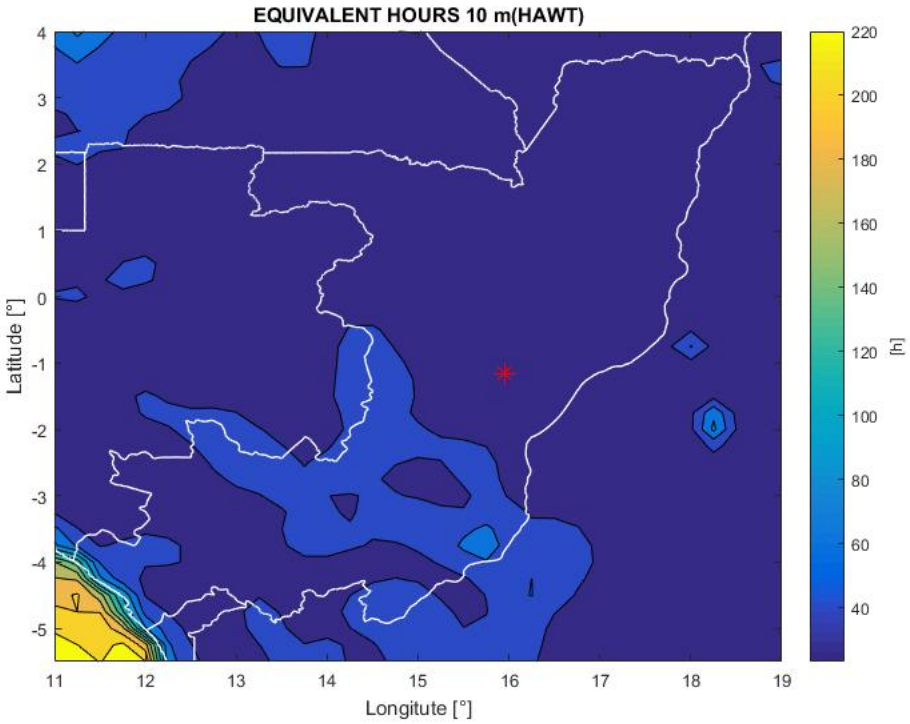


Figure 9.1.7: Equivalent hours Honeywell WT6500

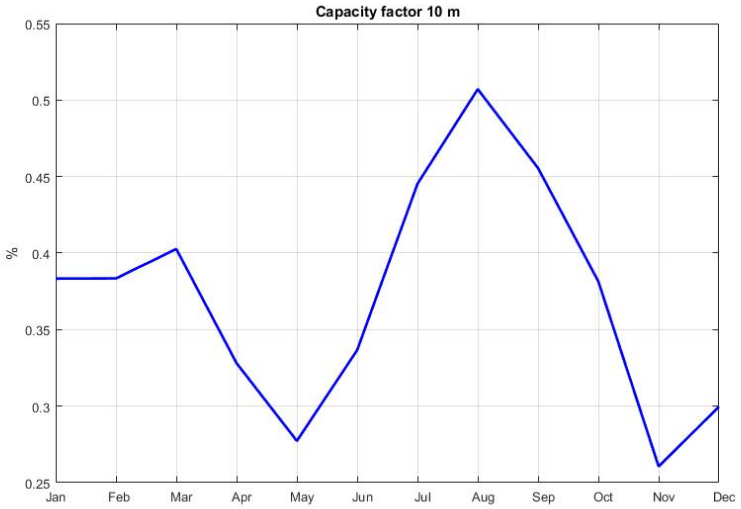


Figure 9.1.8: Monthly capacity factor in Oyo

## 9.2 Solar Resources

On the Global Solar Atlas website [5] it is possible to evaluate some photovoltaic indicators knowing only the geographical data of the location.
To determine annual productivity, it is necessary to study a type of power plant and make some assumptions, as reported for the Global Atlas Source.

- Installed power: 1 kWp;
- Modules:
  - CSI modules, NOCT = 46°C;
  - Temperature coefficient of Pmax = -0.45 $\%/k$;
- Inverters:
  - Efficiency: 97.5%;
- PV installation:
  - Fixed structures North or Sud oriented with optimum tilt angle and with typical row spacing;
- DC losses:
  - Dirt, dust, soiling, frost, snow, DC cabling losses, electrical mismatch, electrical losses of 7.5%;
- Transformer:
  - Standard high efficiency transformer, AC cable losses of 1.5%;

The capacity factor for solar panels is between 15% and 40%. However, with solar energy, the maximum power factor for a fixed photovoltaic system is approximately 27%, since the technology is not able to produce energy at night and even during the day only partial sunlight is available in the early morning or evening.
Since the output of a solar photovoltaic system is directly related to the available peak hours of sunshine, it is possible to calculate the maximum theoretical capacity factor at a given location by dividing the peak hours of sunshine per day by the hours per day [60].

$$MaxCapacityFactor = \frac{Peak \quad Sun \quad Hours \quad Per \quad Day}{24 \quad Hours}$$

For instance, the most favourable locations in the world tend to have 6.5 peak sun-hours per day, in these cases the capacity factor would be:

$$MaxCapacityFactor = \frac{6.5 \quad Hours}{24 \quad Hours} = 0.27 = 27\%$$

As can be seen in figure 9.2.1, the results are summarized in the hours equivalent map and the capacity factor graph.

Specifically for Oyo's location, the main two values are:

- Photovoltaic output (PVOUT)= 1434 $kWh/kWp$ per year (around 16% of annual use);
- Global total irradiation (GTI)= 1865 $kWh/m^2$ per year;

The capacity factor has been determined using the PVGIS software available on Internet. PVGIS is a free online photovoltaic solar energy calculator for stand-alone or grid-connected PV systems in Europe, Africa and Asia.
As a Geographic Photovoltaic Information System, it offers a googlemap application that makes it easy to use.
This application calculates the monthly and yearly potential electricity generation E $[kWh]$ of a photovoltaic system with defined modules tilt and orientation.
The characteristics of the system and the typology of the power plant evaluated are:

- PV technology = Crystalline silicon modules;
- Installed peak power = 1 kWp;
- Estimated system losses = 14%;
- Fixed mounting position with:
  - Optimal slope: 4° (tilt angle is 94°);
  - Optimal azimuth: -172° (north direction is -180°);

For this analysis a system with a peak power of 1 kWp has been chosen so that the actual power of the system to be set can be calculated more easily.

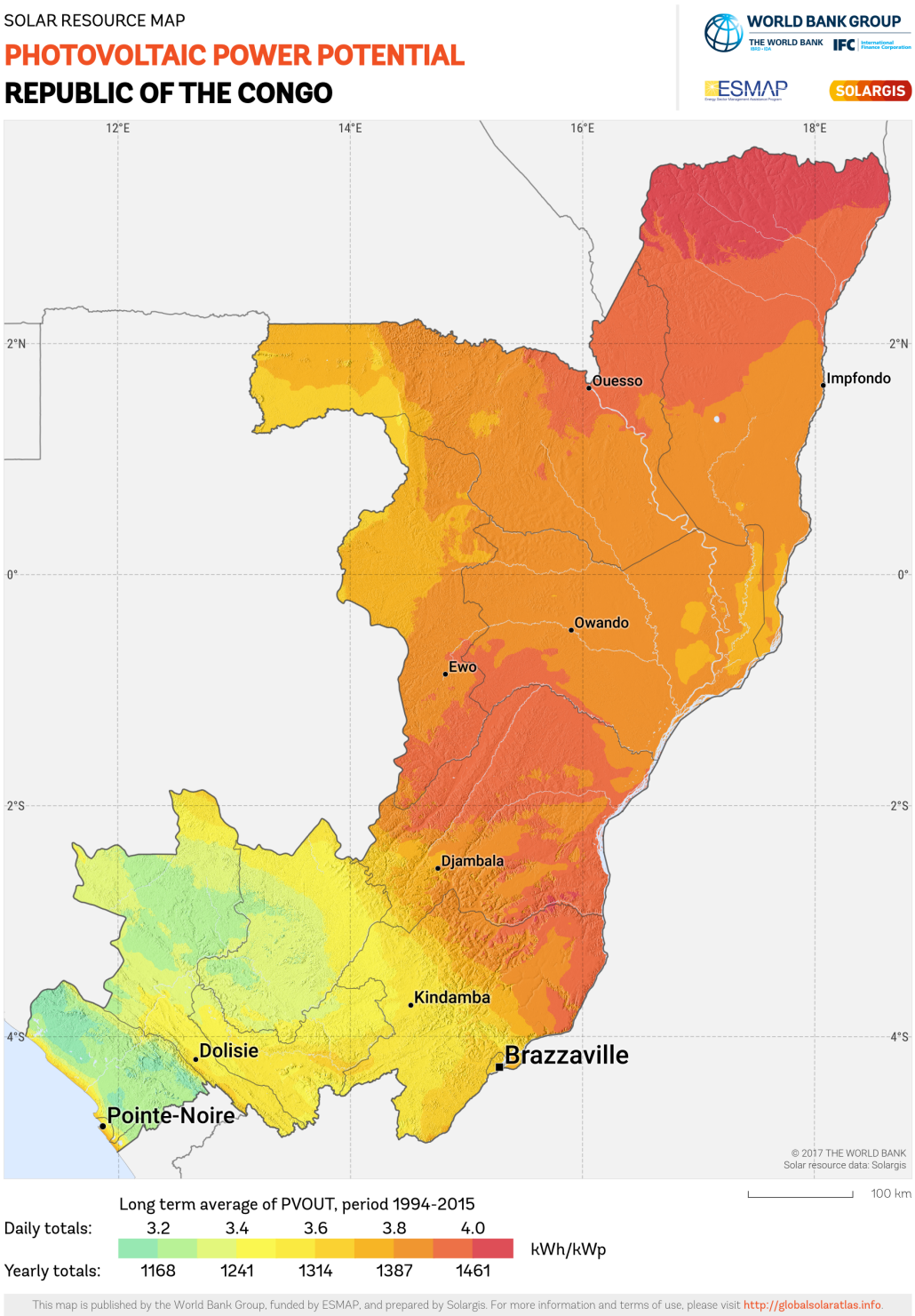


Figure 9.2.1: Photovoltaic power potential [5]

Data were implemented on MATLAB to obtain the following graphs:

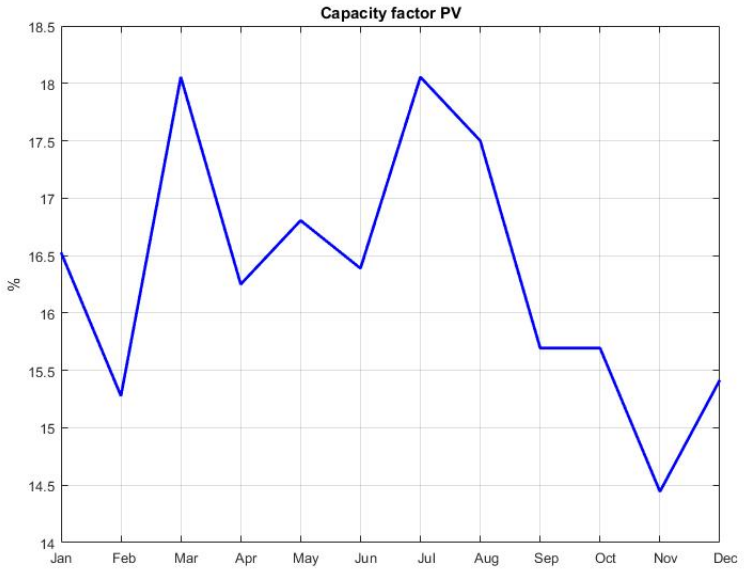


Figure 9.2.2: Capacity Factor PV

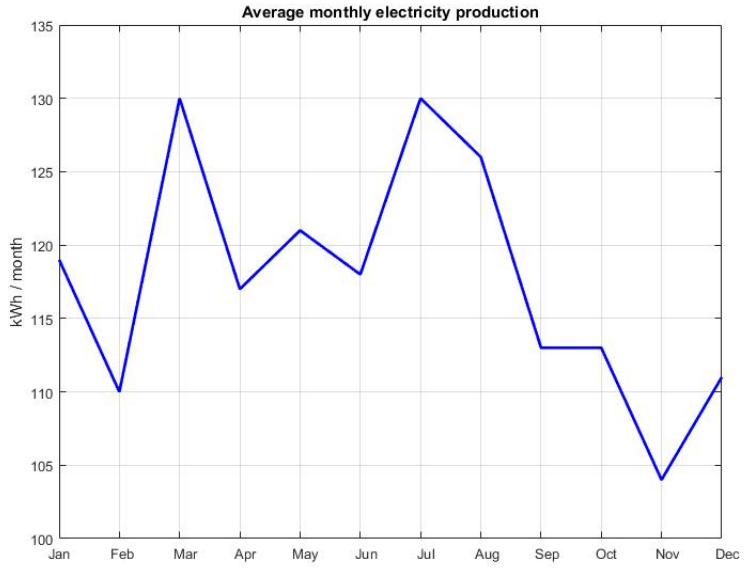


Figure 9.2.3: Average monthly electricity production

Although the potential of solar energy in the Congo would bring great benefits, only a small part of the photovoltaic energy can be used because of the highly forested nature of this country.

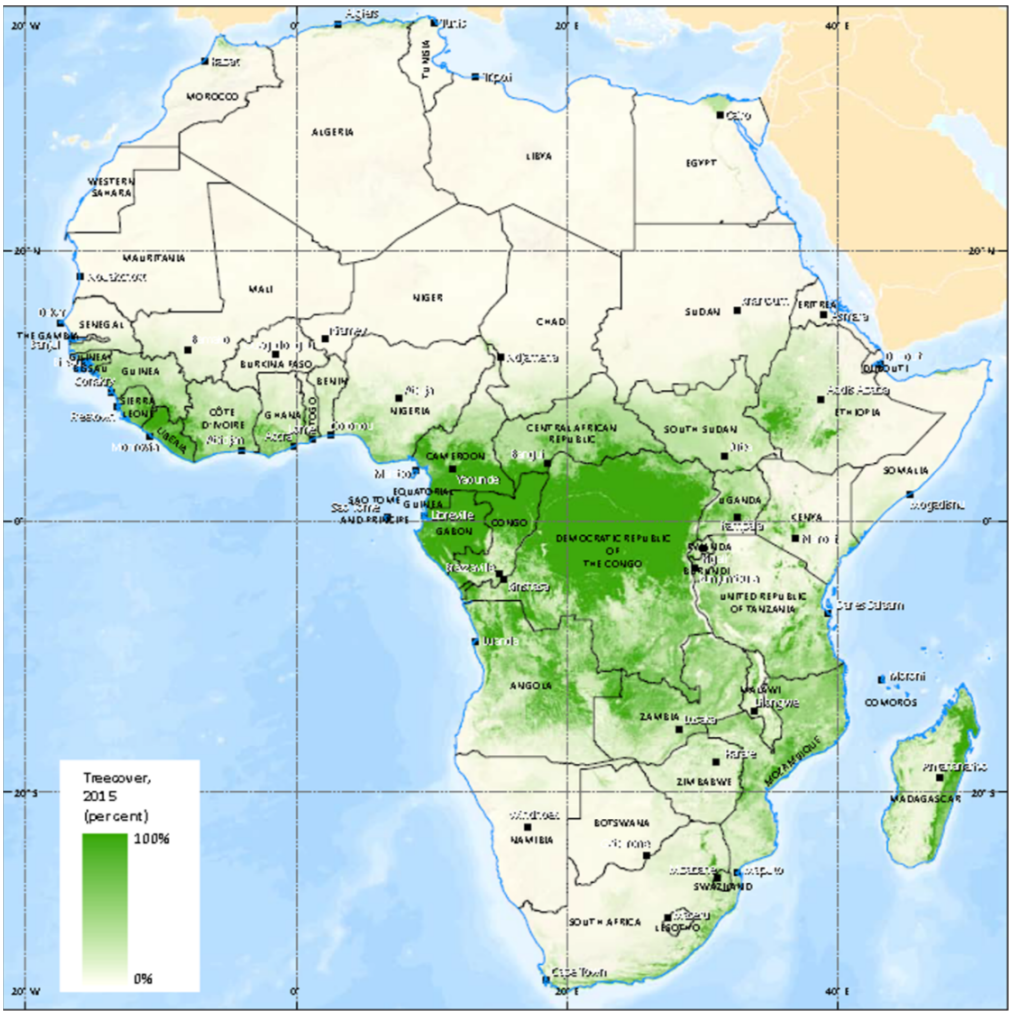


Figure 9.2.4: Treecover 2015 [6]

## 9.3 Hydropower Resources

Hydropower installed capacity in 2011 was 89 MW and accounted for 78 per cent of total net electricity generation (WEC, 2013). Although this country has huge potential for hydropower generation, estimated at 2,500 MW, less than 5 per cent has been developed. There are currently three hydroelectric dams: Imboulou (120 MW), Moukoukoulou (74 MW) and Djoue (15 MW). The government is looking for investors to participate in the planned Sounda Gorge dam, with an estimated capacity of 1,200 MW (REEEP, 2012).

Despite the rich energy resources, less than half of the population of the Republic of the Congo has access to electricity; only 11.7 per cent of rural and 58.9 per cent of urban areas are electrified (World Bank, 2016).
This is due to a severe deficiency in electricity infrastructure as a result of the civil war. Until the distribution network is improved, biomass will remain the major fuel, especially in the countryside. Only a quarter of the population uses modern fuels. This figure is very low in the rural areas (5 per cent) but higher in urban areas (36 per cent) (World Bank, 2015).
The energy intensity (the ratio of the quantity of energy consumption per unit of economic output) of the economy was 2.9 MJ per US dollar (2005 dollars at PPP) in 2012, down only slightly from 2.6 MJ per US dollar in 1990. The compound annual growth rate (CAGR) between 2010 and 2012 was 2.29 (World Bank, 2015).

The Republic of the Congo also has extensive hydropower potential, but most of it remains untapped. The share of renewable energy in the total final energy consumption (TFEC) has been on the decline after a small spike to 72.7 per cent in 2000 before falling to just under 50 per cent in 2012.
The Republic of the Congo aims will be to developing more of its rich hydro-electricity resources with the objective of increasing the share of electricity from hydro sources to 85 percent by 2025.

Due to the low potential of renewable wind and photovoltaic resources and also thanks to the presence of the Alima river near the location considered by this study, the analysis of hydrokinetic turbines to be installed in the river was further deepened.

# Chapter 10

# Alima River

Alima River is a tributary of the Congo River. It is formed by the confluence of two streams, the Lékéti and the Dziélé. It is navigable for about 320 km, and it wets the cities of Okoyo, Boundji and Oyo along its path.

**Alima River**

| | | |
|---|---|---|
| Lenght | 500 | $km$ |
| Width | 140 | $m$ |
| Average Depth | 5 | $m$ |
| Average Flow Rate | 600 | $m^3/s$ |

The purpose of this document is to deal with the realization of turbines, near the city of Oyo, for the supply of electrical energy. Information on river width ($\sim 97m$), where the turbines are supposed to be placed, was obtained by using Google maps. About river depth, it was obtained from [61] and [62], but it is just an average depth. The average flow rate value was obtained from [63], [64] and [65] although these documents are not very recent.

## 10.1 Water Speed Analysis

$$Area = width \text{ x } depth = 97 \text{ x } 5 = 485m^2$$

$$V = \frac{Q}{A} = \frac{600}{485} = 1.24m/s$$

$V$ =Velocity $[m^2/s]$;
$Q$ =Average flow rate $[m^3/s]$;
$A$ =River Section $[m^2]$;
$\rho$ =Water density at 25°C $[kg/m^3]$;

For the convenience of study, a rectangular section of the river and a constant speed distribution over the entire section have been adopted.
As previously written, some information has been found in not recent documents,


Figure 10.0.1: Bridge width, where turbines are supposed to be anchored

consequently, in order to confirm the value of the velocity, other methods for calculating the velocity have been performed.

Other calculation methods for water velocity were adopted to validate the result.

In the field of hydraulic engineering, the Chézy equation is derived from hydrodynamics theory developed in 1775 by Antoine de Chézy, to calculate the velocity of a fluid in a duct, both under pressure and free water surface.

$$V = u_c C R_h^{\frac{1}{2}} S_P^{\frac{1}{2}} \tag{10.1.1}$$

$V$ =Average Velocity $[m/s]$;
$u_c$ =A conversion factor for Manning and Chézy formula (see table 10.1);
$C$ =Chézy's roughness coefficient $[m^{\frac{1}{2}}/s]$ (parameters that reflect the stream morphology);
$R_h$ =Hydraulic radius $[m]$;
$S_P$ =Slope of free water surface $[m/m]$

In addition, there is another relation to calculate the water velocity. The Manning equation is an empirical formula estimating the average velocity of a liquid flowing in a conduit that does not completely enclose the liquid, i.e., open channel flow. However, this equation is also used for calculation of flow variables in case of flow in partially full conduits. The equation was made by the French engineer Philippe Gauckler in 1867 and later re-developed by the Irish engineer Robert Manning in 1890.

$$V = \frac{u_m}{n_m} R_h^{\frac{2}{3}} S_P^{\frac{1}{2}} \tag{10.1.2}$$

$n_m$ =Manning's roughness coefficient;
Equations (10.1.1) and (10.1.2) are very similar, the only differences are the unit conversion factors, lumped coefficients, $n_m$ and $C$, and the exponent of hydraulic radius.
Chézy factor $C$ may be considered within both the Manning coefficient $n_m$ and the hydraulic radius (or depth) $R_h$ according to this equation:

$$C = \frac{u_m R_h^{\frac{1}{6}}}{u_c n_m}$$

Average stream velocity $V$ depends on the stream area $A$, morphology, and slope $S_P$. The product between the cross-sectional area of the stream ($A$ = width·depth) gives the stream discharge $Q$.

The hydraulic radius $R_h$ is sort of "equivalent radius" and it is expressed as the ratio between cross-sectional area of the flow A and the wetted perimeter of the cross-section $P_r$.
For wide and shallow streams (depth $<$ 0.05 width), the hydraulic radius is essentially the average depth, $R_h \sim h$.

| **Units on V** | **Units on $R_k$** | $u_m$ | $u_c$ |
|---|---|---|---|
| feet/second | feet | 1.49 | 1.00 |
| meters/second | meters | 1.00 | 0.552 |
| cm/s | cm | 4.64 | 5.52 |

Table 10.1: A-Unit conversion factor for Manning and Chézy Formulas

| **Channel Condition[s]** | $n_m$ | **Variability** | **Roughness [mm]** |
|---|---|---|---|
| Glass | 0.010 | ±0.002 | 0.3 |
| Painted Steel | 0.014 | ±0.003 | 1 |
| Unfinished Concrete | 0.014 | ±0.002 | 1 |
| Corrugated Metal | 0.016 | ±0.005 | 37 |
| Masonry Rubble | 0.025 | ±0.005 | 80 |
| Ravelly | 0.025 | ±0.005 | 80 |
| Natural Clean & Straight | 0.030 | ±0.005 | 240 |
| Major Rivers | 0.035 | ±0.010 | 500 |
| Sluggish Reaches & Deep Weedy Pools | 0.065 | ±0.015 | 900 |

Table 10.2: B-Some typical values of Manning's n for various type of streams and aqueducts [2]

Where no value for $n_m$ is defined, it may be estimated from the roughness of the river bed: $n_m = 0.121\epsilon^{\frac{1}{6}}$ where the roughness $\epsilon$ is in millimeters.
Applying the Manning's equation:

$$V = \frac{1}{0.03} 5^{\frac{2}{3}} 0.0002^{\frac{1}{2}} = 1.38 \quad m/s$$

Using Google Earth pro, has been measured the water slope ($S_P$= 0.0002 m/m) of the river near the Oyo's bridge.
Alima river has a tropical forest ecosystem and exhibit the classical features of the so-called "Black Rivers": low pH, high dissolved and particulate organic matter concentrations, low total inorganic suspended and dissolved loads. For the roughness coefficient $n_m$, has been choose a value like natural clean in case of straight river ($n_m$ = 0,03) reported above in table 10.2.
The hydraulic radius can be simplify using the depth value because satisfy the condition above mentioned.

A graphical method to calculate the speed has also been used (figure 10.1.1). It consists in drawing two lines: one that connects the Manning's coefficient with the hydraulic radius and another that connects the intersection point of the first line with the A scale with the slope. The intersection of the latter line with the speed scale detects the value of the water velocity.

The value of the velocity is about 1.3 m/s.

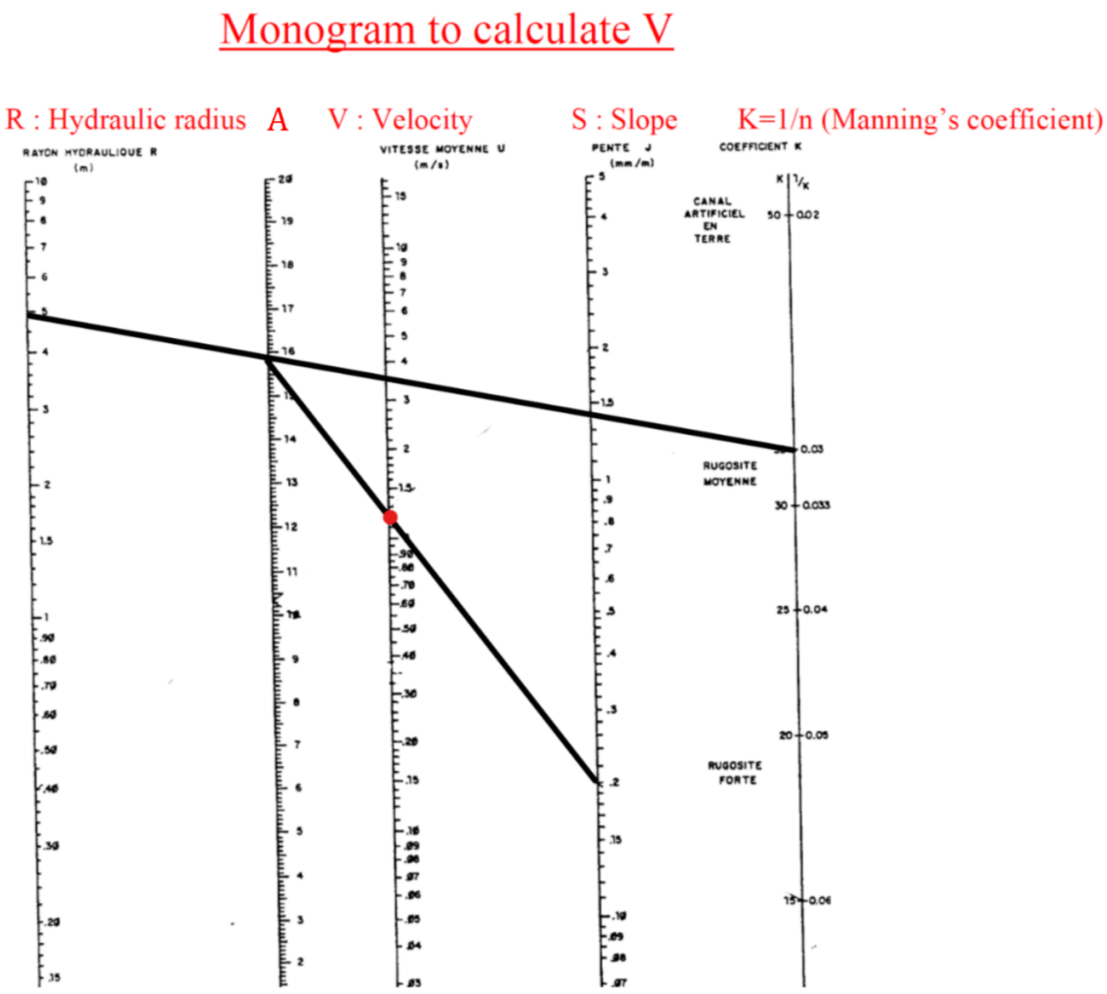


Figure 10.1.1: Monogram to calculate V

## 10.2 Monthly Velocity Variability

Since we have more confirmation on the average flow of rivers, it would be useful to calculate how climate affect could change the trend of velocity. For this reason, there are different approaches in the literature to take into account natural and meteorological factors. One of these is the principle of mass conservation applied to the hydrological system, known as the water balance model.

The water that flows into the soil through precipitation can undergo different processes: evapotranspiration, surface runoff or can be stored in the soil.

Describing the water balance of a basin or sub-basin is often a starting point for understanding its hydrology. The standard equation is generalized as:

$$P = E + Q \pm S$$

where $S$ is the change in water storage over some given time period; P and E are the amounts of precipitation and evaporation during that same time (E includes evapotranspiration in this generalization); and $Q$ is net outflow from the basin, which is often considered the summed river discharge during the given time but can also include groundwater fluxes. The following subsections describe our understanding of each of these values [66].

## 10.3 Rainfall

The rainfall investigation was conducted using the Word Bank Group website. By indicating the location of the site of interest and the time period in question, an average annual rainfall trend was obtained.
The time range used for the study in Oyo was from 1991 to 2015 (see [67]).

The average rainfall in the 'Cuvette Centrale' ranges between 1400 and 1800 mm/year [68]. The rainfall average in Oyo is 1676 mm/year. In general, the rainfall trend matches the trend in the whole country. The rainfall trend significantly influences the flow of the river, in fact, according to the source [68], the flow rates of the Congo River are characterized by a bimodal flooding pattern, consisting of high water in October and November, a secondary peak in April and May, low water in August and a secondary minimum in January and February.

## 10.4 Evapotranspiration and Temperature

Compared to precipitation, less information is published regarding evapotranspiration and temperature.
The term evapotranspiration refers to the water that is transferred from the catchment area to the atmosphere by evaporation from the liquid mirrors and soil, and by transpiration from plants. For practical purposes it is of little importance to

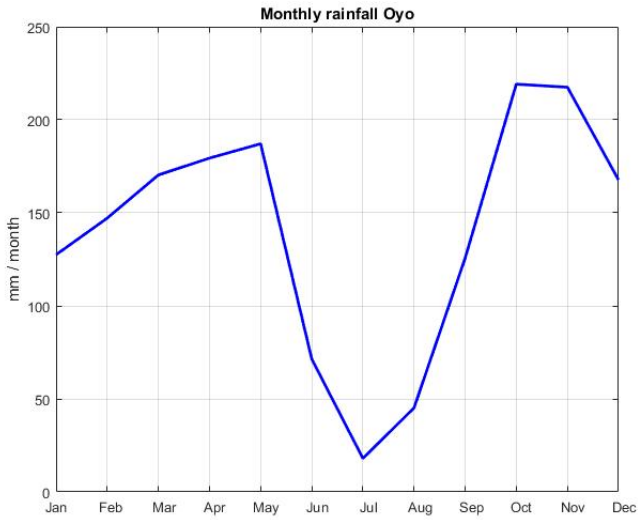


Figure 10.3.1: Monthly rainfall in Oyo

know the amount of water that passes in one way or another because the global phenomenon is the result of the overlapping of both phenomena.
Under the same conditions, as the availability of water increases in the soil, the value of evapotranspiration will increase also, but this will not indefinitely. There will be an evapotranspiration limit value that will not be exceeded even for greater availability of water. This limit value is called potential evapotranspiration.

Definitions:

***ET* - Real evapotranspiration:** also called actual evapotranspiration. It is the result of soil-vegetation-atmosphere interaction.
It depends on:

1. Evaporating power of the atmosphere;
2. Vegetation (type, development and stage of growth);
3. Water content of the soil.

***ET*$_p$ - Potential evapotranspiration:** it is evapotranspiration that occurs when the water content of the soil is not a limiting factor for it. The availability of water in the soil is at least equal to the amount of water that the soil-vegetation-atmosphere system is able to evaporate.
It depends on 1. (evaporating power of the atmosphere) and 2 (vegetation).

$$ET \leq ET_p$$

***$ET_{p0}$* - Reference potential evapotranspiration:** It is the evapotranspiration from a dense and uniform grassy cover well irrigated, 8-15 cm high, in the growth phase. We refer to it to eliminate the dependence on point 2 (vegetation). $ET_{p0}$ depends only on climatic conditions.

Estimating procedures:

- $ET_{p0}$: There are some methods and equations to estimate $ET_{p0}$, based on environmental parameters.
- $ET_p$: This is obtained by multiplying $ET_{p0}$ with a coefficient that depends on:
  - type of crop
  - stage of vegetative development
- $ET$: Indicates the actual loss of resource from the basin and depends on the water content of the soil. The vegetative activity of the plants, in fact, is reduced when the water content of the soil becomes lower than the critical value and stops completely below the point of withering.

Since in the calculation of both $ET$ and $ET_p$ are necessary environmental parameters whose value is not known, in this study was taken into account the value of $ET_{p0}$, knowing that this value is higher than the other two and therefore should generate a greater variability of the flow rate allowing to work under the worst possible conditions.

To calculate $ET_{p0}$ reference potential evapotranspiration, different methods can be used, depending on the availability of the data and the accuracy of the estimations to achieve.
The most common methods are:

- Evaporation method
- Thornthwaite Method
- Blaney and Criddle method
- Penman's Method

The few known parameters allow only the Thornwaite method to be used. Descriptions of other methods can be found in [69].

**Thornthwaite method** allows estimation of evapotranspiration reference potential, expressed in centimetres on a monthly basis (cm/month) using only information of the trend of the monthly average temperatures $T$. This equation was proposed for the purpose to simulate hydrological phenomena in the basin with the aim of assessing the irrigation deficit.

The formula is written:

$$ET_{p0} = cT^a$$

As already mentioned, T represents the average temperature of the month, expressed in degrees centigrade, while $c$ and $a$ are two parameters that depend on the climate of the site.
The parameters can be expressed as a function of the annual thermal index expressed by the equation:

$$I = \sum_{i=1,12} (T_i/5)^{1.514}$$

where $T_i$ indicates the average monthly temperature. Parameters $a$ and $c$ take the form:

$$a = 0.016I + 0.5$$
$$c = 1.6(10/I)^a$$

The temperature values, from 1991 to 2015, were found on the Word Bank Group website (figure 10.4.1) .

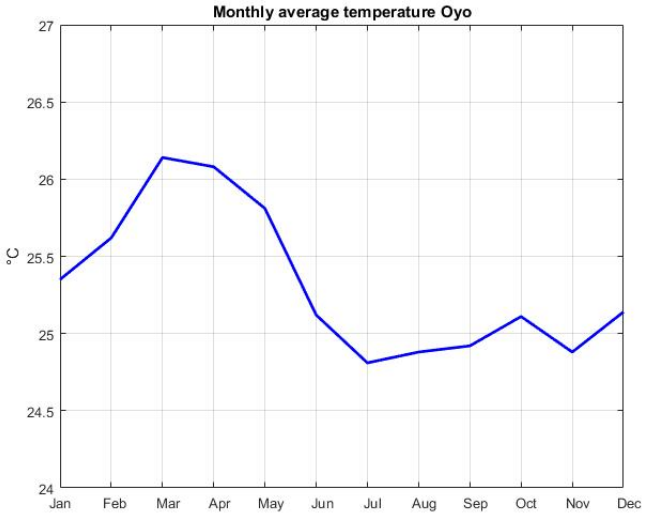


Figure 10.4.1: Monthly Temperature in Oyo

Applying the Thornwite equation one obtains the trend of the reference potential evapotraspiration. In the equation of the water balance the value of the real evapotranspiration should be put, however due to the lack of data about the vegetation, quantity of water contained in the soil etc. it was decided to approximate it with the reference potential evapotranspiration (figure 10.4.2). The reference potential evapotraspiration average in Oyo is 1543 mm/year.

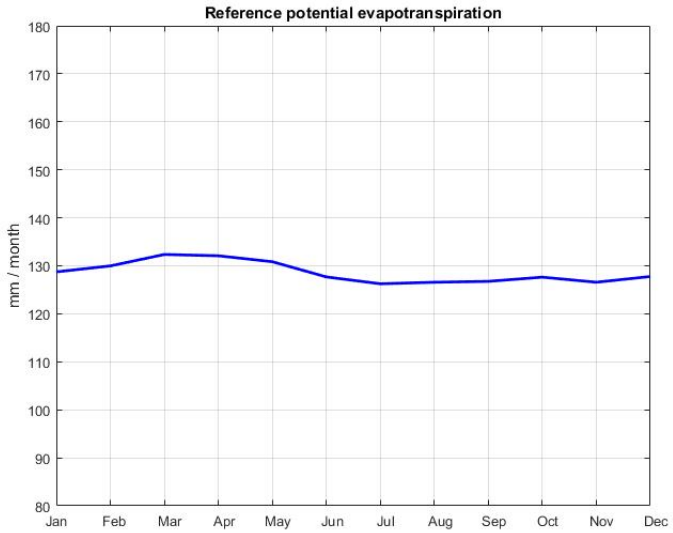


Figure 10.4.2: Monthly evapotraspiration in Oyo

## 10.5 Total Water Storage

Until a few years ago, there was no information on the water that storage in the ground in a wet regions such as the Congo river basin because it was too difficult to determine the distribution of vegetation.
Satellite gravimetry remains the only technique that provides information on the total water storage change at continental scales and gives access to groundwater variations when a priori information on surface and sub-surface reservoirs is available. Data of the Gravity Recovery and Climate Experiment (GRACE) mission were widely used to estimate changes in land water storage and fluxes over Africa at basin to regional scales. By using the first two years (April 2002 to May 2003) of GRACE data, the study of seasonal total water storage (TWS) variations vary between $\pm 50$ mm of TWS in the Congo and Niger basins.
Since its launch in 2002, the Gravity Recovery and Climate Experiment space mission has measured, for the first time, changes of total water storage , including surface water, soil, moisture and groundwater, with unprecedented centimeter accuracy in terms of geoid height. GRACE data have already demonstrated a strong potential for estimating hydrological system information, such as river discharges and evapotranspiration rate [70].
Thanks to some documents, estimates of the total water storage near Oyo have been found; these data have been processed and inserted into the equation of the water balance.
However, since no other document was found to confirm what was reported by these documents, it was decided to use experimental data that will be introduced in the next section.

## 10.6 Conclusion

The equation of the water balance with the data described previously has been applied, obtaining the trend of the river's flow rate (figure 10.6.1). Subsequently, the speed was calculated as the ratio between the water flow and the section of the river (figure 10.6.2).

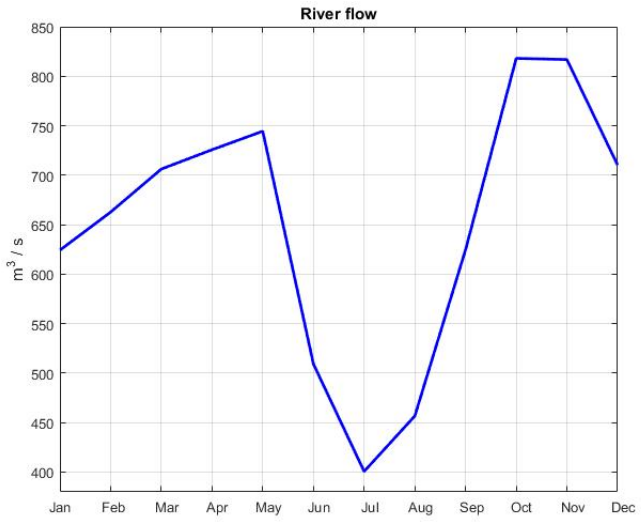


Figure 10.6.1: Alima water flow

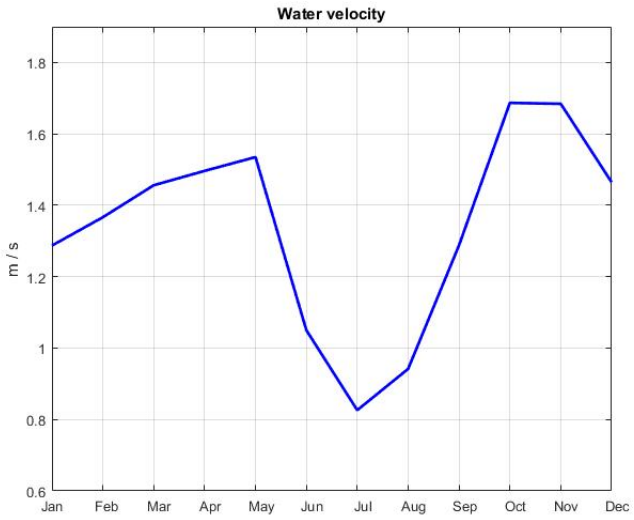


Figure 10.6.2: Alima water velocity

As mentioned previously, due to the difficulties to calculate the precise variability of the flow rate by applying the water balance equation caused by some unknown

experimental parameters, it was only possible to give an approximate estimate of the flow rate. However, through further research, some experimental data on the flow of the Alima river near Tchikapika, a district of the Republic of Congo not far from Oyo, have been found [71]. These data, however, refer to the years between 1952 and 1994, but since these are the only data available to us, they will be those used in this study. We would like to point out that the previously estimated data do not differ much from the experimental data.

| **Jan** | **Feb** | **Mar** | **Apr** | **May** | **Jun** | **Jul** | **Aug** | **Sept** | **Oct** | **Nov** | **Dec** |
|---|---|---|---|---|---|---|---|---|---|---|---|
| 602 | 595 | 598 | 606 | 617 | 582 | 513 | 498 | 533 | 598 | 639 | 632 |

Table 10.3: Average monthly flow rate $[m^3/s]$ measured at the Tchikapika hydrometric station (1952-1994)

| | | |
|---|---|---|
| Average Flow Rate | 584 | $m^3/s$ |
| Average Water Speed | 1.28 | $m/s$ |
| River Section | 456 | $m^2$ |

Table 10.4: Average annual data measured at Tchikapika station (1952-1994)

The section of the river was recalculated using experimental data.
A further confirmation of the work done previously, regarding the variability of the flow rate, is [64]. In fact, the flow and rainfall trends in the Congolese basin, where Oyo is also located, have been analysed. From figure 10.6.3 it can be seen that even if the quantity of discharge is different, it reproduces fairly well the trend found previously.

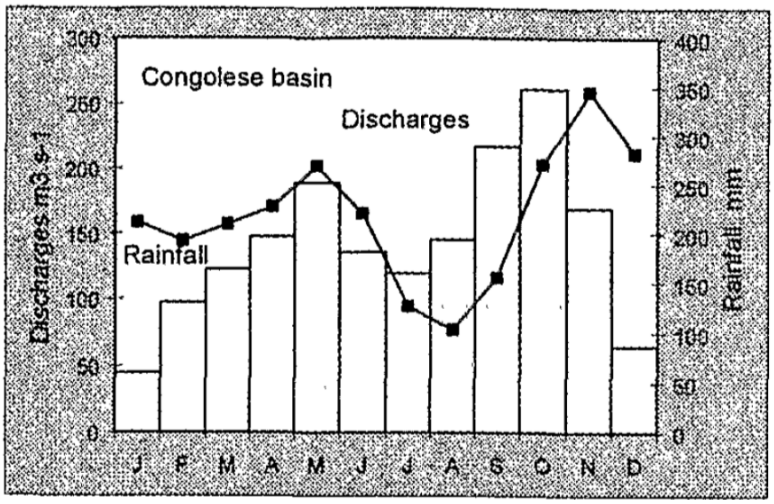


Figure 10.6.3: Typical mean rainfall charts and hydrological regimes of the Congolese basin (Ouesso station: 1966-94) (Likouala Mossaka à Makoua: 1953-93).

# Chapter 11

# Open-source

Through a research on the web it is possible to find some open-source for the design of hydrokinetic turbines; In this section are described the functionality of some of these. Typically these open-sources are based on blade element momentum theory or rotor lifting line theory. *HARP_Opt* and *OpenProp* are representative open-source engineering codes for preliminary design of axial-flow turbines. (*OpenProp* is also useful for marine propeller design, hence itsname). *HARP_Opt* employs blade element momentum theory and uses a multi-objective genetic algorithm to maximize annual energy production subject to constraints such as cavitation. *OpenProp* employs rotor lifting line theory and principles from variational calculus to optimize the blade load distribution (lift coefficient) for maximum power extraction,with options for blade geometry(chord and thickness) optimization subject to cavitation and stress constraints. OpenProp also provides performance curves for off-design flow conditions, blade cavitation and stress analyses, and geometry outputs for visualization and modeling. Engineering models have also been developed for crossflow turbines, such as *CACTUS* and *CyROD*. The *CyROD* model accounts for six load effects: steadylift, steadydrag, lift due to flow curvature, unsteady lift, added mass, and acceleration reaction. Both models employ a vortex-lattice formulation with a free-wake model, with shed vorticity advected with the free stream plus the induced velocity field for more accurate performance predictions [72].

## 11.1 Harp_Opt

The *HARP_Opt* (Horizontal Axis Rotor Performance Optimization) code utilizes a multiple objective genetic algorithm and blade-element momentum (BEM) theory flow model to design horizontal-axis wind and hydrokinetic turbine rotors. Genetic algorithms solve optimization problems by mimicking the principles of biological evolution. Using rules modeled on biological reproduction and gene modification, genetic algorithms repeatedly modify a population of individuals to create subsequent generations of "superior" individuals. *HARP_Opt* utilizes the MATLAB Genetic Algorithm solver to perform this optimization, and the *WT_Perf* BEM theory code to predict rotor performance metrics.
*HARP_Opt* optimizes a rotor's performance for steady and uniform flows (no sheared or yawed flows). A variety of rotor control configurations can be designed using

*HARP_Opt*, including fixed or variable rotor speed and fixed or variable blade pitch operation. Blades with circular or non-circular roots can be designed using *HARP_Opt*. *HARP_Opt* can function as a single or multiple objective optimization code. The primary optimization objective is to maximize the turbine's annual energy production (AEP). Annual energy production is calculated using a Rayleigh, Weibull, or user-defined flow distribution. Maximum power is bounded, and maximum power point tracking (MPPT) is a combined objective with AEP. For hydrokinetic turbines, additional constraints are defined such that cavitation will not occur. An additional objective can be activated, in which *HARP_Opt* performs a structural analysis to minimize the blade mass. For the structural analysis, the blade is modeled as a thin shell of bulk isotropic material, and the blade mass is minimized using a maximum allowable strain as the constraint. Maximizing energy production and minimizing blade mass are conflicting objectives, thus *HARP_Opt* will identify the set of Pareto optimal solutions. To meet these objectives, *HARP_Opt* calculates the optimal blade shape (twist, chord, and airfoil/hydrofoil distributions) and optimal control of the rotor speed and blade pitch.

### 11.1.1 Analysis of Algorithm parameters in *HARP_Opt*

The HARP_Opt code is mainly composed by 2 algorithms: the first algorithm is used for the BEM theory, also known as WT_Perf, whereas the second is a genetic algorithm code as a single or multiple objective optimization.The primary optimization objective is to maximize the turbine's annual energy production (AEP). This can be done by using not only the Rayleigh and Weibull distributions, but also a user-defined speed distribution. The second objective is to maximize the turbine efficiency, but does not necessarily create a turbine with the highest AEP.
In this initial phase to approach to the software, in addition to the guide in the enclosure, some preloaded examples were also taken into account.

*HARP_Opt* defines the shape of the blade through the use of curve fits. The twist, chord, and thickness distributions are all required to be monotonically decreasing. As figure 11.1.1 illustrates, five control points are defined for the twist and chord distributions, and then a 5th order Bezier curve is fit through the control points. The genetic algorithm determines the optimal twist and chord values of the control points, but the radial location of the control points remain fixed. The radial location of the control points are spaced using half-cosine spacing (with higher density towards the hub) or equal spacing where blade element centers being equally spaced along the length of the blade. Since in this analysis are chosen to use the corrections for hub and tip losses, "Cosine" spacing results as the better solution.

The hydrofoil profile chosen for the study is the NACA 4415 with a blade configuration equal to the example reported by the producer. In the second version of *HARP_Opt*, the same used in this treatment, a graphic user interface (figure 11.1.2) has been inserted to facilitate the parameters setting in the software.

For the BEM algorithm settings, all available corrections have been used except for the stall delays models.One of the simplifying assumptions of BEM theory is that spanwise flow along the length of the blade is neglected. But in reality the

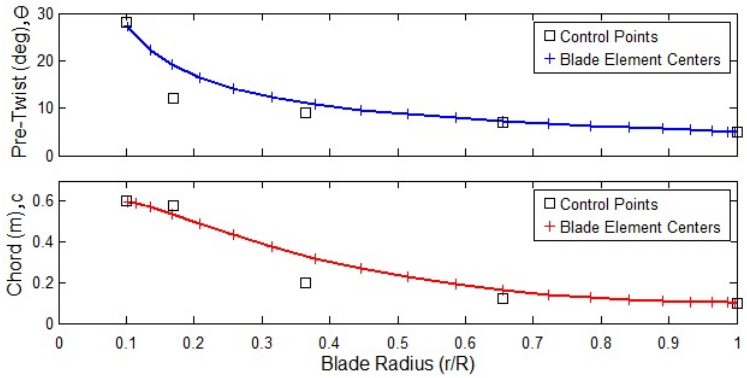


Figure 11.1.1: Chord and twist distribution determined by genetic algorithm

presence of spanwise flow can cause significant augmentation to the lift, drag, and pressure distributions, especially near the blade root. *HARP_Opt* can use the stall-delay models to make corrections to the lift and drag coefficients, accounting for spanwise flow. Since there are some approximations in the current implementation of the delay stall models, it is better to not consider this tool yet.

A general study of the software-parameters will be carried out in the following pages.

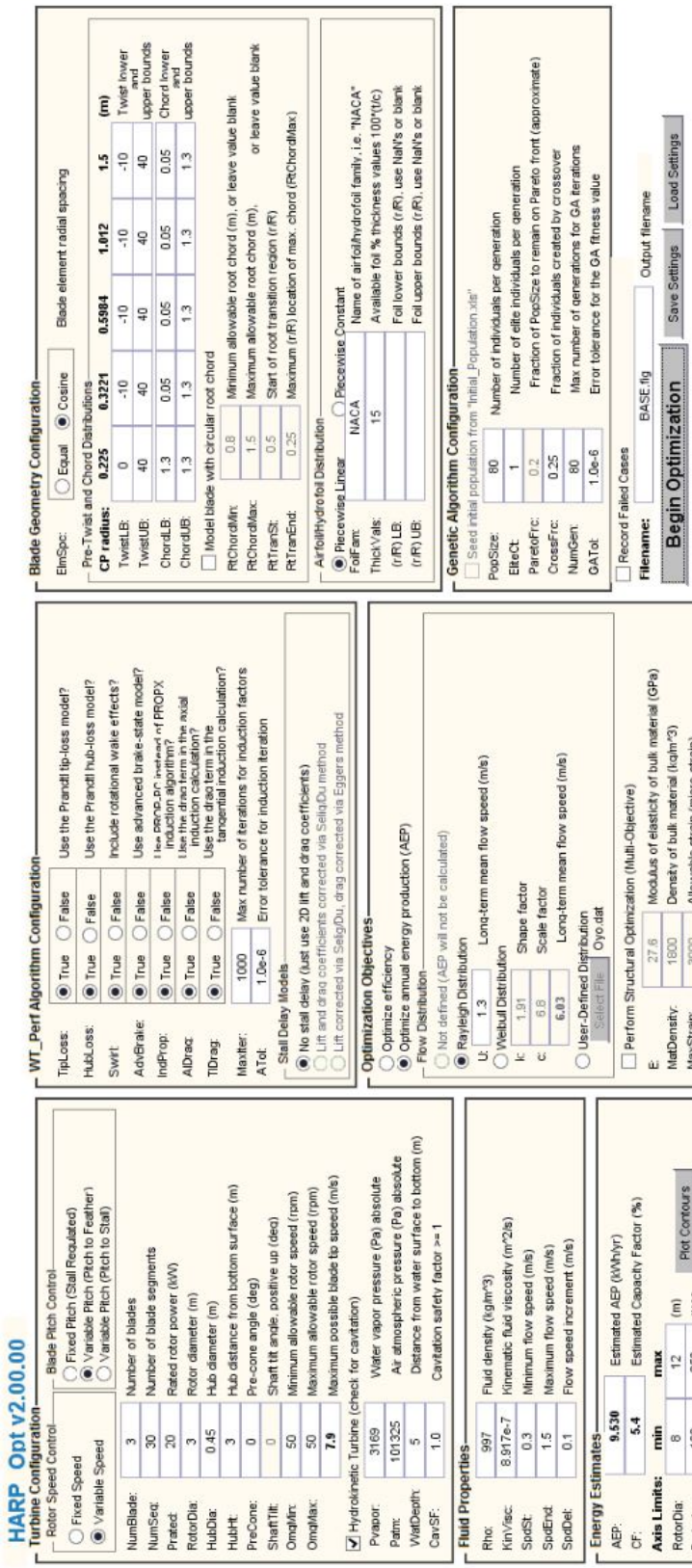


Figure 11.1.2: *HARP_Opt* grafic user interfece

### Parameters of Genetic Algorithm (GA)

The genetic optimization algorithm is controlled through 6 parameters, which are described in the original manual:

1. **PopSize**, which determines the number of individuals that will be created for each generation. Increasing the population size enables the genetic algorithm to more thoroughly search the solution space and thereby obtain a better result. However, the larger the population size, the longer the genetic algorithm takes to compute each generation.

2. **EliteCt**, which is the number of elite individuals in each generation. The elite count is the number of individuals with the best fitness values in the current generation that are guaranteed to survive to the next generation. When EliteCt is at least 1, the solution can only improve, or at least stay the same form one iteration to the next. However, setting a high value for EliteCt-can cause the fittest individuals to dominate the population, which can make the search less effective and may cause a pre-mature convergence. EliteCt is disabled during multi-objective optimization (when structural optimization is enabled), this is because the genetic algorithm handles elite individuals differently during multi-objective optimization.

3. **ParetoFrc** which is the number of individuals that are on the Pareto front. For example, if ParetoFrc is equal to 0.35, the solver will try to limit the number of individuals in the current population that are on the Pareto front to 35% of the population size.

4. **CrossFrc** which the crossover fraction of the population. This value specifies the fraction of the population, other than elite children, that is created by the crossover reproduction function. The remaining fraction of the population is created by the mutation reproduction function. Crossover and mutation are essential to the genetic algorithm optimization. Crossover enables the genetic algorithm to extract genes from the best performing individuals and recombine them into potentially superior children individuals. Mutation makes random changes to an individual, which adds diversity to the population and therefore searches the solution space more effectively. A crossover fraction of 1 means that all children will be crossover children, while a crossover fraction of 0 means that all children will be mutation children neither of these extremes is an effective optimization strategy.

5. **NumGen** which is a stopping criteria to determine the maximum number of generations that the genetic algorithm will run for. The genetic algorithm will terminate when NumGen has been reached, unless it converges before this number is reached. The genetic algorithm will also terminate if the number of stall-generations exceeds 50.A stall generation is a generation which has not made an improvement over the previous generation.

6. **GATol** which is the genetic algorithm tolerance. The optimization will converge when the average change in the fitness value, from one generation to the next, is less than the value specified by GATol.

One of the above mentioned quantities, ParetoFrc, has not been subsequently analysed because when enabling the variable speed simulation, the parameter in question is locked at a fixed value. To evaluate the behaviour of these factors, as previously mentioned, a set of variables comparable with the examples given by the producer has been defined, in order to create the starting model for further studies. The aim of this survey is to find a set of values that can guarantee a good compromise between precision and calculation time.

### Analysis of PopSize parameter

The figure 11.1.3 shows the AEP trend and the calculation time used in the simulation as a function of the PopSize parameter. The basic test that is often used for later comparisons, refers to a value of AEP equal to 9550 kw-hr/year with a simulation time of 23.5 minutes. Increasing PopSize, has the most influential effect on run-time performance.

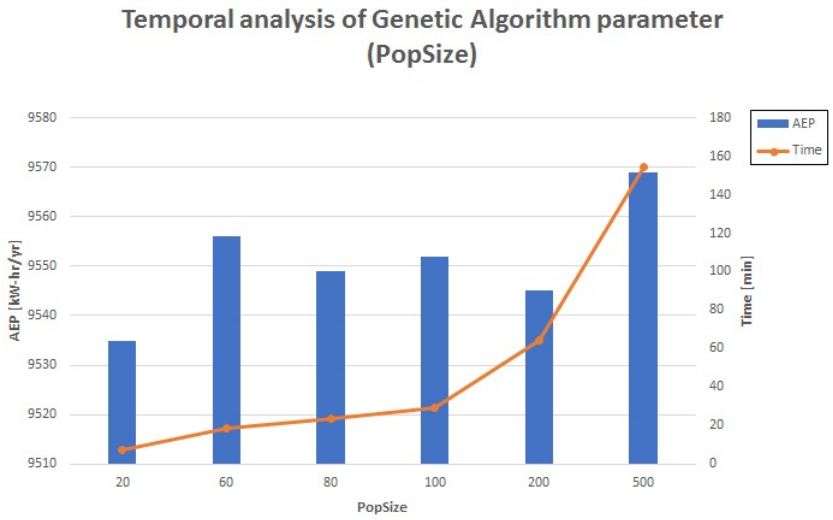


Figure 11.1.3: Temporal analysis of Genetic Algorithm parameter (PopSize)

By varying the parameter the Popsize number, as can be seen further in table 11.1, no significant differences were observed. For this reason, the value PopSize=80 has been chosen because it allows a good trade-off between precision and simulation time.

### Analysis of EliteCt parameter

As mentioned above, if large values are set for this parameter, this can lead to premature convergence. A greater demonstration of this was obtained by some warning messages in the simulation with EliteCt = 5.

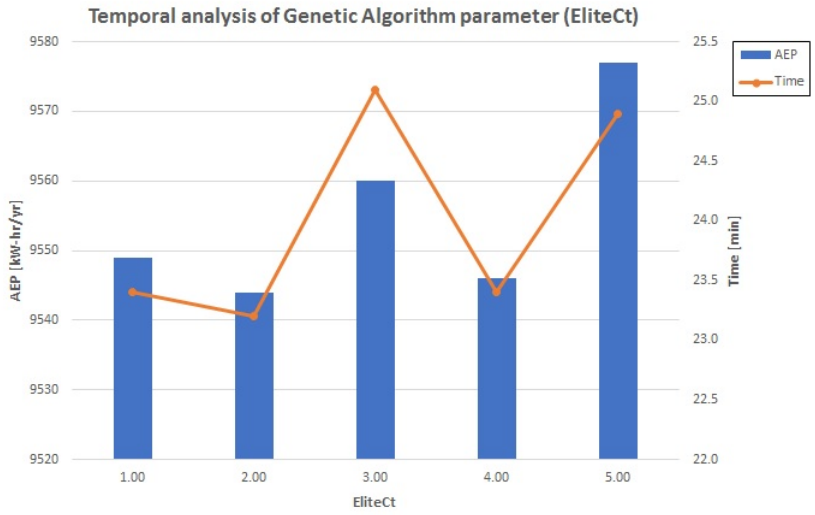


Figure 11.1.4: Temporal analysis of Genetic Algorithm parameter (EliteCt)

As you can see in figure 11.1.4, when the parameter under consideration changes, almost the same simulation time is used, so the chosen value has been evaluated in terms of AEP precision. For this reasons, the best choice falls into EliteCt = 1.

### Analysis of CrossFrc parameter

As previously mentioned, the CrossFrc values may vary between 0 and 1 (figure 11.1.5).

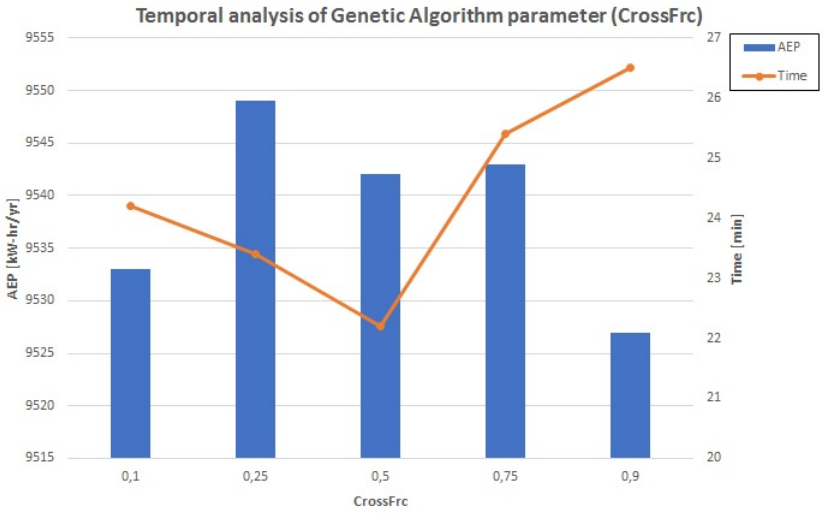


Figure 11.1.5: Temporal analysis of Genetic Algorithm parameter (CrossFrc)

In this case, there were almost no significant changes in the calculation time; for this reason the choice falls to CrossFrc = 0.25.

### Analysis of NumGen parameter

The run-time is almost scales linearly with NumGen (figure 11.1.6).

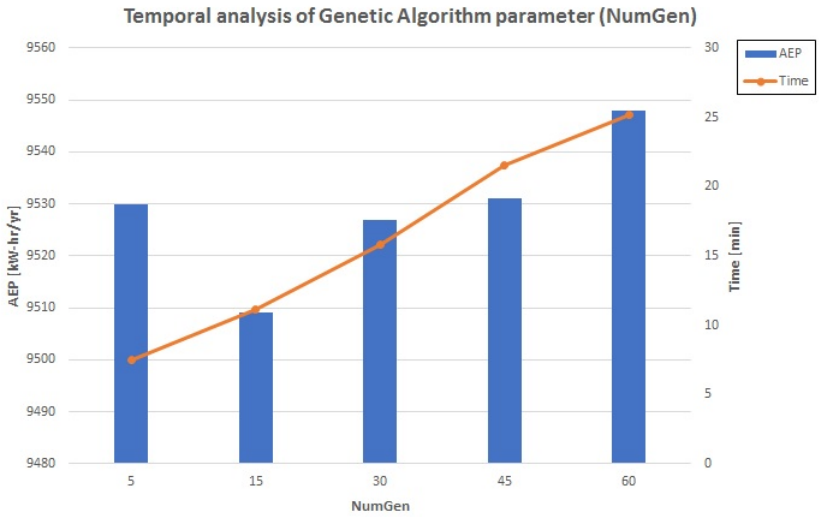


Figure 11.1.6: Temporal analysis of Genetic Algorithm parameter (NumGen)

Since the starting simulation corresponds to set NumGen = 60 with a certain GATol tolerance, refer to figure 11.1.2, it is not possible to simulate higher values of NumGen because that tolerance degree is achieved before reaching the generations end. For this reason, NumGen = 60 allows to have the best compromise between AEP and calculation time.

### Analysis of GATol parameter

In this case, compared to the starting case, figure 11.1.2, the value of GATol= 1e-7 is the optimal choice because it allows to obtain a better precision without increasing the calculation time (figure 11.1.7).

### Parameters of Blade Element Momentum theory (BEM)

The main configurable parameters of BEM algorithm are:

- **NumSeg** which indicates how many elements there will be along the blade. The analysis points are located at the center of the elements;
- **MaxIter** which shows the maximum number of iterations for induction factors;
- **ATol** which indicates the tolerance error for induction iteration;

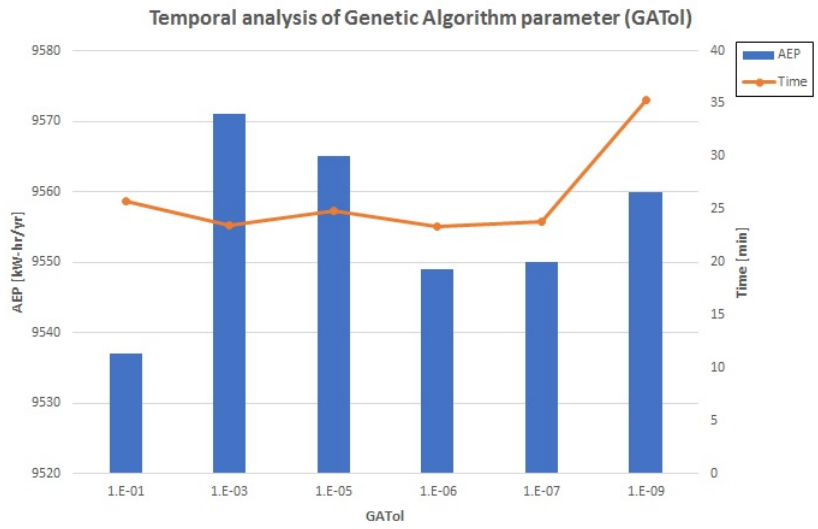


Figure 11.1.7: Temporal analysis of Genetic Algorithm parameter (GATol)

### Analysis of NumSeg parameter

As can be seen in figure 11.1.8, for small NumSeg values there is a low resolution of the blade which results in an overestimation of the actual values in terms of AEP. For this reason, the best compromise between AEP accuracy and calculation time is reached with the NumSeg = 30 configuration (figure 11.1.8).

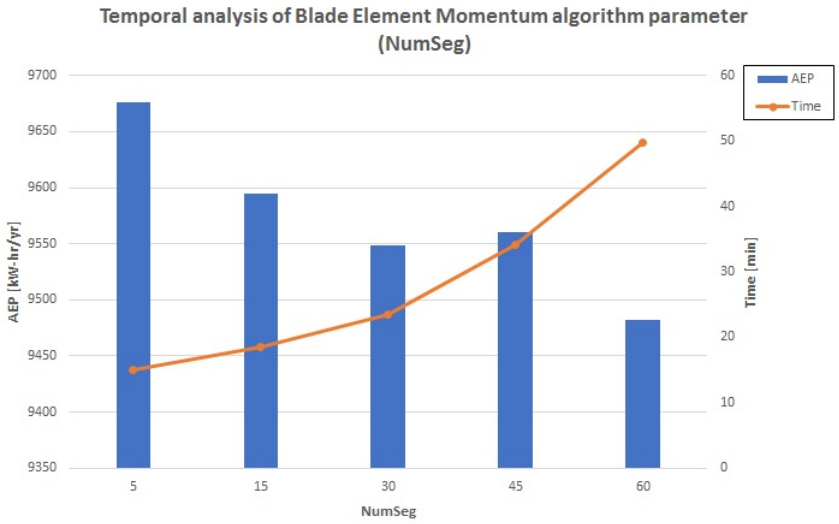


Figure 11.1.8: Temporal analysis of Blade Element Momentum algorithm parameter (NumSeg)

### Analysis of MaxIter parameter

This parameter shows an ambiguous trend which makes it difficult to evaluate. For this reason has been chosen the base value used in the starting test, MaxIter = 1000 (figure 11.1.9).

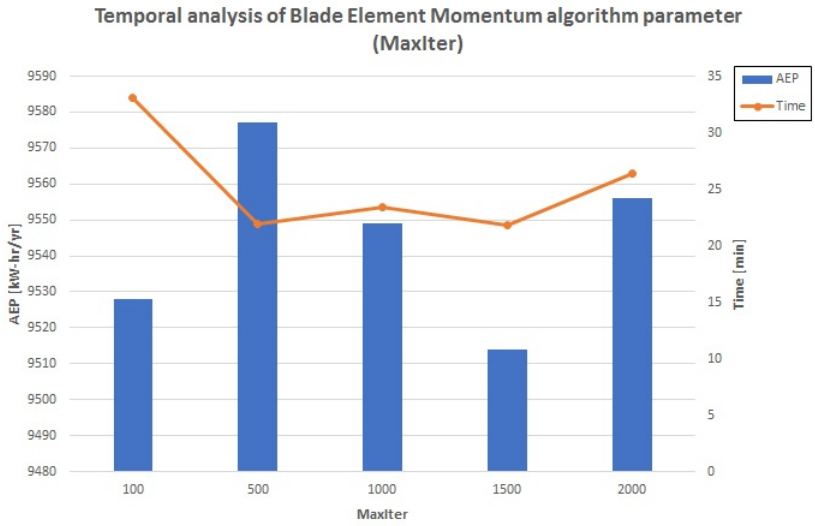


Figure 11.1.9: Temporal analysis of Blade Element Momentum algorithm parameter (MaxIter)

### Analysis of ATol parameter

Also in this case, as observed in figure 11.1.10, if a large tolerance is entered, the AEP value is overestimated. For this reason, the best compromise between AEP accuracy and calculation time is reached with the ATol = 1e-5 configuration.

To understand the data distribution, some statistical values have also been calculated in table 11.1, such as the standard deviation (SD) and the coefficient of variance (COV).

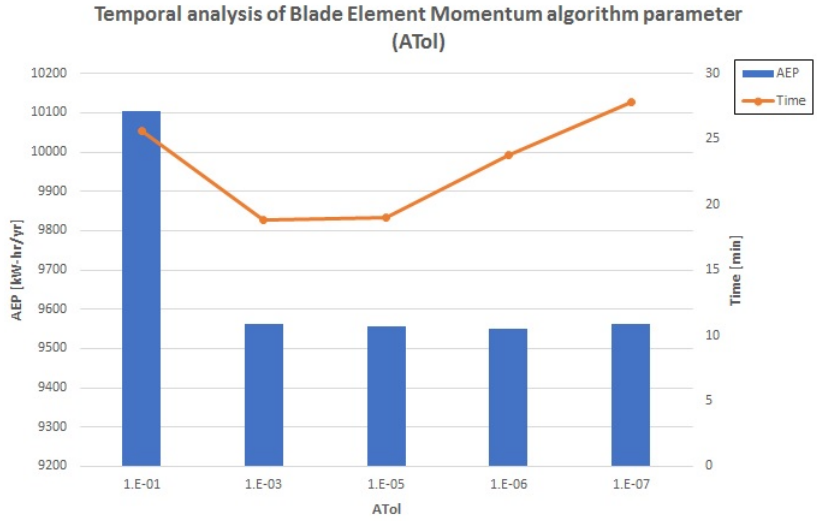


Figure 11.1.10: Temporal analysis of Blade Element Momentum algorithm parameter (ATol)

| **Genetic Algorithm parameters** | **Standard deviation (SD)** | **Coefficient of variance (COV)** |
|---|---|---|
| PopSize | 11.37 | 0.001 |
| EliteCt | 13.67 | 0.001 |
| CrossFrc | 8.73 | 0.001 |
| NumGen | 13.87 | 0.001 |
| GATol | 12.37 | 0.001 |
| **BEM algorithm parameters** | **-** | **-** |
| ATol | 244.34 | 0.026 |
| MaxIter | 24.55 | 0.003 |
| NumSeq | 70.92 | 0.007 |

Table 11.1: Statistic table of algorithm parameters

| **Geometrical Dimensions** | | |
|---|---|---|
| NumBlade: | 3 | |
| NumSeq: | 30 | |
| RotorDia: | 3 | m |
| HubDia: | 0.45 | m |
| HubHt: | 3 | m |
| **Fluid Properties** | | |
| $\rho$: | 997 | $kg/m^3$ |
| KinVisc: | 9.917e-7 | $m^2/s$ |
| Pvapor: | 3169 | Pa |
| Patm: | 101325 | Pa |
| CavSF: | 1 | |
| **Installation site** | | |
| WatDepth: | 5 | m |
| SpdSt: | 0.3 | m/s |
| SpdEnd: | 1.5 | m/s |
| Rayleigh Distribution: $U_{mean}$ | 1.3 | m/s |
| SpdDel: | 0.1 | m/s |
| **Terms of use** | | |
| Prated : | 20 | kW |
| OmgMin: | 50 | rpm |
| OmgMax: | 50 | rpm |
| **BEM Analysis** | | |
| ATol: | 1.0e-6 | |
| MaxIter: | 1000 | |
| **Genetic Algorithm Configuration** | | |
| PopSize: | 80 | |
| EliteCt: | 1 | |
| CrossFrc: | 0.25 | |
| NumGen: | 60 | |
| GATol : | 1.0e-6 | |

Table 11.2: Set of parameters in *Harp_Opt* starting test

In conclusion, the parameters collected during the study are summarized in table 11.3.

| | | |
|---|---|---|
| **Geometrical Dimensions** | | |
| NumBlade: | 3 | |
| NumSeq: | 30 | |
| RotorDia: | 3 | m |
| HubDia: | 0.45 | m |
| HubHt: | 3 | m |
| **Fluid Properties** | | |
| $\rho$: | 997 | $kg/m^3$ |
| KinVisc: | 9.917e-7 | $m^2/s$ |
| Pvapor: | 3169 | Pa |
| Patm: | 101325 | Pa |
| CavSF: | 1 | |
| **Installation site** | | |
| WatDepth: | 5 | m |
| SpdSt: | 0.3 | m/s |
| SpdEnd: | 1.5 | m/s |
| Rayleigh Distribution: $U_{mean}$ | 1.3 | m/s |
| SpdDel: | 0.1 | m/s |
| **Terms of use** | | |
| Prated : | 20 | kW |
| OmgMin: | 50 | rpm |
| OmgMax: | 50 | rpm |
| **BEM Analysis** | | |
| ATol: | 1.0e-5 | |
| MaxIter: | 1000 | |
| **Genetic Algorithm Configuration** | | |
| PopSize: | 80 | |
| EliteCt: | 1 | |
| CrossFrc: | 0.25 | |
| NumGen: | 60 | |
| GATol : | 1.0e-7 | |

Table 11.3: Set of algorithm parameters

### 11.1.2 Choice of Hydrofoils

*HARP_Opt* accepts files formatted to the existing *AeroDyn v12* style or the newer, slightly modified style for the airfoil/hydrofoil data input files.
It is not the intent of *HARP_Opt* to provide an extensive database of airfoils and hydrofoils the airfoil/hydrofoil database is designed to be easily expanded by the user.

To simplify the study, profiles already available in the database have been chosen. $C_L$ and $C_D$ data refer to Reynolds numbers between 1.5 and 2 million
Each series of hydrofoils was studied in such a way as to be able to choose the most appropriate for our study, then the best of each series were compared and then we proceeded to the comparison of 3 types of hydrofoil.
The comparisons of $C_L$, $C_D$ and $C_L/C_D$ of the hydrofoils of each series are shown in figures 11.1.11, 11.1.12, 11.1.13,11.1.14 and 11.1.15.

The main focus in the design of blade sections of lift turbines, has been to maximize lift: drag ratio (L/D) mainly by increasing $C_L$. It is still a generally accepted requirement. However, there are different preferences among blade aerodynamicists regarding the maximum $C_L$ depending on the type of control, for example, the stall controlled turbines restrict $C_{L,max}$ to serve two purposes: (i) to reduce the peak power generated; and (ii) to keep the thrust on the system small. On the other hand, the pitch-controlled turbines require a high $C_{L,max}$.
A high lift to drag ratio is a generally accepted requirement; however, although a reduction in the drag coefficient directly contributes to a higher aerodynamic efficiency, an increase in the lift coefficient does not have a significant contribution to the torque, as it is only a small component of lift that increases the tangential force while the larger component increases the thrust [73].
For the choice of hydrofoils the considerations made previously have been taken into account and a compromise has been looked for, attempting to have a good stall characteristic. Hydrofoils selected for the study are:

- NACA 4415;
- FFA-W3-211;
- RISO 18;

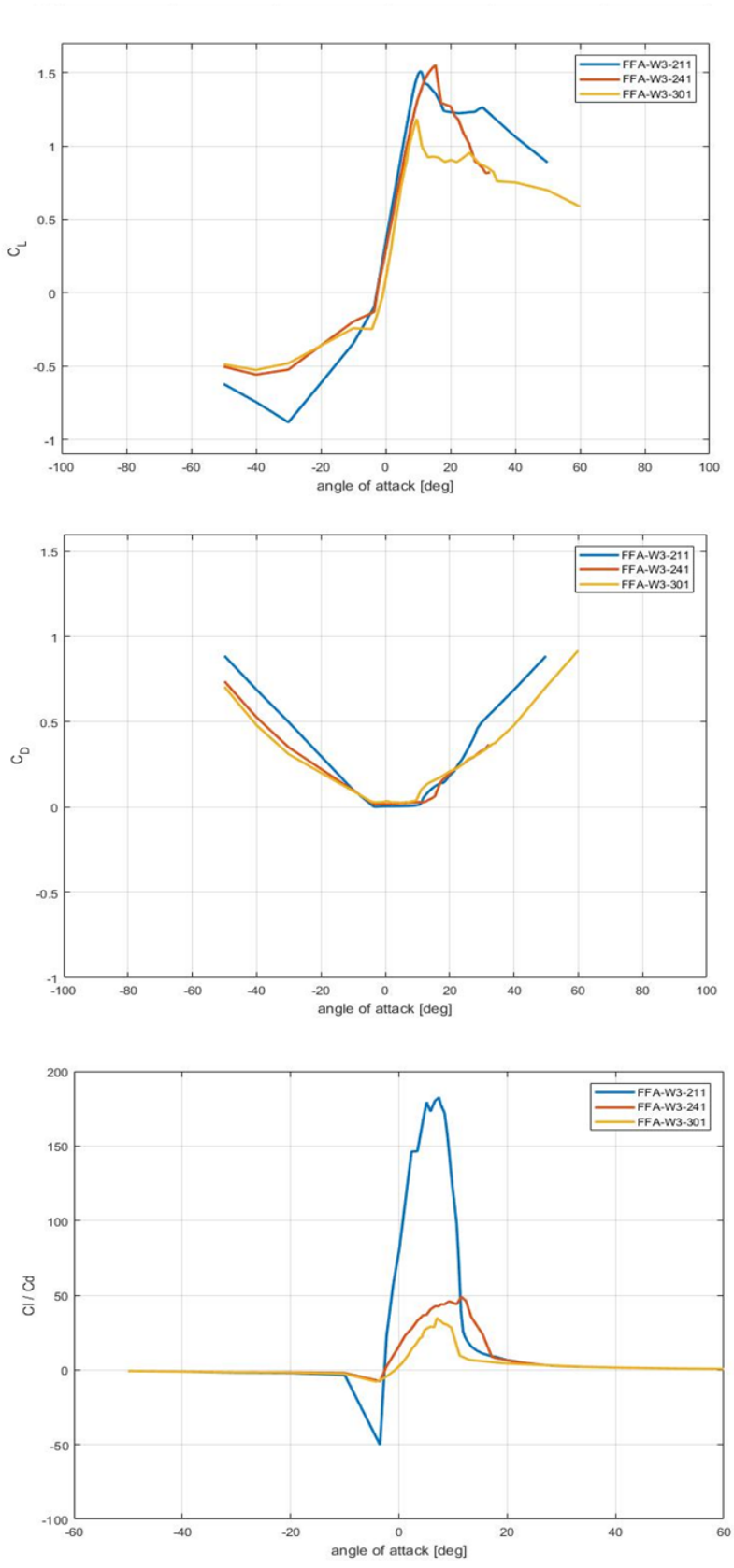


Figure 11.1.11: FFA hydrofoils comparison

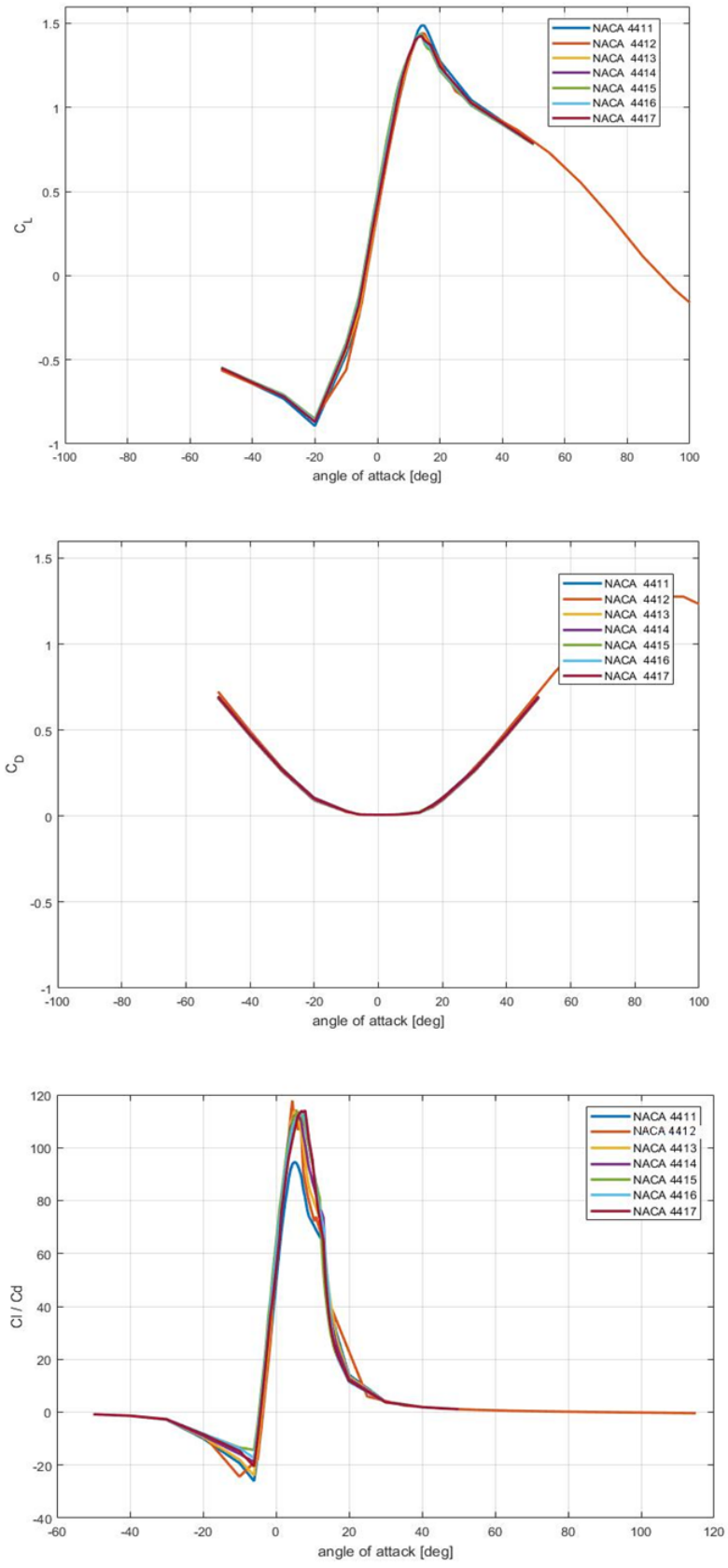


Figure 11.1.12: NACA hydrofoils comparison

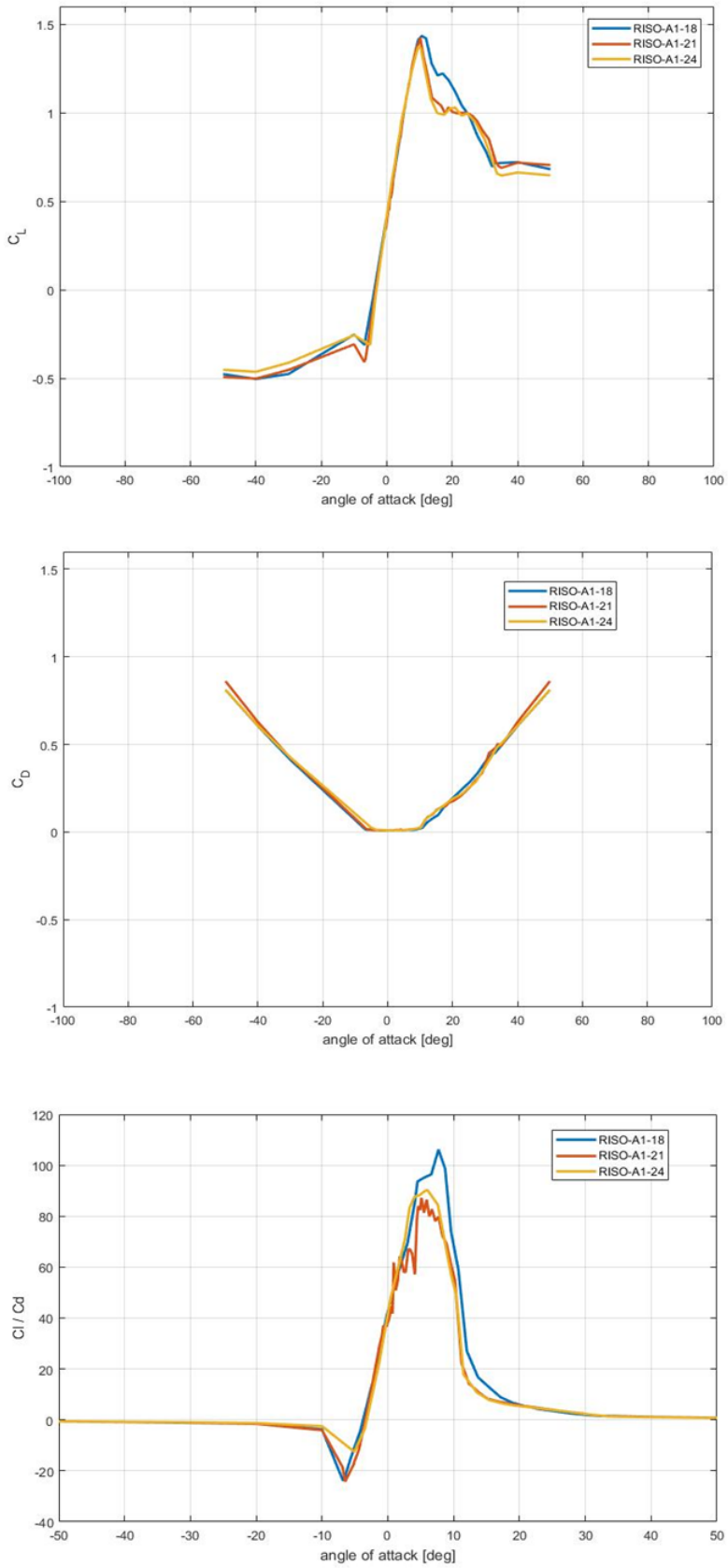


Figure 11.1.13: RISO hydrofoils comparison

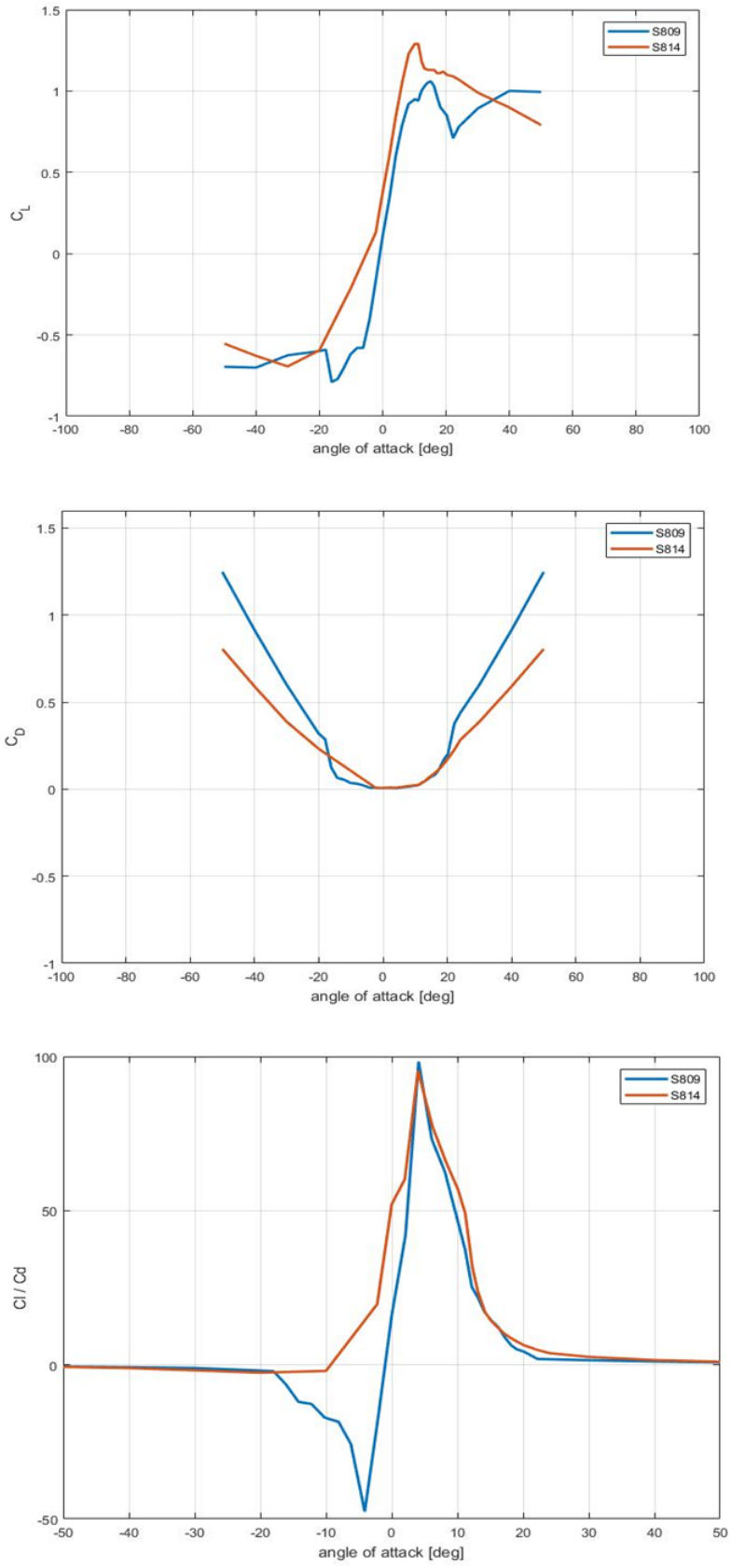


Figure 11.1.14: S series (NREL) hydrofoils comparison

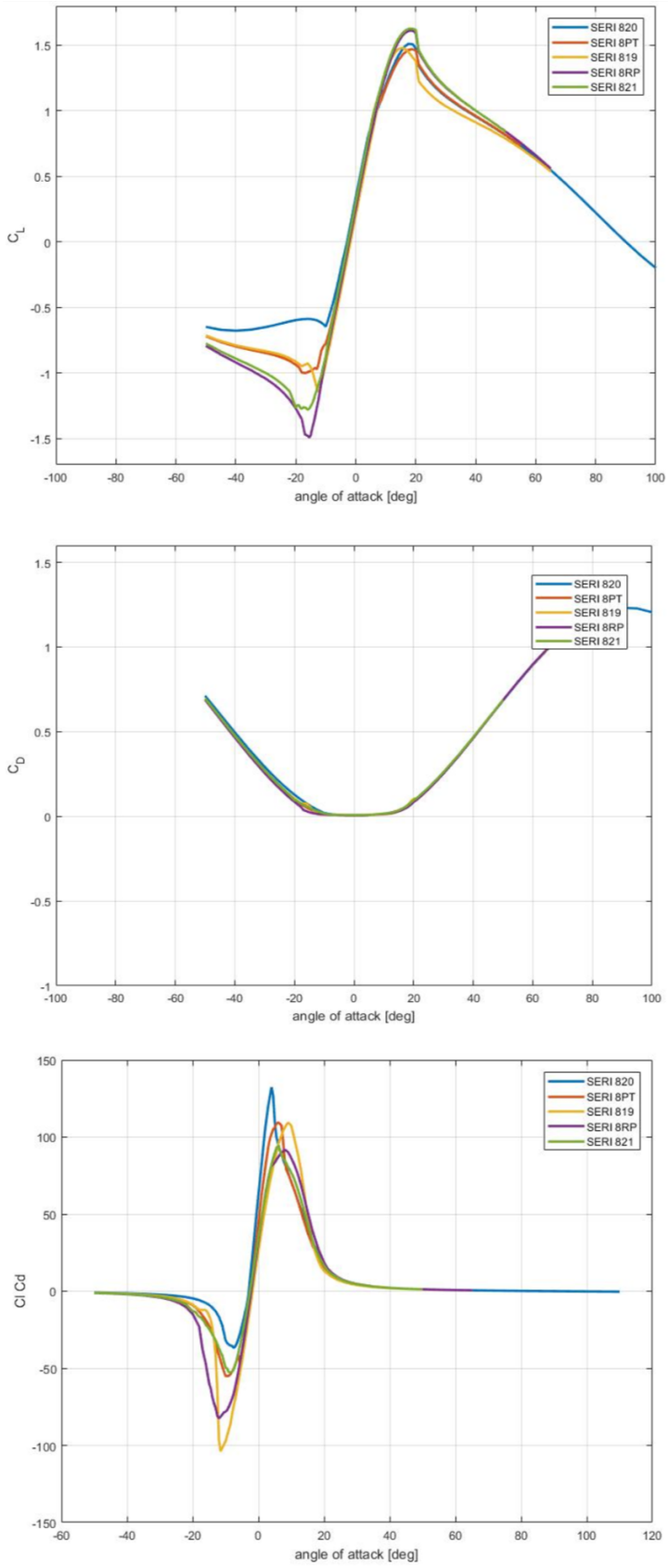


Figure 11.1.15: SERI hydrofoils comparison

### 11.1.3 Water speed distribution

In order to realise a survey focused on the optimisation of the annual energy produced (AEP), the *HARP_Opt* software offers the possibility to use an optimisation algorithm based on a customized flow probability distribution. First of all, with the purpose of a statistical analysis, all data of the Alima river speeds in Tchicapika station from 1952 to 1993 have been analyzed. Once the cumulative distribution function (CDF) of the achieved data was represented, some possible fitting were evaluated with different types of static distribution.

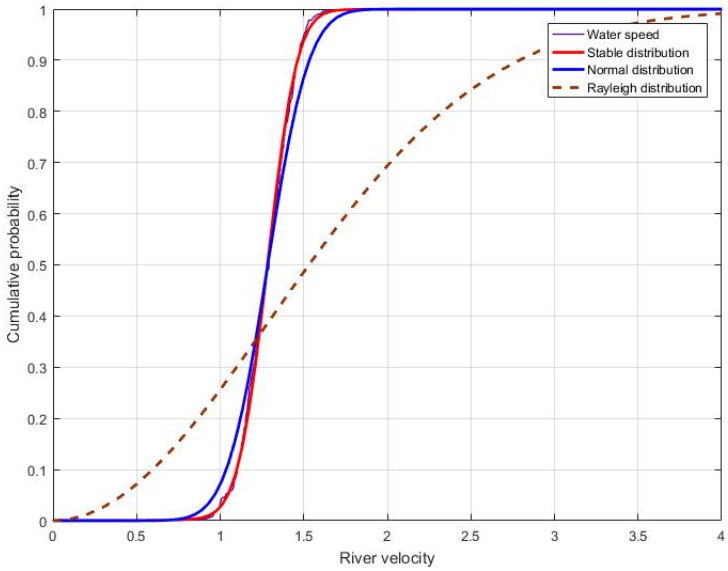


Figure 11.1.16: Cumulative distribution function

While normal distribution is not too far from the original CDF, the best performance was achieved with stable distribution. Stable distribution, also named Lévy distribution, in honour of its inventor,Paul Lévy, is one of the few distributions that are stable and that have probability density functions (PDF) that are analytically expressible. The others are the normal distribution and the Cauchy distribution [74].
The Lévy distribution is sometimes used in financial engineering to model price changes because the 'fat tail' or slow fall off that this distribution models, is a good match for what happens after prices change. Other applications concern social engineering and physical sciences, such as how to determine the length path follows by photon in a turbid medium [75].
As the stable distribution was chosen from figure 11.1.16 as the function that best approximates all of the data, for further clarity, the probability density function (PDF) was also evaluated .

In conclusion, the probability density data of the stable distribution were exported and set in *HARP_Opt* for further studies.

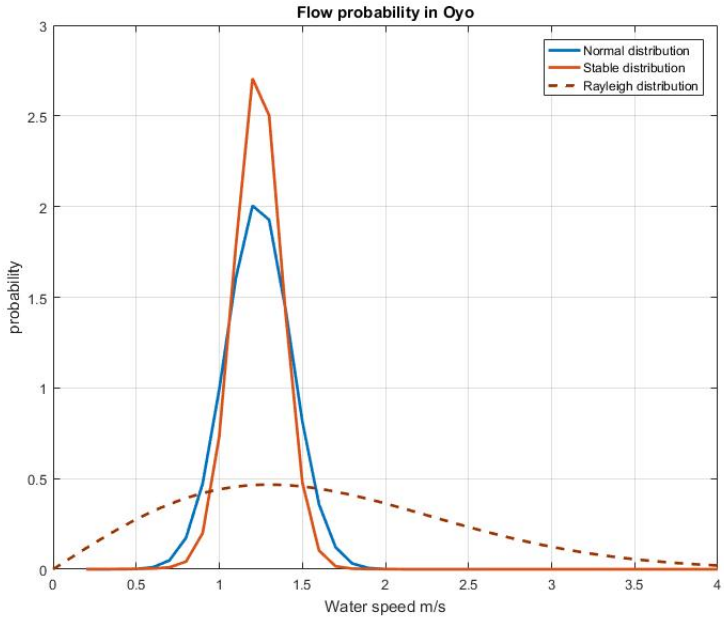


Figure 11.1.17: Probability distribution function(PDF)

### 11.1.4 Height of turbine installation

Since there is not an optimal choice on the type of installation of horizontal axis turbines, both submerged and near the free surface, it is advisable to make some tests in accordance with the required application. In this case, to simplify the study, only one type of rotor was studied, i.e. the 3-metre diameter configuration with NACA 4415 profile. Two simulation was made respectively at 2 and 3 meters above the bottom of the river, setting a variable rotor speed range. The factors taken into account for the comparison concern the power curves, the rotor speed range and the annual energy production (AEP). The results of the study did not show any noticeable differences between the two models, which suggests some considerations made. In particular, when the speed distribution was calculated, a hypothesis of a constant section of the river was introduced. In addition, as the speed study was set up, a speed profile along the depth of the river, i.e. along the axis of the third dimension z, was not taken into account. For these reasons, and also considering the importance of river navigability, it was decided to use a submerged system with a constant installation height for each test of 3 meters above the bottom of the river.

### 11.1.5 Rotor speed control

In the *HARP_Opt* code two types of configurations can be used for the rotor rotational speed, fixed or variable speed. In the fixed speed configuration, once a range of angular speed variability has been introduced, the software proceeds to evaluate a speed value that can guarantee the best performance over the entire turbine operating range. On the other hand, in the variable speed type, for each river speed the software chooses the optimal rotation speed in order to maximize the energy

production. This powerful tool will be used in the next analysis, case by case.

## 11.2 Hydrofoils comparison in *HARP_Opt*

In this section are presented several tests in order to highlight the differences of the hydrofoils previously chosen (NACA 4415, FFA-W3-211, RISO-A1-18) in three different sizes of diameter, 3 metres, 2 metres and 1.5 metres. The aim of this analysis is to determine, for each selected diameter, which is the best turbine in terms of performance and annual energy production (AEP). For this purpose, the first step was to carry out an assessment to identify some of the effects that may affect the behaviour of turbines, such as the installation depth and the range of angular rotational speeds.

### 11.2.1 Test for a 3 meters rotor turbine diameter

In this first study, by setting the fixed speed configuration, the optimal speeds for each profile were evaluated with the aim to obtain a unique angular velocity. The optimal speeds obtained fall within a very limited range, between 35 and 40 rpm. However, if a number of fixed speed tests are carried out just outside this range, the program can not find solutions in acceptable time. For this reason, the following simulations conducted at fixed speed will be considered as the optimal speeds derived from the software. In addition in this section, only for the NACA 4415 profile, are also shown some of the parameters that the *HARP_Opt* code evaluate, as an illustration of the potentialities of this tool. The simulations conducted for each profile, with optimal fixed speed and variable speed, are compared below.

#### NACA 4415

As can be seen from figure 11.2.1 and figure 11.2.2, at low speeds, the two characteristic curves are almost overlapped, while at high speeds, the variable speed configuration predominates. This is partly due to the fact that the software tries to optimize the production of AEP where there are probability values in the speed distribution. In this way, when the fixed speed configuration is set, the algorithm searches for the optimal speed in the range where the probability density is different from zero, i.e. only at low speeds. For this reason, the rotation speed extracted from the code is not suitable for high speed flow because it acts as a resistance decelerating the river flow.

The figure 11.2.3 shows the trend of the power coefficient $C_P$ in the fixed speed configuration. With the variable speed configuration, figure 11.2.4, the algorithm adjusts the angular velocity according to the current speed, in order to maximize the power coefficient, which in this case is stable at 0.443.

Figure 11.2.5 and figure 11.2.6 show as the geometric parameters of the blade are altered moving in the radius direction.

Figure 11.2.7 and figure 11.2.8 show the thrust and the torque curves on the rotor. As noted above, in the variable speed configuration it can be seen that the rotor at high speeds is subject to higher loads.

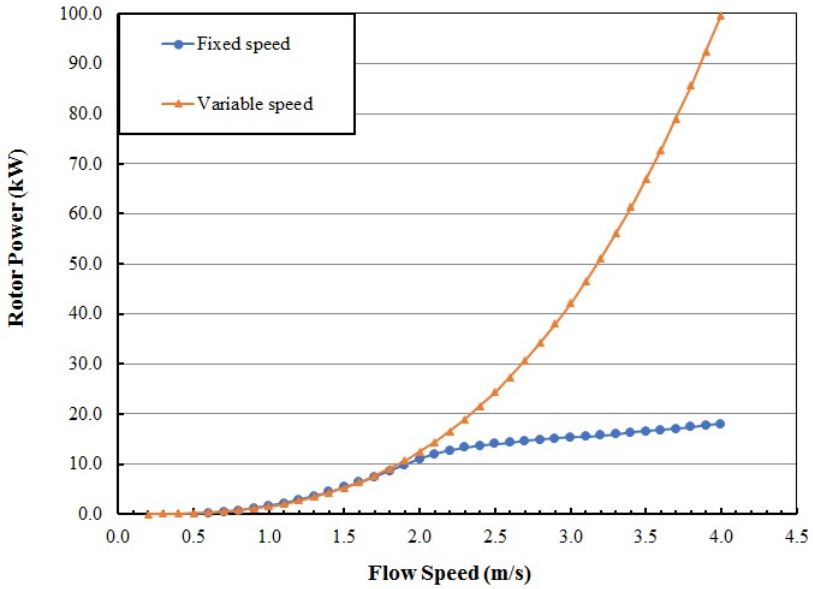


Figure 11.2.1: Power curves fixed/variable speed of NACA 4415

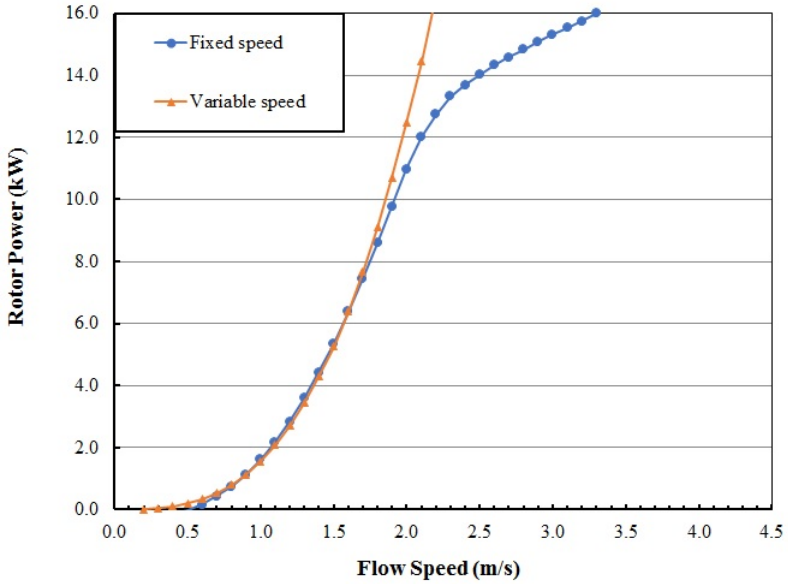


Figure 11.2.2: Power curves details at low water velocity

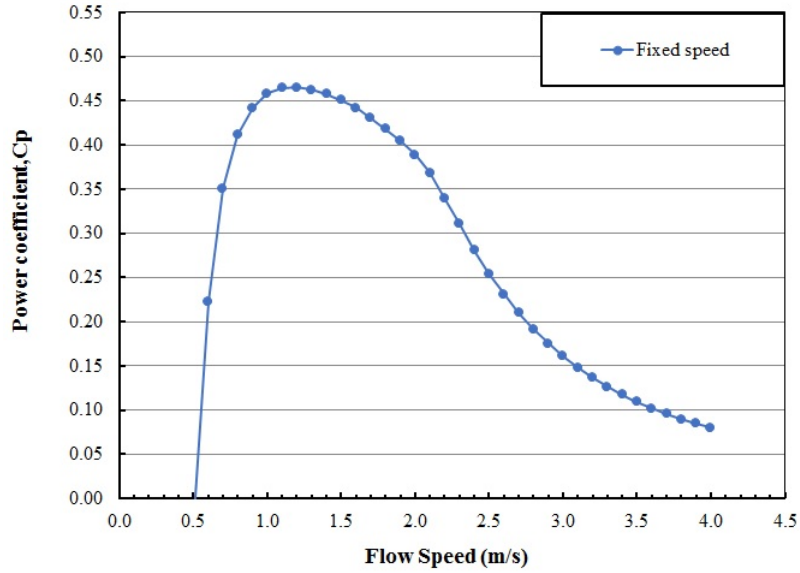


Figure 11.2.3: Power coefficient of NACA 4415 fixed speed

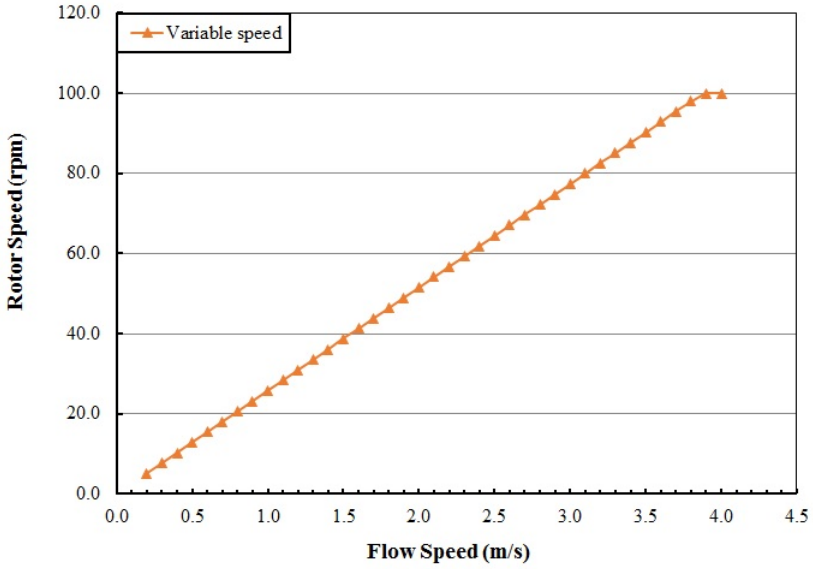


Figure 11.2.4: Angular rotor speed of NACA 4415

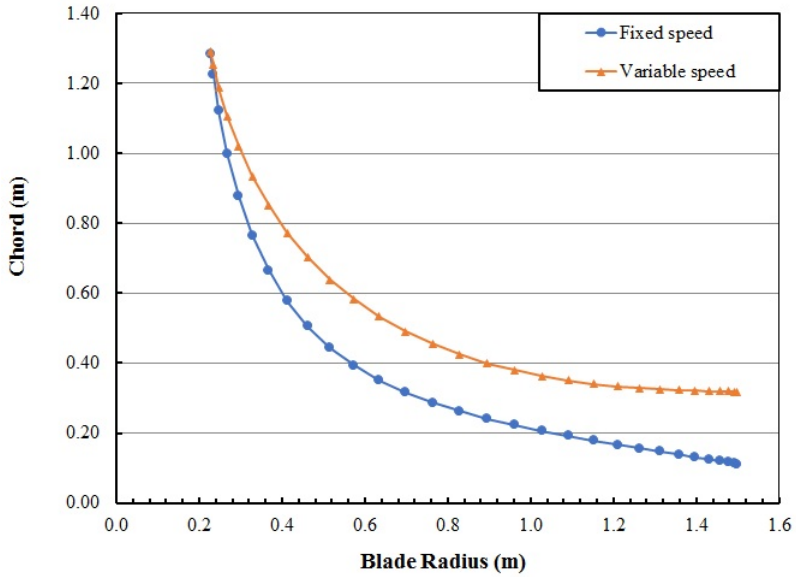


Figure 11.2.5: Chord distribution fixed/variable speed of NACA 4415

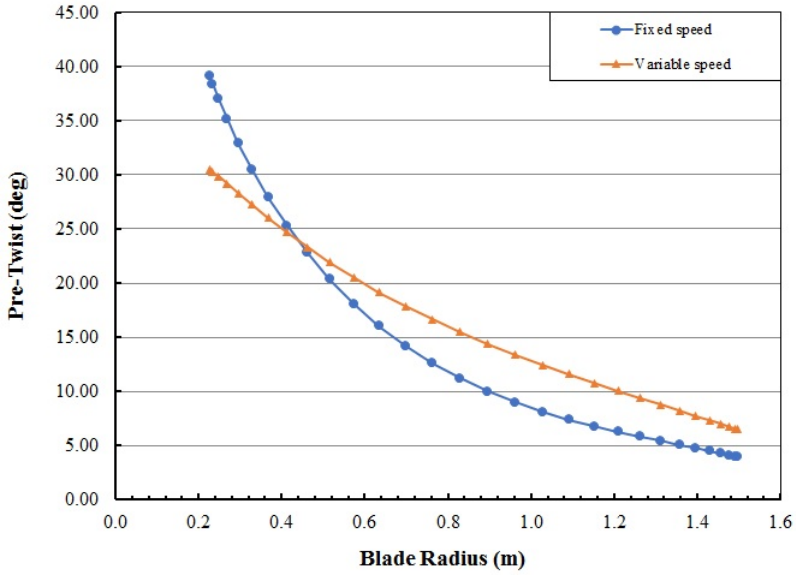


Figure 11.2.6: Twisted configuration fixed/variable speed of NACA 4415

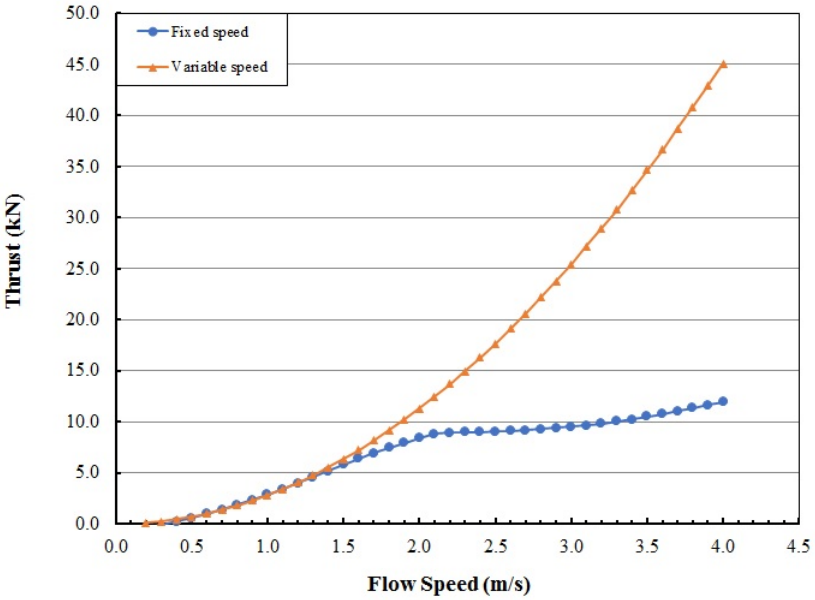


Figure 11.2.7: Thrust fixed/variable speed of NACA 4415

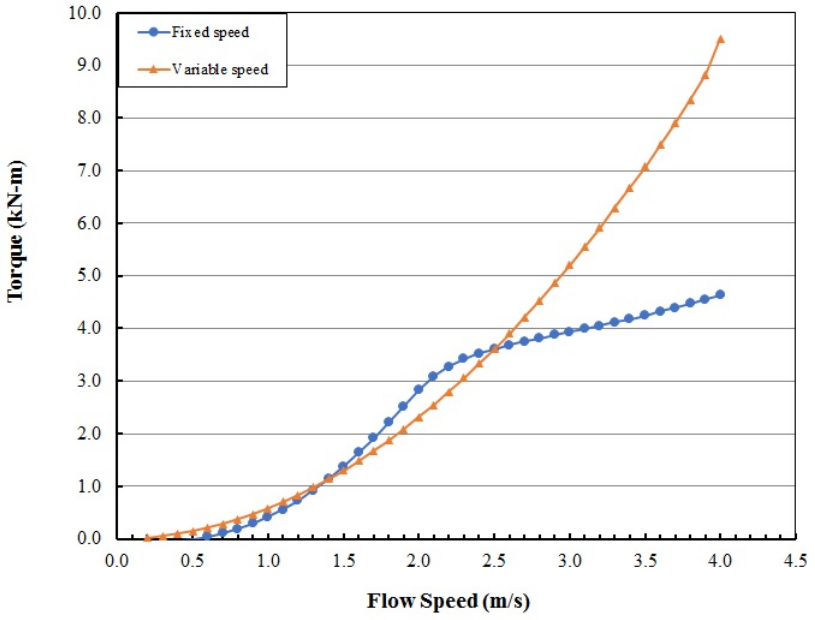


Figure 11.2.8: Torque fixed/variable speed of NACA 4415

### FFA-W3-211

In the same way as for the previous hydrofoil, the two curves at low speed have no differences, while at high current velocities the variable speed configuration prevails, figure 11.2.9.

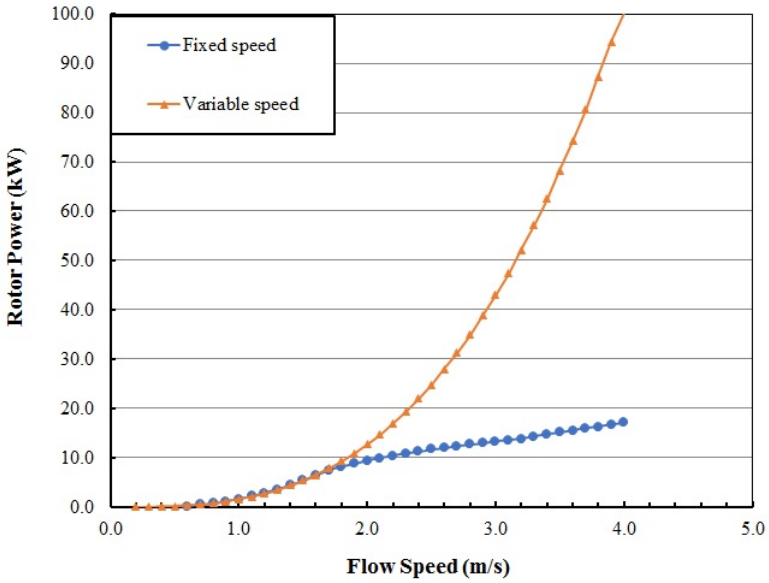


Figure 11.2.9: Power curves fixed/variable speed of FFA-W3-211

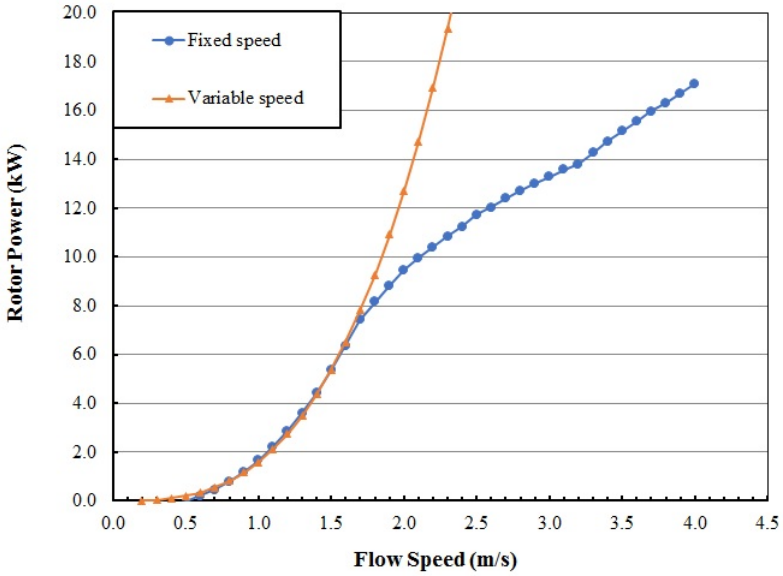


Figure 11.2.10: Power curves details at low water velocity

Figure 11.2.11 shows the trend of the power coefficient at fixed speed with the current speed variations.

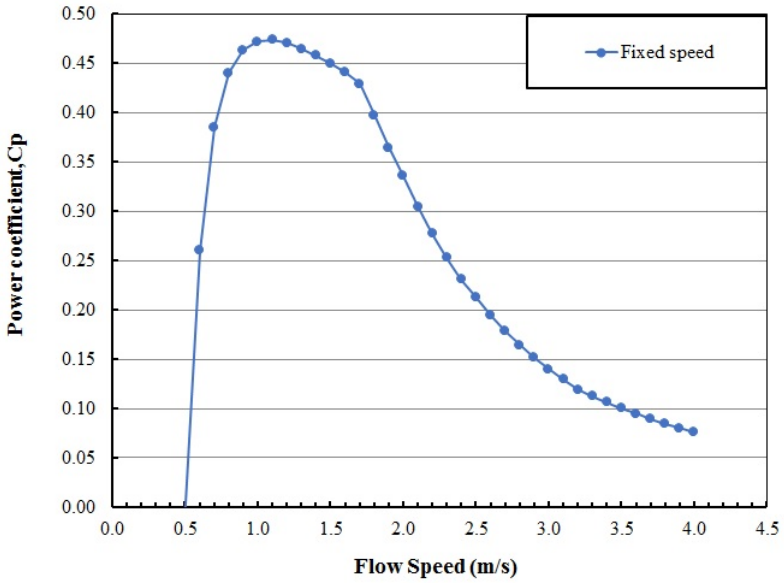


Figure 11.2.11: Power coefficient of FFA-W3-211 fixed speed

### RISO 18

As can be seen in figure 11.2.12 and figure 11.2.13, the same considerations as for the previous hydrofoils are also valid in this case, where significant differences can be noted only at high current speeds.

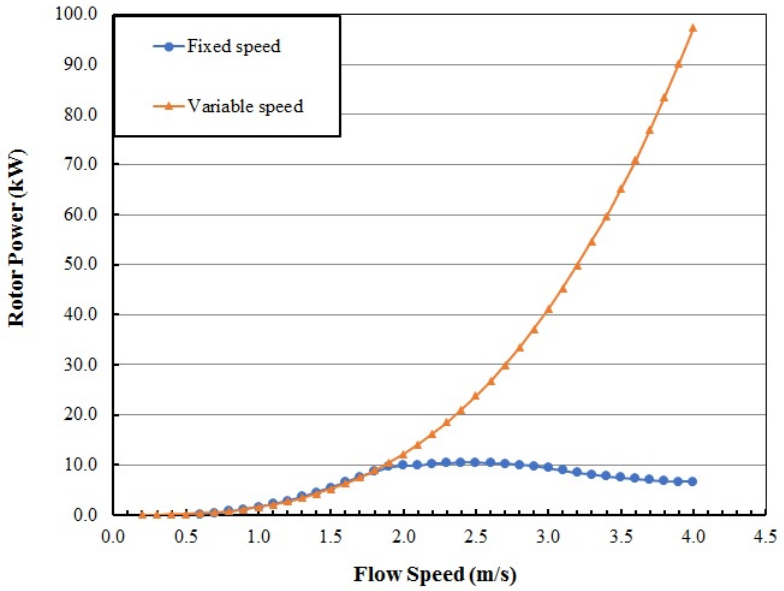


Figure 11.2.12: Power curves fixed/variable speed of RISO 18

Figure 11.2.14 shows the trend of the power coefficient at fixed speed with the current speed variations.

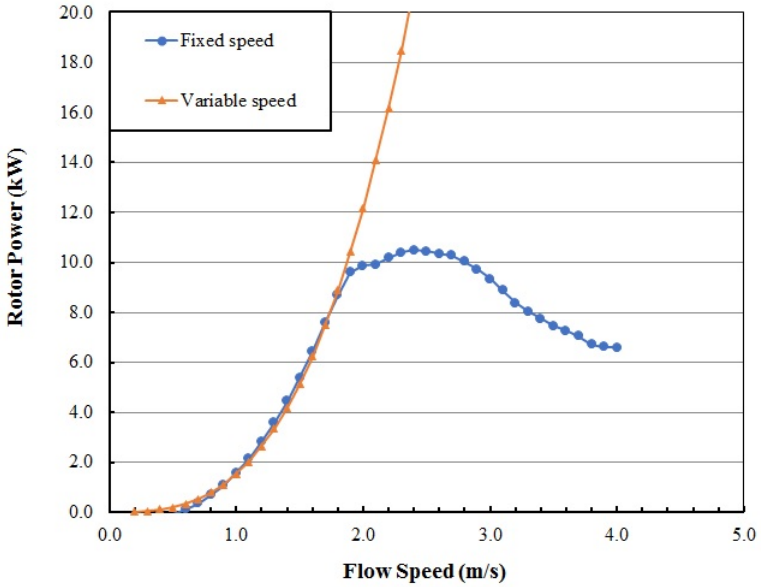


Figure 11.2.13: Power curves details at low water velocity

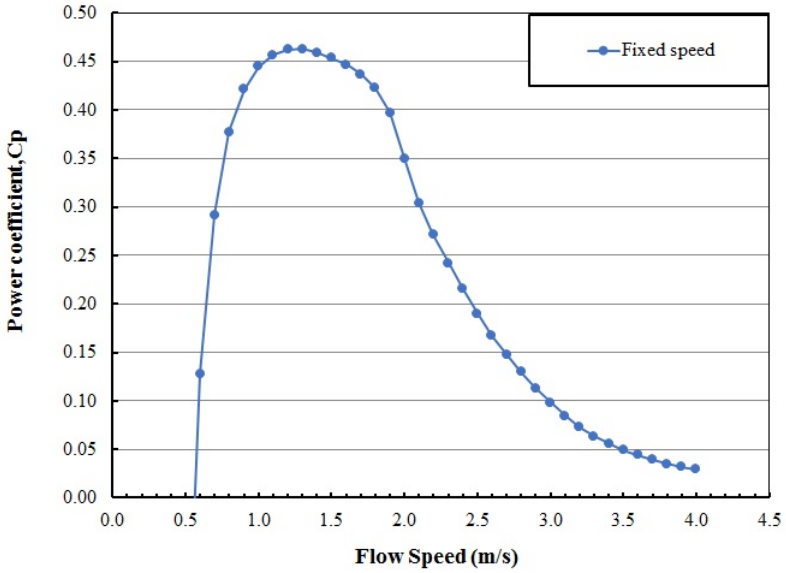


Figure 11.2.14: Power coefficient of RISO 18 fixed speed

### Comparison

To evaluate the best profile, since there are no differences in the variable speed power curves, figure 11.2.17, only the parameters obtained in the fixed speed configuration were evaluated. As can be seen from figure 11.2.15, whereas at low current speeds there are no differences, at high speeds the NACA profile prevails over the competitors. However, taking into account the trends of the power coefficients $C_P$,

figure 11.2.16, and the data of the capacity factor CF and AEP summarized in table 11.4 and table 11.6, due to the speed distribution used, the best choice is the FFA-W3-211 profile. Capacity factor CF values may also vary considerably between the different profiles, as they refer to a rated power of 2 m/s of velocity.

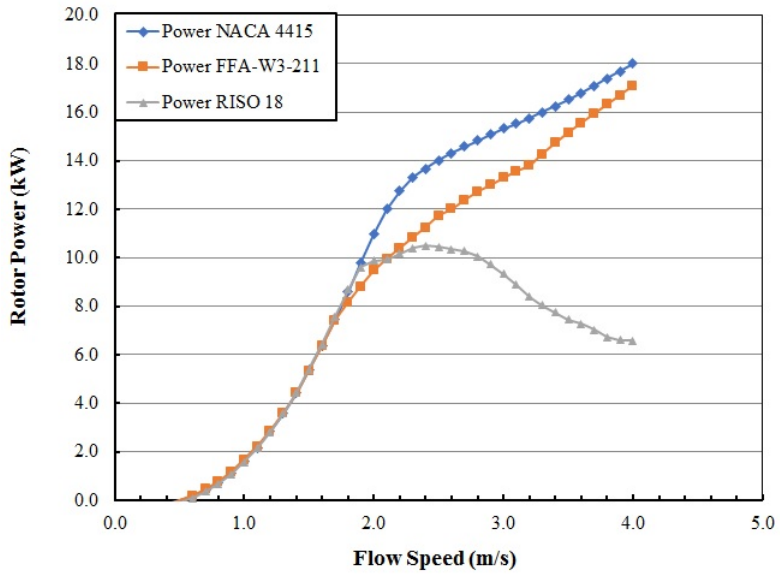


Figure 11.2.15: Power curves comparison at 3 m of diameter at fixed speed

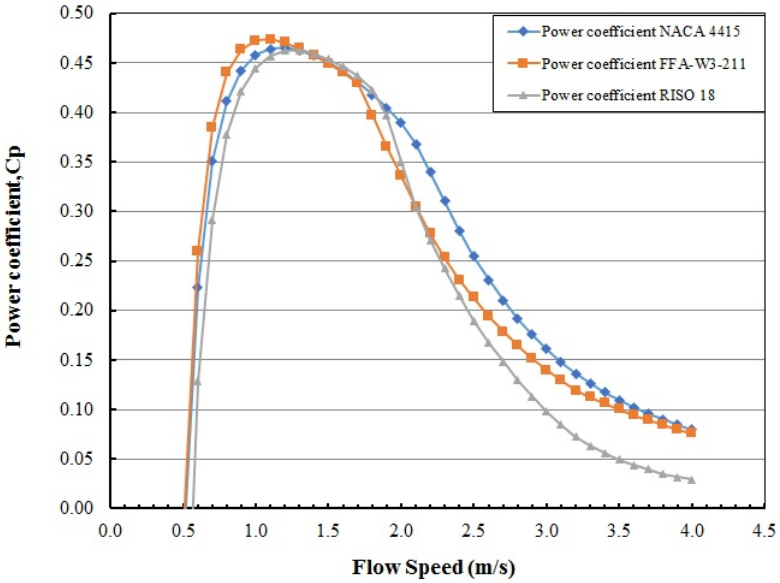


Figure 11.2.16: Power coefficient comparison at 3 m of diameter at fixed speed

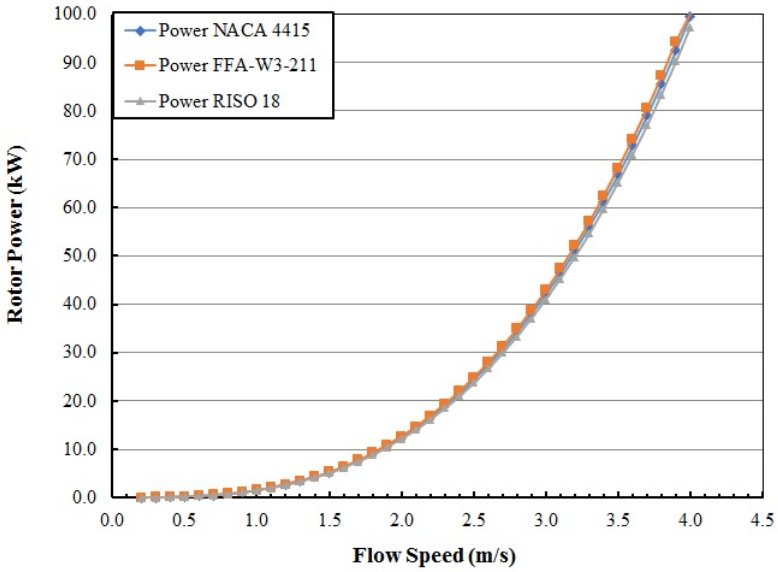


Figure 11.2.17: Power curves comparison at 3 m of diameter at variable speed

### 11.2.2 Test for a 2 meters rotor turbine diameter

Since many of the graphs previously seen have the same trends and characteristics also in the subsequent categories, in order to reduce the treatment complexity, only the comparisons between the hydrofoils in the remaining categories will be examined.
As can be seen in figure 11.2.18 and figure 11.2.20, there are only slight variations between these profiles, so overall the model FFA-W3-211 was selected. In figure 11.2.19 it is shown that the power coefficient $C_P$ of the profile FFA-W3-211 is preferable among the competitors. Although table 11.4 shows a higher CF value for RISO 18, as it does not represent an absolute value but an index that also depends on the rated power evaluated at an arbitrary speed, in this case observing the AEP value in table 11.6, the choice is the profile FFA-W3-211.

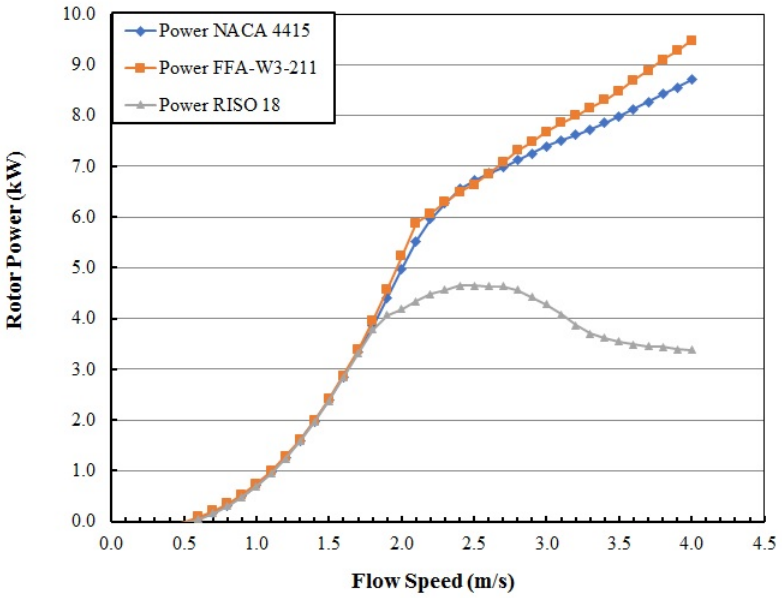


Figure 11.2.18: Power curves comparison at 2 m of diameter at fixed speed

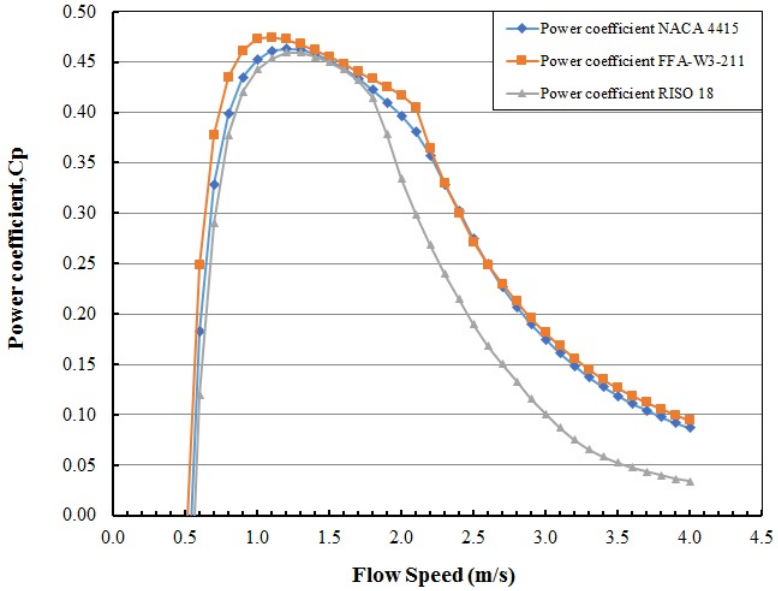


Figure 11.2.19: Power coefficient comparison at 2 m of diameter at fixed speed

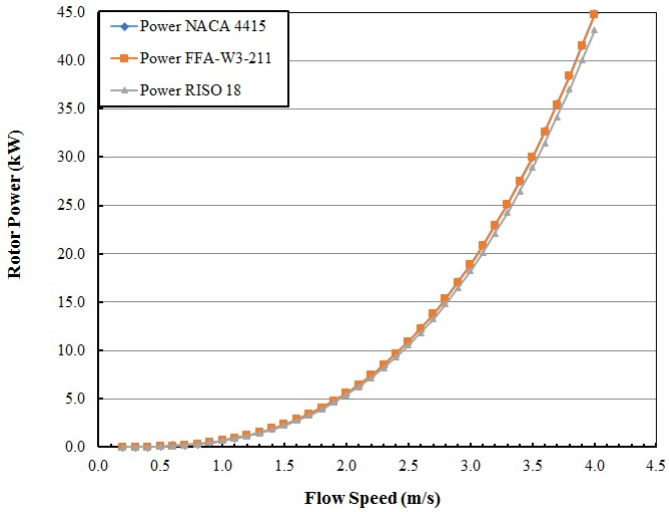


Figure 11.2.20: Power curves comparison at 2 m of diameter at variable speed

### 11.2.3 Test for a 1.5 meters rotor turbine diameter

As noted previously, there are no differences between these profiles in the variable speed power curves. In figure 11.2.21 the power curve of the NACA 4415 profile is much steeper than the others, so from this analysis the NACA 4415 hydrofoil is preferable. In the power coefficient $C_P$ curve, in figure 11.2.22, it can be seen that the FFA-W3-211 profile has a higher maximum than its competitors, even if the NACA 4415 shows a preferable overall trend. As can be seen from table 11.6 and table 11.7, the NACA 4415 profile is the best choice in terms of AEP.

### 11.2.4 Results

For the turbines configurations with diameter 3 and 2 metres, the FFA-W3-211 profile was chosen, while for the configuration of turbines with a diameter of 1.5 metres, the NACA 4415 profile is the best.

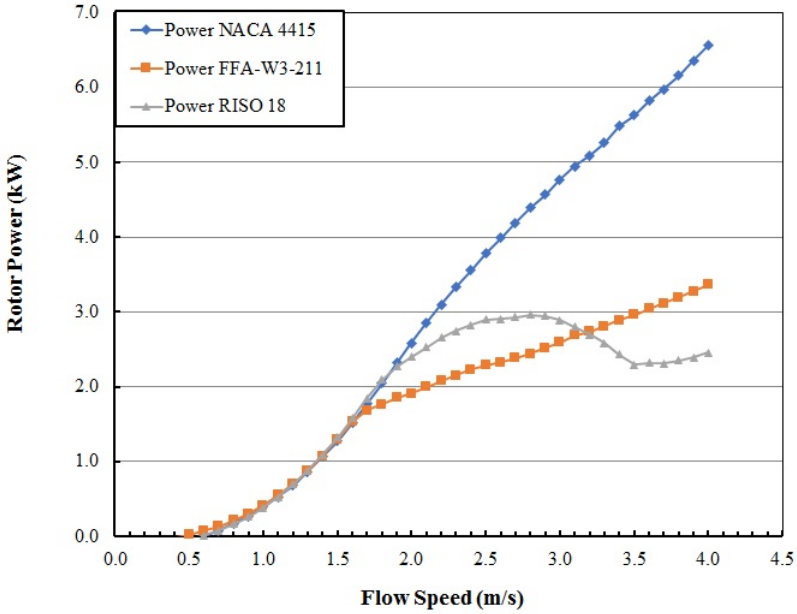


Figure 11.2.21: Power curves comparison at 1.5 m of diameter at fixed speed

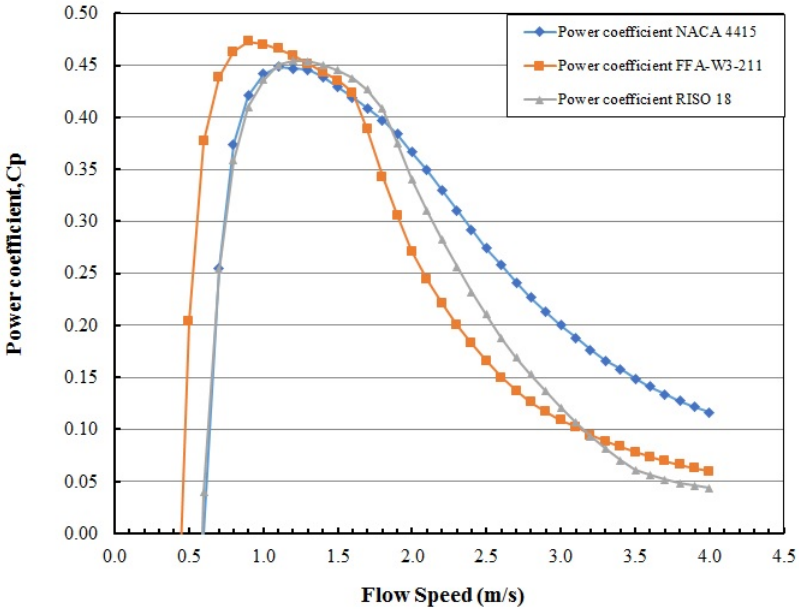


Figure 11.2.22: Power coefficient comparison at 1.5 m of diameter at fixed speed

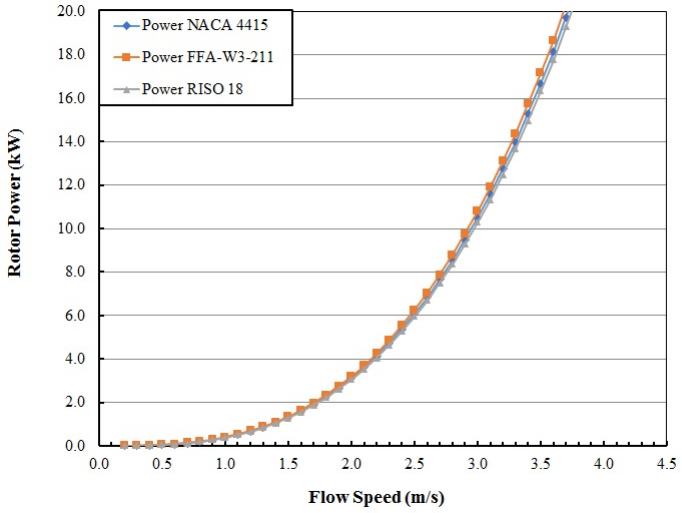


Figure 11.2.23: Power curves comparison at 1.5 m of diameter at variable speed

| CF | NACA 4415 | FFA-W3-211 | RISO-A1-18 |
|---|---|---|---|
| D=3 m | 28.81% | 33.63% | 31.9% |
| D=2 m | 28.18% | 27.28% | 33.18% |
| D=1.5 m | 29.38% | 40.61% | 34.86% |

Table 11.4: Capacity Factor at fixed speed

| CF | NACA 4415 | FFA-W3-211 | RISO-A1-18 |
|---|---|---|---|
| D=3 m | 24.37% | 24.37% | 24.37% |
| D=2 m | 24.37% | 24.32% | 24.37% |
| D=1.5 m | 24.37% | 24.37% | 24.39% |

Table 11.5: Capacity Factor at variable speed

| AEP [kWh/yr] | NACA 4415 | FFA-W3-211 | RISO-A1-18 |
|---|---|---|---|
| D=3 m | 27669 | 27884 | 27567 |
| D=2 m | 12274 | 12472 | 12158 |
| D=1.5 m | 6793 | 6768 | 6768 |

Table 11.6: AEP at fixed speed

| AEP [kWh/yr] | NACA 4415 | FFA-W3-211 | RISO-A1-18 |
|---|---|---|---|
| D=3 m | 26600 | 27128 | 25934 |
| D=2 m | 11940 | 11923 | 11507 |
| D=1.5 m | 6825 | 6496 | 6496 |

Table 11.7: AEP at variable speed

## 11.3 CACTUS

Sandia National Laboratories recently released an open source code for design and analysis of axial-flow and cross-flow marine and hydrokinetic (MHK) turbines, CACTUS (Code for Axial and Cross-flow Turbine Simulation), and has initiated an outreach effort to promote its use among MHK researchers and developers [76]. CACTUS is a turbine performance simulation code based on the blade element method and using a free vortex line description of the turbine wake flow.
A rotor blade consisting of an arbitrary planform shape and foil sections can be modeled by the synthesis of a number of blade elements. The blade loads and wake of the turbine rotor are evolved in time over a certain number of rotor revolutions, until the revolution-averaged rotor power is converged. The code output includes the blade aerodynamic forces, wake vortex trajectories, and performance metrics such as torque and power. CACTUS uses a potential flow model comprised of free vortex line elements to represent the turbine wake flow field. The operational cycle of some turbines, most notably cross-flow turbines or axial flow turbines in yawed flow conditions, cause the turbine blades to operate in dynamically variable flow conditions. For these reasons, some models have been included in CACTUS to evaluate the effects of dynamic stall and to consider the influence of the closeness of free surface (water) on the turbine performance [77].

### 11.3.1 Comparison of different models

The results obtained in the previous study of the TABASCO model are summarised in table 11.8.

| **Location's site parameters** | |
|---|---|
| Water depth | $0.8m$ |
| Width river | $5-6m$ |
| Water speed | $2-2.5m/s$ |
| **Rotor configuration** | |
| Diameter | $1.5m$ |
| Height | $0.6m$ |
| Chord | $0.15m$ |
| $\frac{Chord}{Radius}$ | 0.2 |
| Airfoil | NACA0015 |

Table 11.8: TABASCO full scale design

The comparison was made by varying the speed of the river at a fixed rotation speed of 90 rpm.

As can be seen in figure 11.3.1 and figure 11.3.2, the CACTUS results are overestimated compared to those previously gained. Some possible explanations can be linked to the fact that the CACTUS, besides using a blade element theory instead of the BEM, provides unsatisfactory results when the ratio chord to radius exceeds 12%

| Water velocity [m/s] | TSR | $C_P$ | Power [kW] |
|---|---|---|---|
| 1 | 7.1 | -0.06 | -0.27 |
| 1.25 | 5.7 | 0.19 | 0.17 |
| 1.5 | 4.7 | 0.29 | 0.43 |
| 1.75 | 4 | 0.33 | 0.79 |
| 2 | 3.5 | 0.35 | 1.27 |
| 2.25 | 3.1 | 0.37 | 1.91 |
| 2.5 | 2.8 | 0.38 | 2.69 |
| 2.75 | 2.6 | 0.27 | 2.54 |
| 3 | 2.4 | 0.24 | 2.9 |

Table 11.9: TABASCO results at 90 rpm

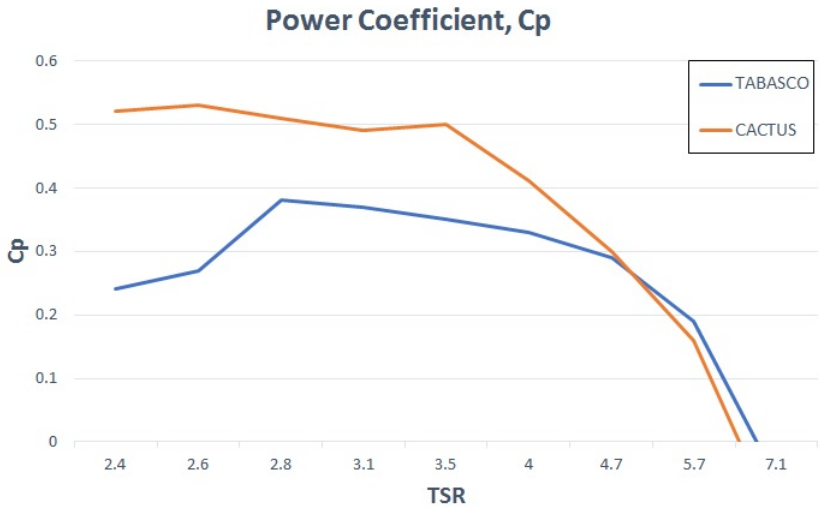


Figure 11.3.1: Turbine power coefficient

[76]. The CACTUS numerical model was validated by experimental data obtained at sufficiently high Reynolds numbers, therefore it cannot be determined whether problems with model predictions are caused by Reynolds number effects, issues related to higher solidity, or both.It is uncertain whether numerical models validated with physical model data obtained at low Reynolds number should be considered validated at all [78].

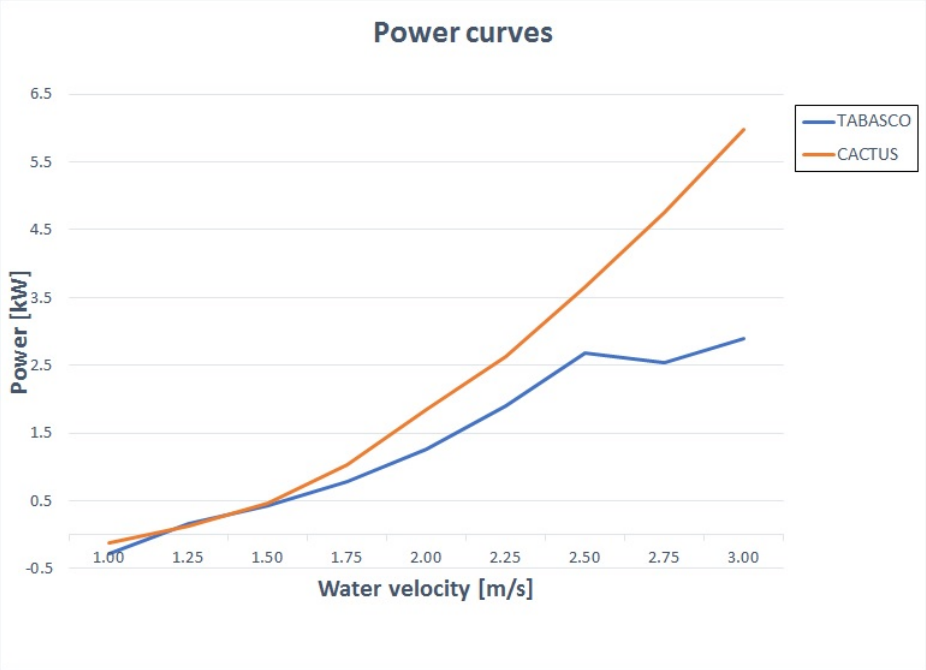


Figure 11.3.2: Turbine power characteristics

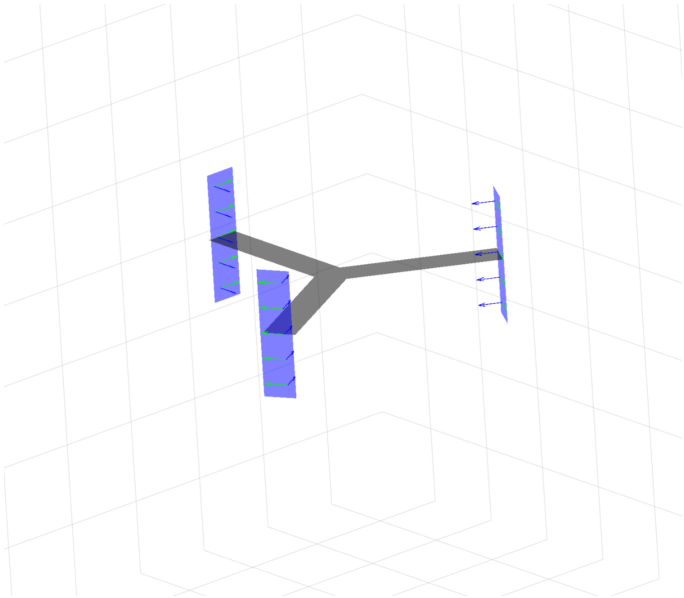

Figure 11.3.3: Geometry simulation on CACTUS

# Chapter 12

# Conclusions and Future Works

In this work, the potential of renewable resources in Africa was evaluated, particularly in Oyo, Congo in order to allow energy self-sufficiency for small communities. The three most important types of renewable sources were analysed: wind, solar and hydro. Firs of all, the analysis of wind power showed that there is such a low potential to make even small applications not worthy. Secondly, photovoltaics is a major resource for the country thanks to its geographical position, but it can not be so exploited due to the vegetation that covers most of the territory. Finally, the potential extracted from watercourses, in particular the Alima river, has been analysed, focusing on applications of kinetic turbines, more advantageous than large hydroelectric plants due to their low environmental impact and low construction and maintenance costs. In order to face difficulties in mathematical modelling of a turbine two software developed by two leading companies in the renewable energy sector were used:

- *HARP_Opt* developed by NREL (National Renewable Energy Laboratory)
- CACTUS developed by SANDIA national laboratories

*HARP_Opt* has been used to evaluate some configurations of horizontal axis turbines. For this study three types of hydrofoils have been adopted in different configurations, in order to evaluate the best one according to the application. In our case study, focused on low speeds, not great differences between the fixed or variable rotation speed configuration of the rotor has been noted, but huge differences can be seen for higher speeds.

CACTUS has been used instead to evaluate the potential of vertical axis turbines. In this case, to prove the reliability of this software, a turbine previously designed by the Polytechnic of Turin, TABASCO, was used as a reference. However, the results show an overestimation: this could be caused by the software still in a development phase during our research.

The results of this paper, may be biased because the data available for Africa are old and very limited.

**Future Projects:**

- Due to the low potential of single renewable sources, the best option could be their combination, not only for a more stable power self-sufficiency, but also for a greater economic profit.
- In chapter 11, other software has been cited: premusably some of them could prove to be of particular interest.
- The CACTUS-DAKOTA coupling, used as an optimization tool, could be investigated.
- All software results, however, should also be evaluated experimentally.

# Nomenclature

**Parameters in Sections 1-9**

| | |
|---|---|
| $\alpha$ | Angle of Attack |
| $\alpha_v$ | Volumetric efficiency |
| $\bar{F}$ | Average force |
| $\delta\Gamma$ | Increase of circulation |
| $\Delta t$ | Time interval |
| $\dot{m}$ | Mass flow rate |
| $\eta_{Carnot}$ | Carnot cycle efficiency |
| $\Gamma$ | Circulation |
| $\lambda$ | Tip Speed Ratio |
| $\lambda_h$ | Tip Speed Ratio at the hub |
| $\lambda_{optimal}$ | Optimal Tip Speed Ratio |
| $\Omega$ | Angular velocity of the wake |
| $\omega$ | Rotational frequency |
| $\omega_{optimal}$ | Optimal rotational frequency |
| $\rho$ | Water density |
| $\sigma$ | solidity ratio |
| $\upsilon$ | kinematic viscosity |
| $A$ | Turbine Area |
| $a$ | Acceleration |
| $a$ | Axial induction factor |
| $a'$ | Angular induction factor |

| | |
|---|---|
| $A_1$ | Upstream Cross-section |
| $A_2$ | Downstream Cross-section |
| $b$ | Interference factor |
| $b_s$ | Distance between the the blade and the support |
| $b_{wk}$ | Axial induction factor far the wake |
| $c$ | blade chord |
| $C_D$ | Drag Coefficient |
| $C_L$ | Lift Coefficient |
| $C_M$ | Elemental torque coefficient |
| $C_N$ | Coefficient of normal force |
| $C_P$ | Power Coefficient |
| $C_T$ | Coefficient of tangential force |
| $C_X$ | Thrust coefficient |
| $C_{pr,min}$ | Minimum pressure coefficient |
| $C_{pr}$ | Pressure coefficient |
| $dE$ | Incremental energy |
| $dF_D$ | Infinitesimal drag force |
| $dF_L$ | Infinitesimal lift force |
| $dF_N$ | Infinitesimal normal force |
| $dF_T$ | Infinitesimal tangential force |
| $dF_X$ | Infinitesimal axial force |
| $dL$ | Infinitesimal tangential force |
| $dM$ | Elemental torque |
| $dN$ | Infinitesimal normal force |
| $dP$ | Power generated to earh radial element |
| $dt$ | Infinitesimal time interval |
| $F$ | Force on the rotor |
| $H$ | Total pressure |

| | |
|---|---|
| $m$ | Mass |
| $M_P$ | Pitching moment |
| $N$ | Number of blades |
| $N_L$ | Number of streamtubes (z coordinate) |
| $N_\theta$ | Number of streamtubes that cross equatorial plane |
| $P$ | Power |
| $p$ | Pressure |
| $p'$ | Pressure drop |
| $P_F$ | Power Flux |
| $p_u$ | Inflow pressure |
| $P_v$ | Vapor pressure |
| $p_w$ | Outflow pressure |
| $P_{available}$ | Kinetic power of undisturbed upstream fluid in Betz Theory |
| $q$ | Dynamic pressure |
| $r$ | Turbine Radius |
| $R_e$ | Reynolds number |
| $s$ | Length of the disturbed wind stream |
| $T$ | Thrust |
| $T_1$ | Input Temperature |
| $T_2$ | Rejection Temperature |
| $U$ | Velocty |
| $u$ | Axial component of fluid velocity |
| $U_1$ | Upstream Speed |
| $U_2$ | Downstream Speed |
| $U_{cavitate}$ | Cavitation velocity |
| $U_{rel}$ | Relative velocity |
| $v$ | Radial component of fluid velocity |

| | |
|---|---|
| $w$ | Angular Velocity |
| $w'$ | Induced angular velocity |

**Parameters in Section 10**

| | |
|---|---|
| $\epsilon$ | Roughness |
| $A$ | River Section |
| $C$ | Chézy's roughness morphology |
| $E$ | Evapotraspiration |
| $ET_p$ | Potential evapotraspiration |
| $ET_{p0}$ | Reference potential evapotraspiration |
| $h$ | Height of river |
| $n_M$ | Manning's roughness coefficient |
| $P$ | Precipitation |
| $Q$ | River average flow rate |
| $R_h$ | Hydraulic radius |
| $S$ | Water Storage |
| $S_P$ | Slope of free water surface |
| $u_c$ | Conversion factor for Manning and Chézy equation |
| $V$ | Water velocity |

**Parameters in Sections 11-12**

| | |
|---|---|
| $C_D$ | Drag coefficient |
| $C_L$ | Lift coefficient |
| $C_P$ | Power coefficient |
| $P$ | Power |

# Bibliography


[1] M. Borg, A. Shires, and M. Collu, "Offshore floating vertical axis wind turbines, dynamics modelling state of the art. part i: Aerodynamics," *Renewable and Sustainable Energy Reviews*, vol. 39, pp. 1214–1225, 2014.

[2] V. Chow and O.-C. Hydraulics, "Mcgraw-hill book co," *New York*, vol. 680, 1959.

[3] EUROSTAT, "Statistics explained: Renewable energy statisticsp," accessed on March 2018. [Online]. Available: http://ec.europa.eu/eurostat/statistics-explained/index.php

[4] UNDP, "Small hydropower-based mini-grids for rural electrification in congo-brazzaville," *United Nations Development Programme.*

[5] WorldBank, "Global solar atlas," accessed on September 2018. [Online]. Available: http://globalsolaratlas.info/

[6] *Atlas of Africa Energy Resources.* United Nations Environment Programme, 2017, no. ISBN: 978-92-807-3639-7.

[7] Ren21, "Global status report," *REN21 secretariat, Paris*, no. ISBN 978-3-9818107-6-9, 2017.

[8] A. Demirbaş, "Global renewable energy resources," *Energy Sources, Part A: Recovery, Utilization, and Environmental Effects*, vol. 28, no. 8, pp. 779–792, 2006. [Online]. Available: https://doi.org/10.1080/00908310600718742

[9] WorldEnergyCouncil, "World energy resources: Hydropower 2016."

[10] R. Gasch and J. Twele, *Wind power plants: fundamentals, design, construction and operation.* Springer Science & Business Media, 2011.

[11] TelosNet, "Part 1 - early history through 1875," accessed on March 2018. [Online]. Available: http://www.telosnet.com/wind/early.html

[12] M. Bellis, "The history of the water wheel." accessed on March 2018. [Online]. Available: https://www.thoughtco.com/history-of-waterwheel-4077881

[13] EncyclopædiaBritannicaInc., "Waterwheel," accessed on March 2018. [Online]. Available: https://www.britannica.com/technology/waterwheel- engineering

[14] ScienceEncyclopedia, "Turbine - history," accessed on March 2018. [Online]. Available: http://science.jrank.org/pages/7030/Turbine-History.html

[15] EncyclopædiaBritannicaInc., "Turbine," accessed on March 2018. [Online]. Available: https://www.britannica.com/technology/turbine

[16] OfficeOfEnergyEfficiency, "Types of hydropower turbines," accessed on March 2018. [Online]. Available: https://www.energy.gov/eere/water/types-hydropower-turbines

[17] K. Sørnes, "Zero: Small-scale water current turbines for river applications," 2010.

[18] M. Liu, "Hydrokinetic turbine power converter and controller system design and implementation," Ph.D. dissertation, University of British Columbia, 2014.

[19] M. Khan, M. T. Iqbal, and J. E. Quaicoe, "A technology review and simulation based performance analysis of river current turbine systems," in *Electrical and Computer Engineering, 2006. CCECE'06. Canadian Conference on.* Ieee, 2006, pp. 2288–2293.

[20] A. Kumar and R. Saini, "Development of hydrokinetic power generation system: A review," 2014.

[21] M. Khan, G. Bhuyan, M. Iqbal, and J. Quaicoe, "Hydrokinetic energy conversion systems and assessment of horizontal and vertical axis turbines for river and tidal applications: A technology status review," *Applied energy*, vol. 86, no. 10, pp. 1823–1835, 2009.

[22] A. L. Niblick, "Experimental and analytical study of helical cross-flow turbines for a tidal micropower generation system," Ph.D. dissertation, 2012.

[23] A. Capezzera, "Analisi di un generatore eolico ad asse verticale," Ph.D. dissertation, POLITECNICO DI TORINO.

[24] J. Winchester and S. Quayle, "Torque ripple and variable blade force: A comparison of darrieus and gorlov-type turbines for tidal stream energy conversion," in *Proceeding of the 8th European Wave and Tidal Energy Conference, Uppsala, Sweden*, 2009.

[25] A. Rachman, R. Balaka, and J. Delly, "A mathematical model for predicting the performance of a horizontal axis river current turbine with consideration of the blade parameters," in *Proceeding International Conference and Exhibition Sustainable Energy and Advanced Materials (ICESEAM 2011), Solo*, 2011, pp. 3–4.

[26] M. Ragheb and A. M. Ragheb, "Wind turbines theory-the betz equation and optimal rotor tip speed ratio," in *Fundamental and advanced topics in wind power.* InTech, 2011.

[27] J. F. Manwell, J. G. McGowan, and A. L. Rogers, *Wind energy explained: theory, design and application.* John Wiley & Sons, 2010.

[28] S. Duran, "Computer aided design of horizontal axis wind turbine blades," *Master's thesis, Middle East Technical University, Ankara, Turkey*, 2005.

[29] C. S. Ferreira, H. A. Madsen, M. Barone, B. Roscher, P. Deglaire, and I. Arduin, "Comparison of aerodynamic models for vertical axis wind turbines," *Journal of Physics: Conference Series*, vol. 524, no. 1, 2014.

[30] M. A. Biadgo, A. Simonović, D. Komarov, and S. Stupar, "Numerical and analytical investigation of vertical axis wind turbine," *FME Transactions*, vol. 41, no. 1, pp. 49–58, 2013.

[31] M. B. Patel and V. Kevat, "Performance prediction of straight bladed darrieus wind turbine by single streamtube model," *International Journal of Advanced Engineering Technology*, vol. 14, p. 2, 2013.

[32] H. Beri and Y. Yao, "Double multiple streamtube model and numerical analysis of vertical axis wind turbine," *Energy and Power Engineering*, vol. 3, no. 03, p. 262, 2011.

[33] A. Muratoglu and M. I. Yuce, "Performance analysis of hydrokinetic turbine blade sections," *Journal ISSN*, vol. 2, 2015.

[34] R. E. Sheldahl, P. C. Klimas, and L. V. Feltz, *Aerodynamic performance of a 5-metre-diameter Darrieus turbine with extruded aluminum NACA-0015 blades*. National Technical Information Service, 1980.

[35] "Thropton energy services," accessed on March 2018. [Online]. Available: http://www.throptonenergy.co.uk/

[36] "Alternative hydro solutions," accessed on March 2018. [Online]. Available: http://www.althydrosolutions.com

[37] BrownellMicrohydro, "Theory: Alternative hydro solutions," accessed on March 2018. [Online]. Available: https://www.brownellmicrohydro.com/collections/alternative-hydro-solutions

[38] "New energy corporation," accessed on March 2018. [Online]. Available: http://www.newenergycorp.ca/technology.html

[39] K. Jolapara, "Waterotor – an innovative breakthrough for harnessing energy from very slow moving water," accessed on March 2018. [Online]. Available: https://www.futureentech.com/2015/07/waterotor-innovative-breakthrough-for.html

[40] "Waterotor," accessed on March 2018. [Online]. Available: https://waterotor.com/

[41] "Hydroquest," accessed on March 2018. [Online]. Available: http://www.hydroquest.net/?lang=en

[42] "Orpc rivgen," accessed on March 2018. [Online]. Available: http://www.orpc.co/our-solutions/scalable-grid-integrated-systems/rivgen-power-system

[43] "Smart hydro power," accessed on March 2018. [Online]. Available: https://www.smart-hydro.de/renewable-energy-systems/hydrokinetic-turbines-river-canal/

[44] "Hydrovolts," accessed on March 2018. [Online]. Available: http://hydrovolts.com/products/c12/

[45] M. Sanni, O. G. Oladipo, I. O. Ogundari, and O. T. Aladesanmi, "Adopting latecomers' strategies for the development of renewable energy technology in africa," *African Journal of Science, Technology, Innovation and Development*, vol. 6, no. 4, pp. 253–263, 2014.

[46] IHA, "Hydropower status report," *International Hydropower Association*, 2017.

[47] A. Miketa and N. Saadi, "Africa power sector: Planning and prospects for renewable energy," *Abu Dhabi United Arab Emirates: IRENA*, 2015.

[48] M. Tricard, "Republic of congo - moving forward with hydropower," accessed on April 2018. [Online]. Available: https://www.andritz.com/hydro-en/hydronews/hydropower-africa/rep-of-congo

[49] "The world bank," accessed on September 2018. [Online]. Available: https://data.worldbank.org/indicator/

[50] NationalGeographic, "Wind power," accessed on November 2018. [Online]. Available: https://www.nationalgeographic.com/environment/global-warming/wind-power/

[51] "Ecmwf," accessed on November 2018. [Online]. Available: https://www.ecmwf.int/en/about/

[52] "Era 5," accessed on November 2018. [Online]. Available: https://confluence.ecmwf.int/display/CKB/What+is+ERA5

[53] H. D. H., "Climet data," accessed on November 2018. [Online]. Available: https://www.ecmwf.int/en/about/media-centre/science-blog/2017/era5-new-reanalysis-weather-and-climate-data

[54] "Era 5 data," accessed on November 2018. [Online]. Available: https://confluence.ecmwf.int/display/CKB/ERA5+data+documentation

[55] "Era5:convention for the u and v components," accessed on November 2018. [Online]. Available: https://www.ecmwf.int/en/faq/what-direction-convention-u-and-v-components-winds

[56] "Python," accessed on November 2018. [Online]. Available: https://www.pythonforbeginners.com/learn-python/what-is-python/

[57] "Honeywell," accessed on November 2018. [Online]. Available: https://www.honeywellstore.com/store/images/pdf/Honeywell-Wind-Turbine-System.pdf

[58] B. Emilio, "Productivity valutation of turbines in democratic republic of the congo," Ph.D. dissertation, Politecnico di Torino, 2018.

[59] F. Miceli, "Wind power plant concepts and performance indicators," accessed on September 2018. [Online]. Available: http://www.windfarmbop.com/wind-power-plant-concepts-and-performance-indicators/

[60] L. David, "Capacity factor," accessed on September 2018. [Online]. Available: https://thegrid.rexel.com/en-us/forums/renewable-and-energy-efficiency/f/forum/354/what-is-the-capacity-factor-of-a-pv-array

[61] J. Gros, *Nos explorateurs en Afrique*. Collection XIX, 2016.

[62] H. V. Looy, *Les Régions africaines d'après les récits des voyageurs dans l'Afrique centrale*, 1883.

[63] J. Gaillardet, B. Dupré, and C. J. Allègre, "A global geochemical mass budget applied to the congo basin rivers: erosion rates and continental crust composition," *Geochimica et Cosmochimica Acta*, vol. 59, no. 17, pp. 3469–3485, 1995.

[64] A. Laraque, G. Mahé, D. Orange, and B. Marieu, "Spatiotemporal variations in hydrological regimes within central africa during the xxth century," *Journal of hydrology*, vol. 245, no. 1-4, pp. 104–117, 2001.

[65] A. Laraque and J.-C. Olivry, "Evolution de l'hydrologie du congo-zaïre et de ses affluents rive droite et dynamique des transports solides et dissous," *IAHS PUBLICATION*, pp. 271–288, 1996.

[66] D. Alsdorf, E. Beighley, A. Laraque, H. Lee, R. Tshimanga, F. O'Loughlin, G. Mahé, B. Dinga, G. Moukandi, and R. G. Spencer, "Opportunities for hydrologic research in the congo basin," *Reviews of Geophysics*, vol. 54, no. 2, pp. 378–409, 2016.

[67] "Climate change knowledge portal," accessed on March 2018. [Online]. Available: http://sdwebx.worldbank.org/climateportal/

[68] J. Betbeder, V. Gond, F. Frappart, N. Baghdadi, G. Briant, and E. Bartholomé, "Mapping of central africa forested wetlands using remote sensing," *IEEE J. Sel. Top. Appl. Earth Obs. Remote Sens*, vol. 7, no. 2, pp. 531–542, 2014.

[69] UNICA, "Stima dell'evapotraspirazione nei modelli concettuali," accessed on March 2018. [Online]. Available:

http://pcserver.unica.it/web/sechi/main/Corsi/

[70] G. Ramillien, F. Frappart, and L. Seoane, "Application of the regional water mass variations from grace satellite gravimetry to large-scale water management in africa," *Remote Sensing*, vol. 6, no. 8, pp. 7379–7405, 2014.

[71] B. M. Alain Laraque, "Banque de données hydrologiques des affluents congolais du fleuve congo-zaïre et informations physiographiques," *Programme PEGI-GBF volet CONGO - UR22/DEC*, vol. ALIMA à Tchicapika, pp. 92–106, 1995.

[72] N. D. Laws and B. P. Epps, "Hydrokinetic energy conversion: Technology, research, and outlook," *Renewable and Sustainable Energy Reviews*, vol. 57, pp. 1245–1259, 2016.

[73] M. R. Ahmed, "Blade sections for wind turbine and tidal current turbine applications–current status and future challenges," *International Journal of Energy Research*, vol. 36, no. 7, pp. 829–844, 2012.

[74] "Levy distribution," accessed on November 2018. [Online]. Available: https://www.vosesoftware.com/riskwiki/Levydistribution.php

[75] "Lévy distribution: Definition, pdf, examples," accessed on November 2018. [Online]. Available: https://www.statisticshowto.datasciencecentral.com/levy-distribution/

[76] C. Michelen, J. C. Murray, V. S. Neary, M. Barone *et al.*, "Cactus open source code for hydrokinetic turbine design and analysis: model performance evaluation and public dissemination as open source design tool," 2014.

[77] J. C. Murray and M. Barone, "Cactus user's manual," *Sandia National Laboratories, Albuquerque, NM*, 2013.

[78] M. Wosnik, P. Bachant, B. Gunawan, A. W. Murphy, and V. S. Neary, "Performance measurements for a 1: 6 scale model of the doe reference model 2 (rm2) cross-flow hydrokinetic turbine." Sandia National Lab.(SNL-NM), Albuquerque, NM (United States), Tech. Rep., 2016.

[79] A. Kumar and R. Saini, "Techno-economic analysis of hydrokinetic turbines," 2017.